POLITECNICO DI MILANO

School of Industrial and Information Engineering
Master's Degree in Biomedical Engineering
Department of Chemistry, Materials and Chemical Engineering
'Giulio Natta'

SYNTHESIS AND CHARACTERIZATION OF INNOVATIVE NANOMATERIALS FOR ANTIMICROBIAL APPLICATIONS

Supervisor: Prof. Gabriele **CANDIANI**
Co-supervisors: Nina **BONO**, PhD
Vincenzina **BARBERA**, PhD

Authors:
Simone **RACITI** 896846
Edoardo **TESTA** 897135

Academic Year 2019/ 2020

RINGRAZIAMENTI

Per la realizzazione di questo progetto di tesi desideriamo innanzitutto ringraziare il nostro relatore Prof. Candiani che, con grandissima umanità, professionalità e saggezza ci ha accompagnati e consigliati durante tutto questo percorso formativo sia dal punto di vista professionale che personale. Non avremmo potuto desiderare di meglio.

Un sentito grazie va inoltre alle nostre correlatrici Nina e Vincenzina, per il loro supporto costante e la serenità dei rapporti instaurati che ci hanno permesso di lavorare in un clima, a nostro modesto parere, perfetto. Insieme a loro ringraziamo Chiara, Lucia e tutto il gruppo ISMaterials del Prof. Galimberti per averci aiutati nei primissimi e negli ultimi passi di questo percorso.

Ai nostri compagni di università, carissimi amici e compagni di vita oltre che di studi. Beatrice e Stefano, a voi dedicheremo mille volte grazie.

Grazie poi alle nostre famiglie, ai nostri affetti. Ci avete supportato, forse a volte sopportato, durante tutto questo lungo, ultimo traguardo. Senza di voi non saremmo qua e tutto questo non sarebbe stato possibile.

Grazie quindi a tutti voi, che costantemente avete creduto in noi.

Ma il più grande ringraziamento lo facciamo reciprocamente a noi stessi. Compagni d'avventure universitarie, compagni di tesi. L'uno il braccio destro dell'altro, sempre uniti e con un solo obiettivo: dare sempre il meglio di noi e risaltare il meglio dell'altro. Grazie, grazie, grazie.

INDICE

Acronimi

- CA-SP-Ag: SP/Ag-functionalized Carbon allotropes
- CA: Carbon Allotropes
- CB: Carbon Black N326 + SP
- CB350: Carbon Black N326 + SP + 350μL *Tollens reactive*
- CB650: Carbon Black N326 + SP + 650μL *Tollens reactive*
- CBs: Carbon Blacks (general)
- CFU: Colony Forming Unit
- CNT: MWCNT NC7000 + SP
- CNT350: MWCNT NC7000 + SP + 350μL *Tollens reactive*
- CNT650: MWCNT NC7000 + SP + 650μL *Tollens reactive*
- CNTs: Carbon Nanotubes (general)
- D_H: Hydrodynamic Diameter
- dH_2O: Deionized water
- DLS: Dynamic Light Scattering
- ELS: Electrophoretic Light Scattering
- EPS: Extracellular Polymeric Substance
- FFT: Fast Fourier Transform
- G: Graphite Nano 307 + SP
- G350: Graphite Nano 307 + SP + 350μL *Tollens reactive*
- G650: Graphite Nano 307 + SP + 650μL *Tollens reactive*
- GO: Graphene Oxide
- GSH: Glutathione
- HRTEM: High Resolution Transmission Electron Microscopy
- LB: Luria-Bertani Broth
- MBC: Minimum Bactericidal Concentration

- MDR: Multi-drug Resistance
- MW: Molecular Weight
- MWCNTs: Multi-Walled Carbon Nanotubes
- O.N.: Over Night
- OD: Optical Density
- PBS: Phosphate Buffered Saline
- PC: Polycarbonate
- PDI: Polydispersity Index
- PG: Propylene glycole
- rGO: Reduced Graphene Oxide
- ROS: Reactive Oxygen Species
- SA: Surface Area
- SA/V: Surface Area to Volume (ratio)
- SEM: Scanning Electron Microscopy
- SP: Serinol Pyrrole
- SWCNTs: Single-Walled Carbon Nanotubes
- TGA: Thermogravimetric Analysis
- UV-Vis: UV-visible
- WAXD: Wide Angle X-Ray Diffraction
- ZP: Zeta Potential

Abstract

Among the wide variety of materials, peculiar nanometric structures of nanomaterials are increasingly acquiring more and more relevance in the scientific world thanks to their unique chemical and physical properties. Their potential to perform as antimicrobial platforms represents indeed one of the most attractive fields of nanobiotechnology in the prevention of Multi-drug Resistance (MDR), i.e. the natural selection process carried out by microorganisms protecting from common antibiotics. In this context, Graphene and its derivatives find place as an alternative, an effective and at the same time safe solution fighting against MDR [1].

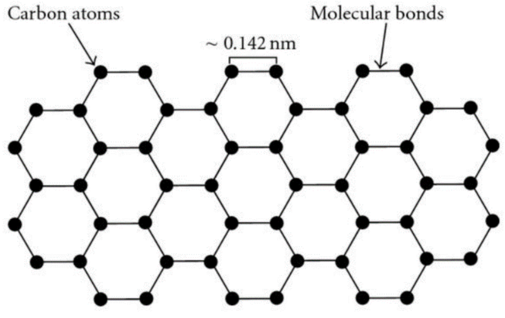

Figure a - Schematic representation of the graphene latticework [2].

The exceptional electronic and mechanical features of the monolayered carbon latticework of Graphene (Figure a) are renown from its first characterization by Geim and Novoselov in 2004 [3], whose study grant them the Nobel Prize in Physics in 2010. Aside from this, the extremely high surface area of interaction, together with their chemical tunability, made Graphene and its derivatives the preferred choice in a variety of scientific articles dealing with the research of enhanced antimicrobial performances [4].

Our thesis work will focus on the synthesis, characterization and evaluation of the antimicrobial activity elicited by three modified Graphene allotropes (i.e. Graphite, Carbon Black (CB) and Multiwalled Carbon Nanotubes (MWCNTs)) against *Escherichia Coli (E. coli)* in the form of suspensions.

Modifications of the raw materials occurred through a double-stage

functionalization of the allotropes with Serinol Pyrrole (SP) and silver (Ag) nanoparticles (NPs) to enhance their solubility and their antimicrobial activity, respectively.
Thermogravimetric analysis (TGA) confirmed the desired SP-functionalization rate (10% (w/w)) for every sample, while Ag-functionalization rate demonstrated to be allotrope-dependent. These results were corroborated by High Resolution Transmission Electron Microscopy (HRTEM) images (Figure b).

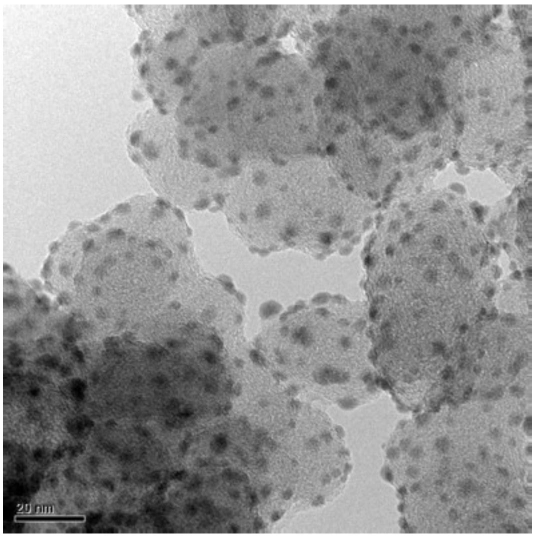

Figure b - HRTEM micrograph representing functionalized CB. Black dots on the surface are Ag NPs.

Further analysis were carried out through Dynamic Light Scattering (DLS) and Electrophoretic Light Scattering (ELS) measurements, suggesting the beneficial effect of probe ultrasonication on short-term homogeneity of particles size and the formation of an external protein corona in the presence of culture medium proteins. The effect of ultrasonication was next deeply evaluated by measuring suspension absorbances after ultrasonication (3 hours kinetics) through a UV-visible spectrophotometer apparatus (Figure c).

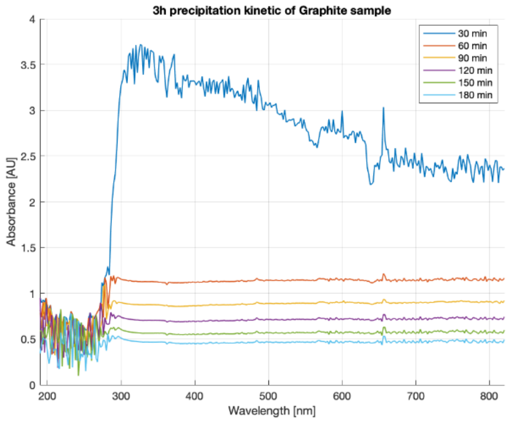

Figure c - Absorbance spectra of Graphite suspension at different time steps: 30, 60, 90, 120, 150, 180 minutes after ultrasonication. Absorbance values were recorded using pure PBS as the blank solution ($PBS_{Absorbance} = 0$).

Despite the SP-functionalization and the eventual probe ultrasonication of samples, our suspensions resulted quite unstable in the mid/long-term, since the formation of precipitate occurred after 3 hours and 24 hours from ultrasonication.

For these reasons, antimicrobial screening tests were performed keeping dynamic conditions of incubation of our samples by means of a home-made rotating system designed and manufactured by us.

These tests were carried out for each allotrope, comparing the activity between the starting materials (i.e allotrope + SP) and their Ag-functionalized counterparts (allotrope + SP + Ag).

Our findings suggested an outstanding enhancement of the antimicrobial activity provided by the enrichment with Ag NPs against *E. coli*, for each allotrope (Figure d).

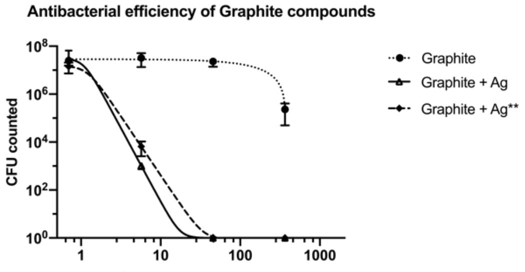

*Figure d - Antibacterial efficiency of Graphite samples (**: higher Ag loading) represented as number of Colony Forming Units (CFUs) counted over Sample Ag Molarity [µM]. The unfunctionalized sample (i.e. Graphite) is represented using its Equivalent Ag Molarity.*

The bactericidal effect resulted to be dose-dependent and different between the three tested allotropes (Figure e).

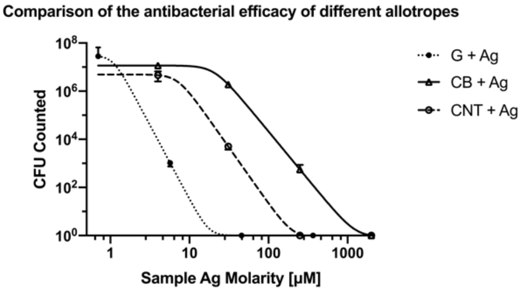

Figure e - Comparison of the antibacterial efficacy among Ag loaded Graphite, Carbon Black and MWCNTs.

According to our findings, we speculated about the antimicrobial mechanism of action displayed during our tests. The absence of Ag^+ ions was preliminary evaluated by means of a dedicated assay, thus we could primarily suggest that high oxidative stress levels elicited by oxygenated species trapped inside metallic Ag NPs may be the principal bactericidal mechanism [5]. The major wrapping ability around bacterial cells of Graphite and MWCNTs samples was next proposed to explain the higher antibacterial effect exerted by these allotropes with respect from CB ones, since higher interaction would consequently expose a higher number of Ag NPs to bacteria. Furthermore, basing on bibliographic evidences, we could likewise suggest a synergistic effect between the aforementioned mechanism and widely reported processes of cellular membrane perforation by means of sharp edges characteristic of Graphite and MWCNTs [6].

In conclusion, our work provides new insights about a simple, sustainable and green procedure for the functionalization of graphene allotropes for antimicrobial purposes. Integrating the wide variety of scientific literature dealing with this, our project can be considered a starting point for researches aiming to find application of graphene-related materials in a multitude of scientific fields requiring enhanced antimicrobial properties.

Sommario

Tra l'ampio spettro delle peculiarità dei materiali, le strutture nanometriche caratteristiche dei nanomateriali stanno via via acquisendo rilevanza sempre maggiore nel mondo scientifico grazie alle loro proprietà chimiche e fisiche uniche nel loro genere. La loro potenzialità di comportarsi come piattaforme antibatteriche rappresenta invero uno dei campi della nanobiotecnologia più allettanti nella prevenzione della resistenza agli antibiotici (Multi-drug Resistance, MDR), ovvero il processo di selezione naturale condotto dai microorganismi al fine di proteggersi verso i comuni antibiotici. In questo contesto, il Grafene e i suoi derivati si inseriscono nel mondo scientifico come un'alternativa valida, efficace e allo stesso tempo sicura nella lotta contro la MDR [1].

Le eccezionali proprietà elettroniche e meccaniche del reticolo a monostrato atomico del Grafene (Figura a) sono riconosciute fin dalla sua prima caratterizzazione compiuta da Geim e Novoselov nel 2004 [3], il cui studio è valso loro l'assegnazione del Premio Nobel per la Fisica nel 2010.

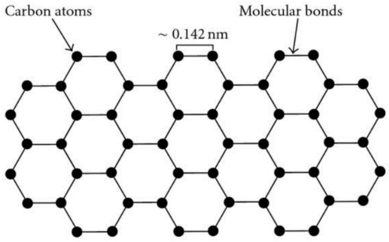

Figure a – Rappresentazione schematica del reticolo monoatomico del Grafene [2].

Oltre a ciò, l'area superficiale di interazione con l'ambiente particolarmente estesa, unitamente alla loro elevata funzionalizzabilità chimica, hanno fatto del Grafene e dei suoi derivati la scelta privilegiata per svariati articoli scientifici relativi alla ricerca di materiali con caratterisitche antibatteriche superiori [4].

Il nostro lavoro di tesi si focalizzerà dunque sulla sintesi, la caratterizzazione e infine la

valutazione dell' attività antibatterica suscitata da tre allotropi del Grafene modificati (ovvero Grafite, Carbon Black (CB), e Nanotubi di Carbonio Multistrato (MWCNTs)) sottoforma di sospensioni nei confronti di *Escherichia coli (E. coli)*.

Tali modificazioni sulle materie prime hanno previsto una funzionalizzazione a doppio stadio di ciascun allotropo con Serinol Pirrolo (SP) e nanoparticelle (NPs) di argento (Ag) per aumentarne la loro solubilità e le proprietà antibatteriche rispettivamente.

Delle analisi Termogravimetriche (TGA) hanno confermato la riuscita della desiderata funzionalizzazione con SP (10% (w/w)) per ciascun campione, mentre la funzionalizzazione con Ag ha dimostrato di essere differente per i vari allotropi. I risultati di funzionalizzazione con Ag sono stati avvalorati da immagini ad alta risoluzione al microscopio elettronico a trasmissione (HRTEM) (Figura b).

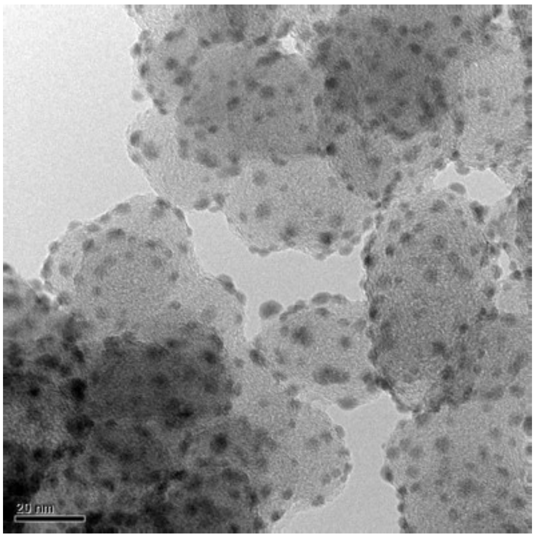

Figure b – Microscopia HRTEM raffigurante CB funzionalizzato. I punti neri sulla superficie degli acini sono nanoparticelle di Ag.

Ulteriori analisi sono state eseguite per mezzo di misurazioni in Dynamic Light Scattering (DLS) ed Electrophoretic Light Scattering (ELS), suggerendo l'effetto benefico dell'ultrasonicazione a sonda sull'omogeneità a breve termine delle dimensioni delle particelle e la formazione di una corona proteica all'esterno di esse in presenza di proteine derivanti dai terreni di coltura.

L'effetto dell'ultrasonicazione sulla stabilità delle sospensioni è stato poi valuato approfonditamente misurando la loro assorbanza durante le 3 ore successive alla procedura di ultrasonicazione per mezzo di uno spettrofotometro operante nel range UV-visibile (Figura c).

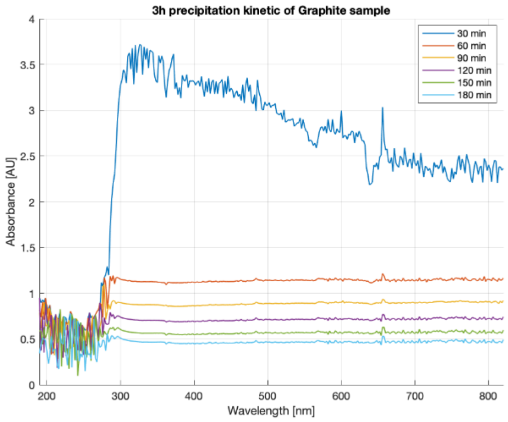

Figura c – Spettri di assorbanza per la sospensione del campione Grafite a diverse tempistiche: 30, 60, 90, 120, 150, 180 minuti dopo l'ultrasonicazione. I valori di assorbanza sono stati registrati utilizzando PBS (Phosphate Buffered Saline) come soluzione di riferimento. (PBS $_{AU}$ = 0).

Nonostante la funzionalizzazione con SP e la successiva ultrasonicazione, le nostre sospensioni sono risultate instabili nel medio/lungo termine, con formazione di precipitato dopo 3 ore e 24 ore dall'ultrasonicazione.

Per queste ragioni, i successivi test di antibattericità sono stati eseguiti mantenendo delle condizioni di incubazione dinamica dei nostri campioni per mezzo di un sistema rotante progettato e costruito da noi stessi.

Questi test sono stati eseguiti per ciascun allotropo, confrontando l'attività antibatterica dei materiali di partenza (allotropo + SP) con loro controparti funzionalizzate con Ag (allotropo + SP + Ag).

I nostri risultati sembrerebbero suggerire un eccezionale incremento dell'attività antibatterica dato dall'arricchimento con nanoparticelle di Ag contro E. coli, per ogni allotropo (Figura d).

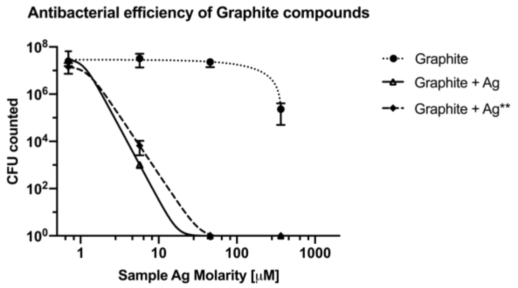

*Figura d – Efficacia antibatterica dei campioni Grafite (**: quantità di Ag legato superiore) rappresentata per mezzo delle CFU (Unità batteriche formanti colonie) contate in funzione della molarità di Ag presente sull'allotropo [µM]. Il campione non funzionalizzato è stato rappresentato utilizzando una molarità di Ag equivalente.*

L'effetto battericida è risultato essere dose-dipendente e differente per i tre allotropi testati (Figura e).

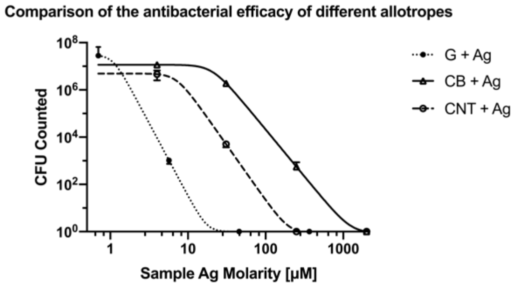

Figure e – Confronto dell'efficacia antibatterica fra i tre allotropi ottenuti dalla stessa procedura di funzionalizzazione con Ag.

In accordo con tali risultati, abbiamo potuto proporre delle ipotesi sul meccanismo battericida emerso durante i nostri test microbiologici.

L'assenza di ioni Ag^+ è stata preliminarmente valutata per mezzo di un saggio dedicato, i quali risultati ci hanno permesso in primo luogo di affermare che il meccanismo antibatterico principale è stato dato dagli alti livelli di stress ossidativo generati dalle specie contenenti ossigeno intrappolate nel reticolo delle nanoparticelle di Ag metallico [5].

La maggiore capacità di avvolgimento intorno alle cellule batteriche dei campioni Grafite e MWCNTs è stata poi proposta per spiegare la maggiore efficacia antibatterica suscitata da questi due allotropi rispetto ai campioni CB, dal momento che una maggiore interazione dei materiali con i microorganismi dovrebbe conseguentemente esporre un numero maggiore di nanoparticelle di Ag a contatto con i batteri. Inoltre, basandoci sull'evidenza di fonti bibliografiche, abbiamo potuto altresì suggerire un effetto sinergico fra i sopracitati meccanismi e gli ampiamente menzionati processi di perforazione della membrana cellulare batterica per mezzo degli spigoli vivi caratteristici della Grafite e dei MWCNTs [6].

In conclusione, il nostro lavoro fornisce ulteriori spunti riguardo ad un nuovo, semplice, sostenibile ed ecologico processo per la funzionalizzazione degli allotropi del Grafene per scopi antibatterici.

Integrando l'ampia gamma di articoli scientifici relativi a questo campo di ricerca, il nostro progetto può essere dunque considerato un punto di partenza per ricerche finalizzate a trovare un'applicazione dei materiali derivati del Grafene in una moltitudine di campi scientifici laddove sono richieste proprietà antibatteriche performanti.

1 Introduction

1.1 Biomedical applications of nanomaterials

A nanomaterial is a material with any external dimension in the nanoscale or having an internal structure or surface in the nanoscale (ISO/TS 80004-1:2015), where nanoscale is defined as the scale range between 1 and 100 nm (ISO/TS 80004-1:2015).

Over the last two decades, nanomaterials increasingly acquired relevance in the scientific world thanks to their unique chemical and physical properties, such as their high surface tailorability, improved solubility and intrinsic optical, magnetic and electrical features [7][8].

The scientific field which deals with nanomaterials is called nanoscience, defined as the study of phenomena and manipulation of entities at a size range from 100 nm down to the atomic level. At this scale range, materials acquire exclusive chemical and physical properties: this is mainly due to the increased surface area to volume (SA/V) ratio of the nanometric structures and associated quantum effects [9].

Biomedical applications of nanomaterials relate to nanobiotechnology, the combination of biotechnology and nanotechnology. Therefore, nanobiotechnology refers to molecular-scale interactions between biological structures and nanomaterials.

The majority of applications of nanomaterials in biomedicine can be divided into two areas: diagnosis, such as biosensors and imaging [8], and therapeutics, such as drug or gene delivery [10]. Nanomaterials' tunable surface reactivity, together with their capability to get into cells, is a fundamental mechanism supporting these applications [9].

1.2 Antimicrobial nanomaterials

Among the wide range of applications of nanomaterials, one of the most attractive field for researchers concerns their ability to perform as antibacterial platforms. Their potential implementation in the industry of medical devices, wastewater treatment, food packaging, synthetic textiles and dentistry makes them a compelling solution worldwide [11].

Nanostructures expose a higher number of atoms on their surface compared to macroscopic structures because of their high SA/V ratio. Since biochemical reactions occur at the interface between the material and the living organisms, this means that a given mass of nanomaterial should be much more reactive than the same mass made up of larger particles because of the major amount of area exposed to the environment (Figure 1.1).

Translating this concept to the antimicrobial field, it is simple to understand how a potential antibacterial effect of such materials would be greatly enhanced, since the contact area between their surfaces and microorganisms exponentially increases decreasing the particle size [9].

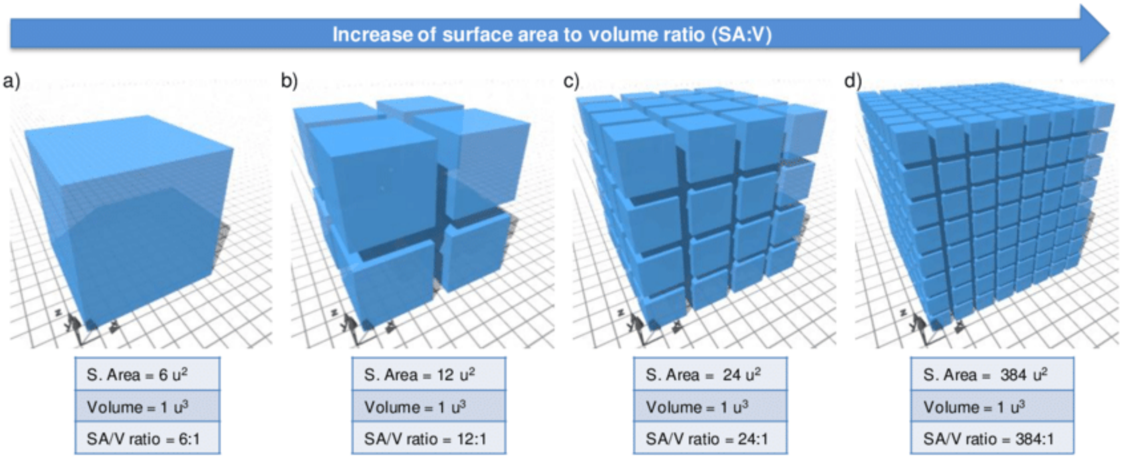

Figure 1.1 - Schematic representation of the variability of the SA/V ratio related to nanoparticle dimensions. [Portilla, Luis. (2017). Functionalization of Metal Oxide Nanostructures via Self-Assembly. Implications and Applications.]

According to the desired application, antimicrobial nanomaterials could be dispersed in proper liquid to form suspensions, deposited onto solid substrates (e.g. antimicrobial surfaces) or embedded into 3D polymeric matrices (e.g. antimicrobial hydrogels or aerogels). In all of these cases, environmental conditions are of fundamental importance to establish the interaction between materials and microorganisms.

The antimicrobial properties of nanomaterials could be exerted both by the bulk structure of the nanomaterial (i.e. *contact-dependent* antimicrobial mechanism) or by specific elements/molecules/nanoparticles (NPs) released from their surface (i.e. *contact-independent* antimicrobial mechanism) (Figure 1.2).

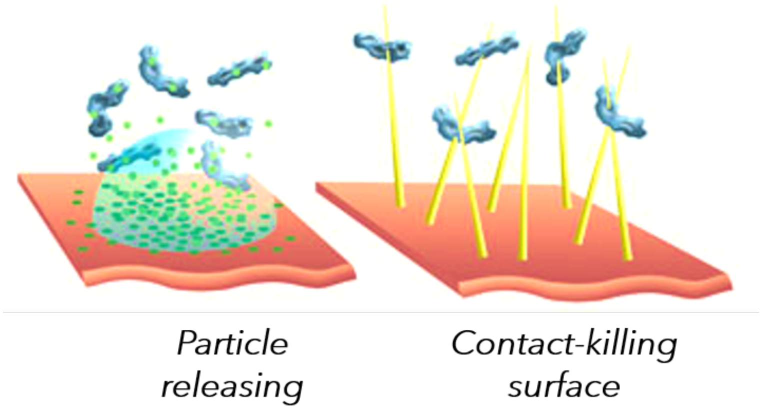

Figure 1.2 - Representation of the two antibacterial mechanisms elicited by nanomaterials. [G. Donelli (ed.), Biofilm-based Healthcare-associated Infections: Volume II, Advances in Experimental Medicine and Biology 831, DOI 10.1007/978-3-319-09782-4_7.]

On the one hand, an interesting antibacterial strategy is based on bio-inspired nano-patterned surfaces, with very effective antimicrobial activity due to their specific roughness and shape: shark skin, dragonfly wings and pagurus carapaces are some examples of natural antibacterial surfaces with contact-dependent antibacterial behavior [12]. The inherent antibacterial features of these materials directly derive from the specific architecture of their surfaces.

On the other hand, the release of ions, molecules or atoms from nanomaterial surfaces represents an alternative strategy. For example, metal oxide NPs such as Fe_2O_3 [13], ZnO [14] and CuO [15], are well known nanomaterials with intrinsic antibacterial activity and are well established in commercial products due to their dimensional tunability and production process affordability [16].

In the case of functionalization, NPs can acquire even more interesting properties: their immobilization on bulk materials could be useful to realize high-performance antimicrobial surfaces. A promising novel approach is to functionalize nanomaterials to form nanocomposites [11], [17] in order to achieve, amongst other features, high antibacterial efficiency exploiting both contact-dependent and independent mechanisms.

Nanomaterials have been extensively exploited in many different biotechnological applications in recent years, therefore, in accordance with the increasing need of antimicrobial platforms, the aim of researchers is to provide deeper knowledge about their bactericidal properties.

1.2.1 Issues related to bacteria

Choice of bacteria phenotype

Prokaryotes, such as bacteria, are known to live under different phenotypes depending on circumstances such as the availability of nutrients, presence of surfaces and their physico/chemical structure or the presence of shear stresses.
The primordial bacteria phenotype is the planktonic one, which refers to microorganisms drifting or floating in an aqueous environment. A planktonic habitat for prokaryotes can encompass water films around soil particles, saliva in the mouth, fluids in the intestinal lumen, serum in blood vessels, and urine in the bladder and urinary tract [18].
Planktonic bacteria could readily adhere to surfaces and turn into sessile bacteria: depending on definitions, this phenotype can include bacteria immediately attached to surfaces and those who can form stable communities embedded in a self-produced extracellular polymeric matrix (EPS). This kind of colonization is called *biofilm* (Figure 1.3).

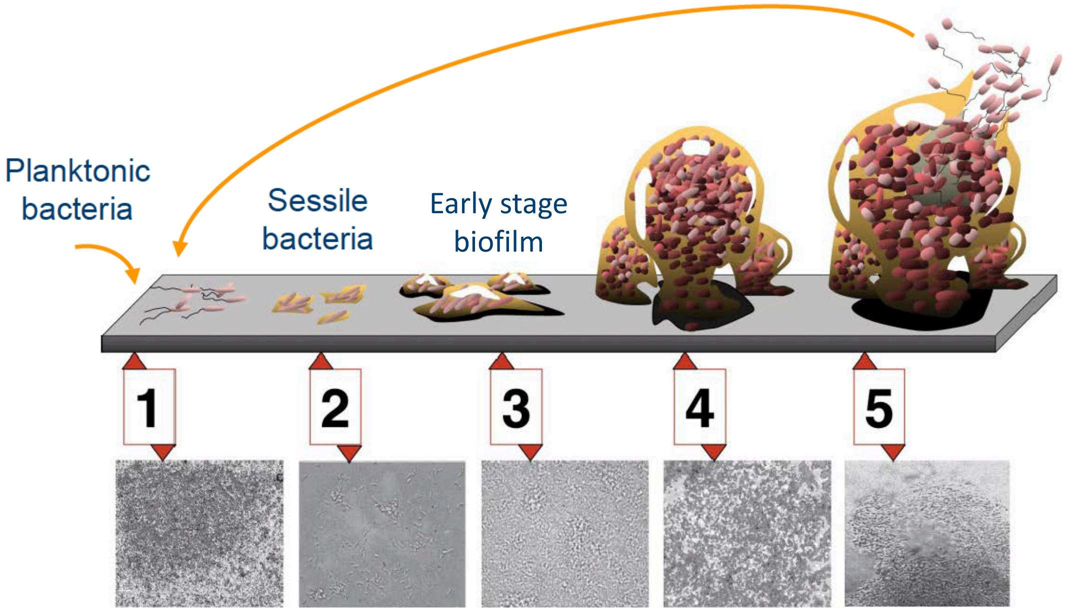

Figure 1.3 – Five stages of biofilm development. Each stage of development in the sketch is paired with the photomicrograph of a developing P. aeruginosa biofilm [Monroe D. (2007) Looking for Chinks in the Armor of Bacterial Biofilms. PLoS Biol 5(11): e307. https://doi.org/10.1371/journal.pbio.0050307].

"Matrix-encased bacterial biofilms that form on implanted medical devices often lead to life-threatening systemic infections and device failure" [19]. Indeed, bacteria in biofilm display higher resistance to a supra-inhibitory concentration of antibiotics with respect to planktonic ones because of the shielding effect guaranteed by the EPS. Moreover, sub-minimal inhibitory concentrations (sub-MIC) of different class of antibiotics were found to induce biofilm growth for several bacterial species, thus issues related to biofilm formation became more and more problematic.

For these reasons, it is imperative to better understand environmental conditions leading to a specific bacterial phenotype in order to outline the optimal experimental setup and, eventually, engineer the optimal antimicrobial nanomaterial suitable for a specific application.

Multi-drug resistance

Infectious diseases caused by pathogenic bacteria are one of the most troublesome health challenges worldwide. Issues related to this afflict various fields including biomedicine, water and food industry [20].

For decades, antibiotics played a fundamental role in the treatment of infectious diseases, nevertheless, their overuse and misuse (Figure 1.4) , as well as a lack of new drug development by pharmaceutical industries, have resulted in the natural process of multidrug resistance (MDR) displayed by microorganisms [21] (Figure 1.5). *Escherichia coli (E. coli)*, *Pseudomonas aeruginosa (P. aeruginosa)* and *Staphylococcus aureus (S. Aureus)* are just some examples of the MDR pathogens and important causes of various hospital-acquired infections [22]. MDR is related to every kind of bacteria and to everyone, for all ages and for every country.

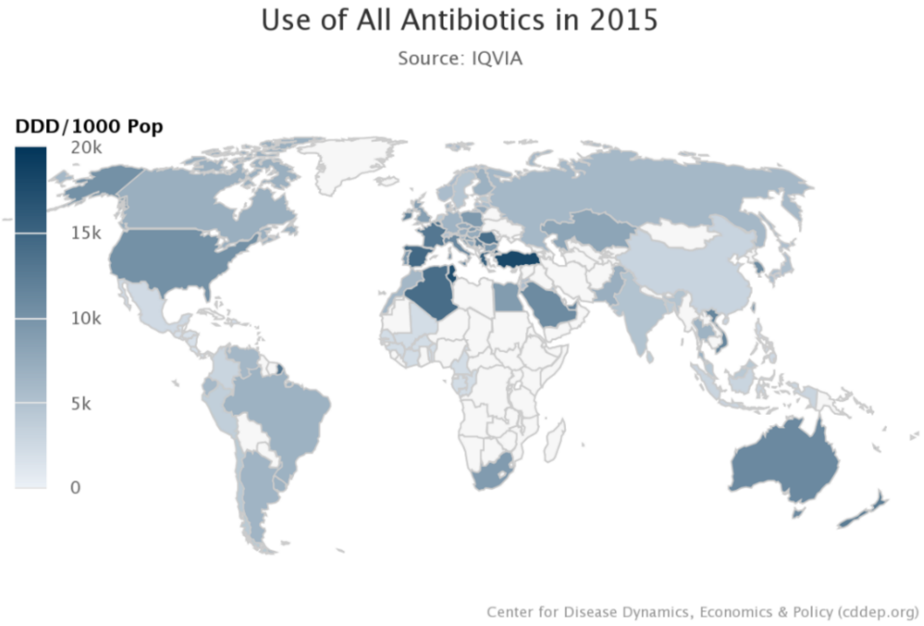

Figure 1.4 - Global distribution of antibiotics reported as Defined Daily Dose per 1000 individuals (2015). [The Center for Disease Dynamics, Economics & Policy. ResistanceMap: Antibiotic Use. 2019. https://resistancemap.cddep.org/AntibioticUse.php].

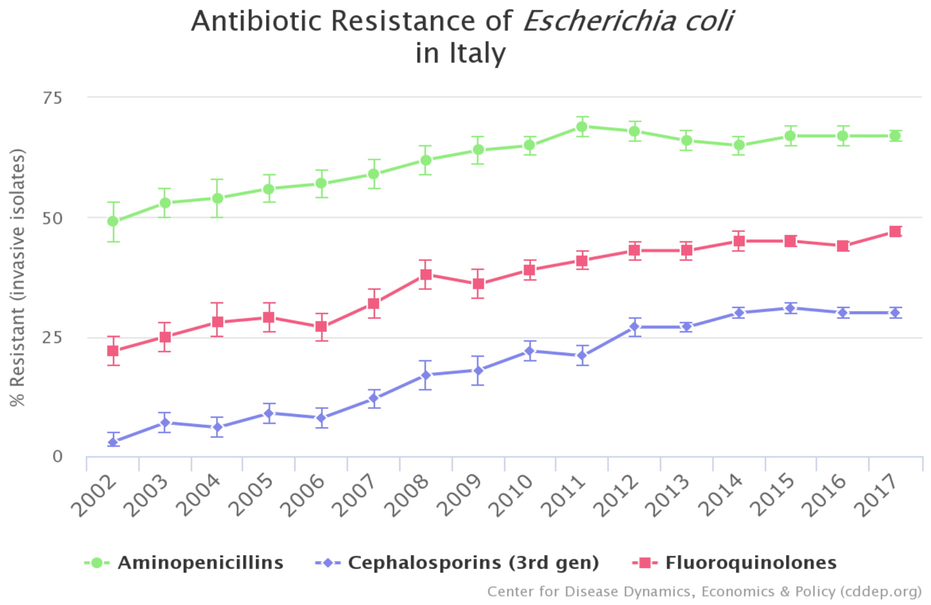

Figure 1.5 - Development of MDR of E. coli in Italy. Three different trends related to three different common antibiotics used for the treatment of E. coli are reported. Data includes aggregated resistance rates for isolates from blood and cerebrospinal fluid (i.e., invasive) from inpatients of all ages. Resistance is evaluated using the clinical breakpoint criteria used by local laboratories. [The Center for Disease Dynamics, Economics & Policy. ResistanceMap: Antibiotic Resistance. 2019. https://resistancemap.cddep.org/AntibioticUse.php].

In this scenario, the need for new antimicrobial nanomaterials able to fight and prevent pathogenic diseases has inspired much research in the field of nanotechnology. Due to alternative, effective and at the same time safe mechanisms of action, this new-generation materials could offer an excellent solution to issues related to microorganisms colonization (i.e. biofilm formation) and MDR [1], [20], [23]–[25].

1.3 Graphene: a promising nanomaterial

Graphene is a one carbon (C) atom thick nanomaterial, arranged as a network of aromatic hexagonal rings to form a polymeric monolayered structure (Figure 1.6).

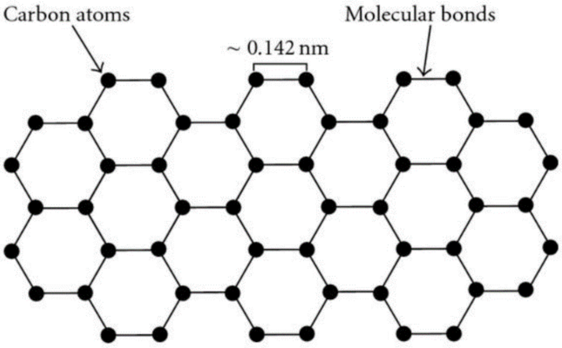

Figure 1.6 - Schematic representation of the graphene sheet structure [2].

This 2D carbon latticework makes up all the graphene related materials and possesses unique properties: as a monolayer of carbon atoms, graphene is almost transparent, notwithstanding this, it is impermeable to gasses and has exclusive mechanical properties, with a Young modulus of approximately 1 TPa (almost 5 times higher than that of the stainless steel).
In addition, graphene has an extraordinary thermal in-plane conductivity, which makes it one of the best heat conductors among the others.
Together with all of these exclusive features, its outstanding electronic properties attracted most of the scientific attention. Indeed, thanks to sp^2 hybridization of carbon atoms, graphene is characterized by an extremely high electrical conductivity due to its great in-plane charge carriers mobility [26]–[28].
Although these remarkable properties have been recorded on a wide variety of graphene samples, it is worth noting that they are mainly evidenced for high-quality few-layered graphene and decrease as the number of stacked layers increases as well as for structural defects displayed on single layers [28].

Since its first characterization in 2004 by Geim and Novoselov [3], graphene synthesis methods have been implemented and refined, making it possible to obtain few-layer thick structures in more efficient ways [29]–[32].

The method of production of graphene is closely related to its applications. In recent years this nanomaterial has rapidly raised its presence in the scientific literature, with more and more researches aimed at looking for innovative employment of graphene in a broad spectrum of commercial uses, thus synthesis has become cheaper and simpler [28]. All of these advancements in manufacturing processes in terms of product quality and affordability, along with the crescent interest of the scientific community, are progressively increasing graphene competitivity into innovative fields of application, making it a promising nanomaterial for potential biomedical applications.

Actually, graphene and its derivatives are employed in this field as nanocarriers in drug and gene delivery - such as the few-layers graphene oxide (GO) for a pH-controlled drug release and the GO-PEI (graphene oxide – polyethylenimine) for DNA transfection; in biosensing - for the detection of thrombin, oligonucleotides, amino acids and ATP; in bioimaging - using aromatic ring intrinsic fluorescence - and in tissue engineering - to elicit mammalian cells growth on a thin GO film [31], [33] (Table 1.1).

In addition to that, the antimicrobial application of graphene has recently become relevant as an alternative to hinder MDR exploiting the unique features of this nanomaterial [1], [22].

Table 1.1 - Biomedical applications of graphene and its derivates.

Biomedical applications of graphene and graphene-derivates

Application	Study	Reference
Biosensing	ssDNA[a]-G[b] for cDNA[c] probing	Mohanty et al. [34]
	Carbohydrate-G for *P.aeruginosa*[d] lectins detection	Chen et al. [35]
	ssDNA-GO for FRET[e] detection of cDNA	He et al. [36]
Mass Spectroscopy	GO/rGO[f] matrixes for ssDNA detection in LDI-MS[g]	Tang et al. [37]

Gene and Drug Delivery	lPEI[h]-GO for gene delivery	Chen et al. [38]
	bPEI[i]-GO for gene and drug delivery	Kim et al. [39]
	Chitosan-GO for cancer treatment	Bao et al. [40]
Cell Growth and Differentiation	GO/rGO-coated substrates for fibroblasts proliferation	Ryoo et al. [41]
	G/chitosan hybrid films as scaffolds for tissue engineering	Fan et al. [42]
	G surfaces for hMSC[j] neuronal differentiation	Park et al. [43]
	G surfaces for hMSC osteogenic differentiation	Nayak et al. [44]

[a] ssDNA: single strand DNA
[b] G: Graphene
[c] cDNA: complementary DNA
[d] Pseudomonas Aeruginosa
[e] FRET: fluorescence resonance energy transfer
[f] rGO: reduced graphene oxide
[g] LDI-MS: Laser desorption ionization – mass spectroscopy
[h] lPEI: linear polyethylienimine
[I] bPEI: branched polyethylenimine
[j] hMSC: human mesenchymal stem cells

1.3.1 Carbon allotropes as antimicrobial nanomaterials

Graphene can give rise to different geometries based on the rearrangement of its 2D planar structure. Different spatial configurations of the same material are called allotropes. These configurations are extremely important at the nanoscale level since the interactions between nanomaterials and living organisms vary upon the surface morphology and its architecture.

Most allotropic forms of carbon, like fullerenes, graphite and carbon nanotubes (CNTs), were soon identified as moderately toxic to most living cells, especially against bacteria. This behavior might be due to their hydrophobic character or to the generation of reactive oxygen species (ROS) causing oxidative stress at the cellular level. Furthermore, since carbon-based nanomaterials are often synthesized in the presence of metallic catalysts, heavy metals particles inclusions can also affect cellular toxicity [4].

In this light view, graphene-related materials could be potentially used for the development of novel antimicrobial nanomaterials. Indeed, most of these nanomaterials can potentially display antimicrobial properties, even though this inherent feature is strongly influenced by surface chemistry, structure and dispersion state of nanomaterials, as such parameters directly impact the possibility to interact with bacterial cells.

1.3.1.1 Graphite

Graphite is the most commonly used carbon allotrope (CA), easy and inexpensive to obtain since it occurs naturally in this form and is the most stable configuration of CA under standard conditions of temperature and pressure. According to ISO/TS 80004-13:2017, graphite consists of at least 11 graphene layers stacked in an ordered AB sequence and linked through each other via Van der Waals interactions between delocalized π orbitals (Figure 1.7).

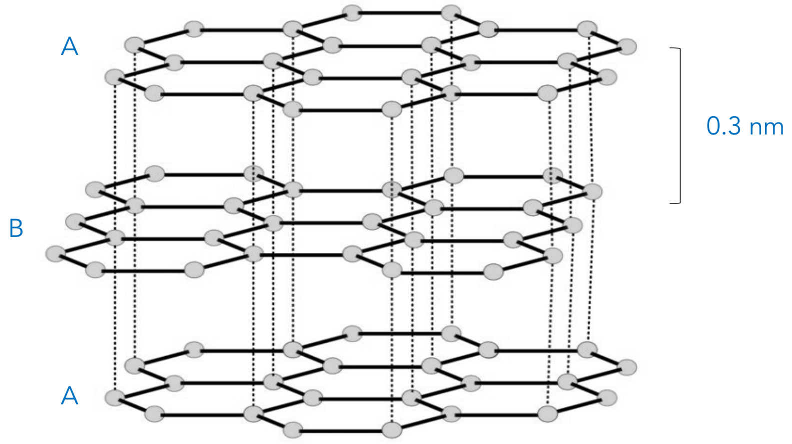

Figure 1.7 - Layered structure of graphite. Grey dots represent C atoms. Black lines represent covalent bonds between carbon atoms. Each layer is linked through Van der Waals interactions between delocalized π orbitals of hexagonal rings (link not represented).

Graphite is an anisotropic material. Covalent bonds, together with sp^2 hybridization within each layer, make such material mechanically strong and extremely conductive along the planes, while Van der Waals forces between layers enable to slide and detach graphene sheets, making graphite a good lubricant and the perfect material for pencils [45].

Similar to all carbon-based materials, graphite is extremely hydrophobic, therefore, it is imperative to take into account its dispersion state. Over the last years, several dispersing methods have been proposed to enhance graphite solubility: oxidation of graphene layers using oxidizing acids seems to be the most promising method for large-scale production [4], although few drawbacks regarding the generation of structural defects have been reported: the oxidation process causes a massive disruption of the covalent bonds of the basal plane changing graphite intrinsic properties. Even if oxides can be removed through reduction processes, the original graphite structure will not be recovered [46].

The antibacterial activity of graphite was studied in 2011 by Liu et al. [34]. In this work the authors report a substantial higher bactericidal effect of graphene samples with respect to graphite counterparts against *E. coli* cells. Their findings clearly evidence the importance of the dispersion state and the influence of stacks lateral dimension on the antibacterial activity of graphene-related materials: this paper suggests that the higher solubility of graphene in aqueous solvents facilitates the interaction with bacteria in suspension. Furthermore, whereas thick stacks of graphite difficultly pierce through bacterial cells wall and membrane, thin edges of graphene easily penetrate bacterial external structures causing a massive phospholipid removal and leading to cell lysis [47].

1.3.1.2 Carbon Nanotubes

Carbon nanotubes (CNTs) are represented by hollow structures with an extremely high aspect ratio generated by rolled graphene sheets. For this reason, the atomic structure of CNTs is the same as graphite, with carbon atoms arranged to form hexagonal rings linked to each other through covalent bonds.

CNTs can be categorized as *single-walled carbon nanotubes* (SWCNTs) and *multi-walled carbon nanotubes* (MWCNTs). The latter can be described as a group of SWCNTs concentrically nested inside each other (Figure 1.8).

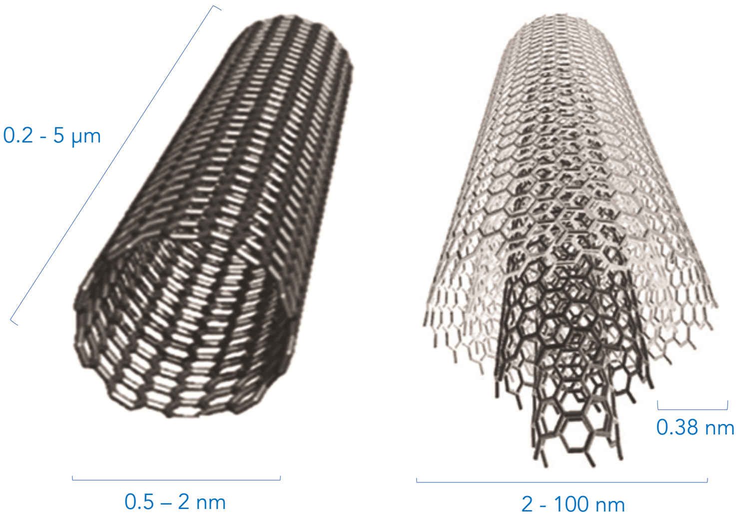

Figure 1.8 – SWCNT on the left, MWCNT on the right. The reader can appreciate the dimensions which confer nanotubes their characteristic high aspect ratio.

CNTs can be artificially synthesized by means of different methods, such as laser ablation of graphite target or chemical vapor deposition. Unlike graphite, scale-up limitations of synthesis and, most of all, purification processes, make the large-scale production of this nanomaterial expensive, thus hampering their applications.

Nevertheless, their remarkable mechanical and physical properties, together with their low density, make CNTs an excellent candidate for composite reinforcement, energy and electronics sectors [48], [49].

Regarding the dispersion state, unfunctionalized CNTs are amphiphobic, which means they are nearly insoluble in most solvents [4], [50], even if the presence of functional groups on their surfaces, as well as their entanglements, strongly influence their dispersibility in different media [51].

The high aspect-ratio and the presence of metallic elements deriving from their synthesis are responsible for the high cytotoxic activity of CNTs against both prokaryotic and eukaryotic cells. The latter issue is the reason why graphene is actually the preferred choice with respect to other carbon-related materials like CNTs.
The antibacterial activity of purified CNTs was firstly evaluated by Kang et al. in 2007 against *E. coli* cells [52], demonstrating the strong bactericidal effect of SWCNTs. The same group reported higher toxicity for SWCNTs against MWCNTs, suggesting a structure-dependent bactericidal mechanism of action in this case too [4].

1.3.1.3 Carbon Black

Carbon blacks (CBs) derive from the incomplete combustion of heavy petroleum and are widely used as a reinforcing filler in tires and rubber products. Among the different CA, carbon black is the only one reported as possibly carcinogenic to human health by the International Agency for Research on Cancer (IARC).

CBs structure can be described as several graphene layers stacked together like graphite, but with completely random orientation (i.e. without ordered AB sequence of graphene layers). This configuration of layers is known as turbostratic and well describes the intimate structure of CBs. Therefore, this nanomaterial exhibits a mesomorphic architecture, since it is not completely amorphous nor crystalline.

Moving to a lower level of magnification, electronic micrographs of CBs reveal a clustered design, with capsules as building blocks linked together. Several studies suggested specific aggregation models of graphene layers from which capsules generate [53] (Figure 1.9).

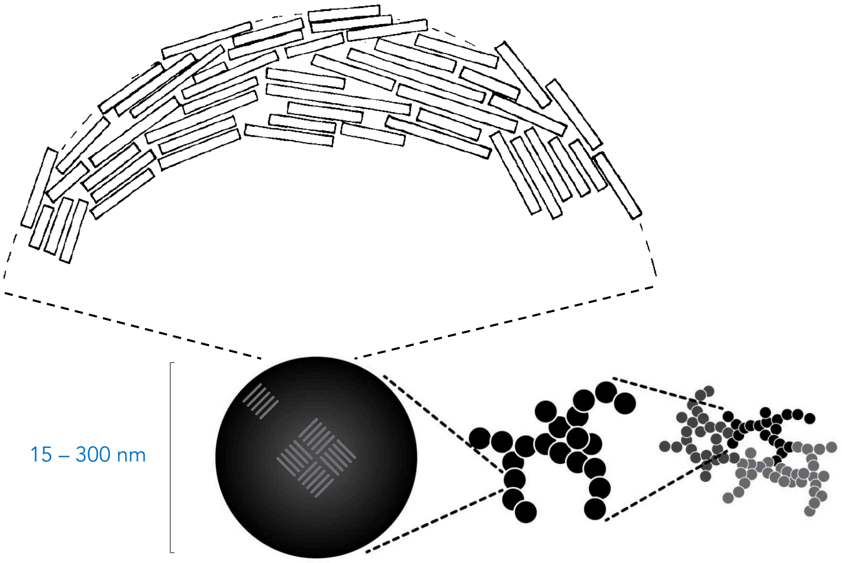

Figure 1.9 - Schematic representation of carbon black nanometric structure. White large boxes represent sections of graphene layers; black spheres represent carbon black capsules.

As for graphite and CNTs, carbon black is a hydrophobic material difficult to disperse in most of the solvents.

Unlike graphite and CNTs, antimicrobial properties of pristine CBs are the less investigated due to the fact that its widely reported pulmonary toxicity prevented for years the use of CBs as antibacterial nanomaterial. However, in recent years a correlation between surface area and cytotoxic potential of CBs has been reported, suggesting that low dosage use of ultra-fine particulate can successfully hamper its pneumotoxic effect [54]. This finding could pave the way for an extensive research on the use of CBs as antibacterial nanomaterial while not affecting eukaryote cell viability.

1.3.2 Graphene functionalization

One of the most promising and exploited graphene features is its versatility. The capability to arrange in different nanostructured shapes to form allotropes is extremely useful, since it allows the generation of diverse nanomaterials with peculiar intrinsic physico/chemical properties, starting from the same basic chemical structure.

Moreover, it is possible to increase this extraordinary versatility enriching its aromatic structure with specific molecules or functional groups to grant novel characteristics or to improve already existing ones.

The aforementioned benzenic latticework distinctive of CA is indeed a nearly inert chemical structure from the biological point of view, lacking reactive moieties which could elicit unique biochemical features. For this reason, functionalization is a good method to link a broad spectrum of functional groups to the allotrope structure, extending the applicability fields of graphene-related nanomaterials.

1.3.2.1 Critical aspects of graphene functionalization

The functionalization process can be fulfilled through different methods depending on the molecules which are going to be attached to the nanomaterial.

The two critical aspects to monitor in order to obtain the desired functionalized nanomaterial are the type and the homogeneity of functionalization.

On the one hand, structural enrichment can occur in different modalities due to the peculiar structure of CA. Graphite, CBs and MWCNTs are composed of several graphene layers stacked together. For this reason, functionalizing molecules can bind the carbon structure on the allotrope surface but also intercalate between graphene layers. In the first case, the obtained functionalized product is a *surface* *compound*, in the second case is an *interstitial compound*. A third possible outcome refers to *substitutional compounds*, which occur when an element or a small molecule with a great chemical affinity to the aromatic structure succeeds to substitute a carbon atom inserting in the latticework [45].

On the other hand, homogeneous functionalization is fundamental to design the final product. Therefore, in order to obtain good molecular tailoring, it is necessary to achieve a proper distribution of functionalizing moieties. This is a challenging issue in the treatment of graphene-based nanomaterials: π delocalized electrons typical of benzenic structure are not easily accessible to covalent bonding with foreign molecules, hence, functionalization preferentially occurs at the layer's edges or in the presence of local structural defects where carbon atoms exhibit free valence electrons [45].

1.3.2.2 Functionalization to enhance solubility of graphene

Since the hydrophobic nature of carbon-based materials prevents a proper dispersion, especially in polar solvents, the achievement of a good dispersion state is fundamental for the physical handling of graphene-related materials [4], [55]. Indeed, these nanomaterials tend to form large aggregates in an aqueous environment making it difficult to obtain a homogeneous dispersion for the evaluation of antimicrobial activity and, above all, diminishing surface area exposed to prokaryote organisms hampering their antimicrobial efficacy.

Even if this detrimental formation of aggregates can be temporarily solved applying mechanical forces, usually through bath or probe sonication, long-term stability is nearly impossible to achieve with these methods unless a proper - generally cytotoxic - solvent is used [29], [32].

The most prominent and common way to obtain stable suspensions in aqueous solvents involves the enrichment of CA with polar functional groups. This process aims at providing graphene latticework with polar moieties like hydroxyl (-OH), carboxyl acid (-COOH) and epoxide (-O-) functional groups, highly improving compound hydrophilicity. The resulting product is the so-called *graphene oxide* (GO) and refers to a single carbon layer functionalized with polar functional groups (Figure 1.10). Despite that, while intercalation compounds provided with polar molecules between graphene layers make it possible to obtain a stable colloidal solution on the one hand, on the other hand surface functionalization of graphene flakes often leads to structural defects altering mechanical and electrical properties [32].

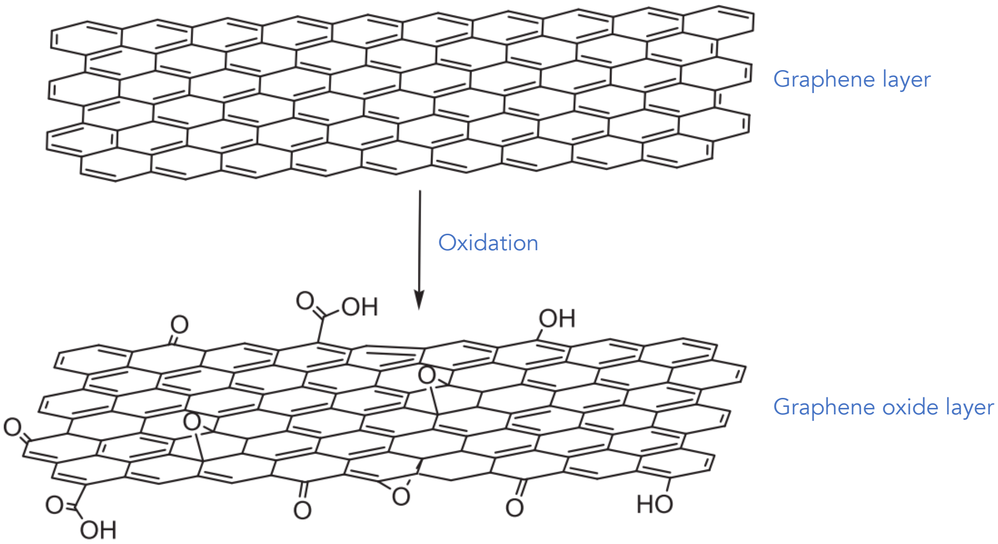

Figure 1.10 - Simplified representation of the oxidation process of graphene layers. Functionalization mainly occurs on the layers' edges due to the presence of free valence electrons. Image modified from [V. Singh, D. Joung, L. Zhai, S. Das, S. I. Khondaker, and S. Seal, "Graphene based materials: Past, present and future," Prog. Mater. Sci., vol. 56, no. 8, pp. 1178–1271, 2011, DOI: 10.1016/j.pmatsci.2011.03.003.]

In order to comply with the crescent request of graphene and its unique properties useful for particular biomedical applications (e.g. electronical conductivity and mechanical flexibility for sensors), impressive research activity is being performed on functionalized graphene-related materials in order to improve their solubility keeping their features as unchanged as possible [26], [55].

1.3.2.3 Metal ions functionalization to enhance antimicrobial properties of graphene

Even though high fractions of oxidizing functional groups could improve graphene-related materials solubility, the loss of intrinsic features related to this tailoring is an undesirable effect. Conversely, a low oxidation of these hydrophobic materials would inevitably lead to lower dispersibility, therefore the interactions with bacteria will be consequently diminished. The loss of bactericidal efficacy due to the lack of oxidizing moieties was reported by Liu et al. [47], who suggested a correlation between the dispersion state of materials, their sizes and their bactericidal efficacy. Keeping these behaviors in mind, characteristic of the whole family of graphene-related materials, a possible approach to obtain enhanced and focused antimicrobial activity is to functionalize graphene layers with bactericidal NPs together with mild oxidation to grant a proper, though not optimal, dispersibility.

Since graphene-based materials structure is relatively inert, the direct bonding between metal NPs and aromatic latticework difficultly occurs. Therefore, functionalization with oxygen-containing groups acquires a second role, serving as a linker between the graphitic structure and bactericidal NPs. In this light, graphene layers could be loaded with metal ions (such as Ag or Cu), NPs, antibiotics and enzymes to improve the antimicrobial activity of graphene-related materials.

Among the wide variety of molecules and NPs which can be tailored on graphene structures, such as zinc oxide (ZnO) [14], [17] or iron oxide (Fe_2O_3/Fe_3O_4) [56], silver (Ag) is one of the most promising elements aiming to enhance its antimicrobial activity.

The effect of Ag on microorganisms has been reported since 1869 [57]. Despite several issues related to the achievement of optimal antibacterial conditions and

its relatively high cost, Ag is still an attractive option for water disinfection since it is odorless, active for long periods and unharmful to humans [5], [58].
These characteristics led to the clinical use of metallic Ag especially for prophylactic treatment of burns, while its usage in the simple form of salts leads to high concentrations of Ag^+ ions, which is precipitated by chloride and proteins giving rise to mild undesirable effects [58]. These phenomena are simply avoidable preventing Ag from dissociation into Ag^+ ions, bearing in mind that metallic silver could elicit an antimicrobial effect too [5].

As a result, many researchers exploited Ag NPs to decorate graphene-based materials for antibacterial purposes [23], [25], [59]–[65], with GO and CNTs as the preferred choice for the scientific community. Moreover, the mechanisms underlying Ag bactericidal activity have been recently clarified through a detailed chemical genetic screen by Gugala et al. [66], paving the way for a more effective use of this antibacterial element.

Table 1.2 - Experimental features and antimicrobial efficacy of Ag-functionalized Graphene based materials.

Material	Bacterial strain	Evaluation method	Concentration [μg/ml]	Inhibition [%]	Reference
GO-Ag	E.coli	OD[f] (MIC[g])	500	100	[23]
	S.Aureus	OD (MIC)	4000	100	
CNT-Ag	E.coli	OD (MIC)	130	100	
	S.Aureus	OD (MIC)	1000	100	
GO-Ag	E.coli	PC[h] (MBC[i])	n.a.[l]	100	[59]
EG[a]-Ag	P.aeruginosa	AD[j] (ZOI[k])	n.a.	4.7 mm	[61]
	S.aureus	AD (ZOI)	n.a.	4.2 mm	
GO-Ag	E.coli	AD (ZOI)	50 ([Ag])	1.5 mm	[25]
	S.aureus	AD (ZOI)	50 ([Ag])	1 mm	
CNT-Ag	E.coli	AD (ZOI)	50 ([Ag])	0.8 mm	
	S.aureus	AD (ZOI)	50 ([Ag])	0.5 mm	
GO-Ag	S.Aureus	OD (MIC) - PC (MBC)	15 - 30	100	[63]
	E.Faecalis[b]	OD (MIC) - PC (MBC)	30 - 60	100	
	E.coli	OD (MIC) - PC (MBC)	15 - 30	100	
	P.Aeruginosa	OD (MIC) - PC (MBC)	15 - 30	100	
	A.baumannii[c]	OD (MIC) - PC (MBC)	6 - 15	100	
	S.Enterica[d]	OD (MIC) - PC (MBC)	30 - 60	100	
GO-Ag	P.aeruginosa	PC (MBC)	100	100	[64]
GO-Ag	S.aureus	AD (ZOI)	n.a.	21 mm	[65]
	B.subtilis[e]	AD (ZOI)	n.a.	16 mm	

[a] EG: Expholiated graphite
[b] Enterococcus faecalis
[c] Acinetobacter baumannii
[d] Salmonella Enterica
[e] Bacillus subtilis
[f] OD: Optical density
[g] MIC: Minimal inhibitory concentration
[h] PC: Plate count
[i] MBC: Minimal bactericidal concentration
[j] AD: Agar diffusion
[k] ZOI: Zone of inhibition
[l] n.a.: not available

1.4 Aim of the study

The antimicrobial activity of graphene is well established since 2010 when Hu et al. first reported the antibacterial activity of two graphene-based materials: *graphene-oxide* and *reduced graphene oxide* [67], [68]. Since that date, several studies regarding the enormous potential application of graphene for antimicrobial purposes have been published and scientists still devote their efforts to look for the optimal graphene nanocomposite [17], [20], [32], [49], [51], [52]. Apart from these promising results, few studies reported significant controversial results about graphene intrinsic antimicrobial properties [70], [71], suggesting a tremendous influence of the experimental culture medium.

Despite their remarkable characteristics, graphene-related materials are characterized by a hydrophobic nature which prevents their solubilization in most of the solvents hindering several features, therefore, polar molecules need to be grafted on their structure to improve solubility. In addition, these polar molecules could potentially behave as a binding site for additional functionalizing entities, highly extending the fields of application of graphene-related materials.

The aim of this work is to synthesize, characterize and evaluate the antimicrobial activity of three different CA (i.e. Graphite, Multi-walled carbon nanotubes and Carbon black) functionalized through a sustainable and green process with an artificial oxidizing molecule - whose production process has been recently published and patented by the chemistry group of Professor Galimberti (ISMaterials) at the Politecnico di Milano [26] - and Ag NPs, in order to assess whether different nanometric chemical structure and the addition of Ag could impact on bacteria viability.

Methods and experimental processes will be subdivided into 3 principal sections as reported in Figure 1.11.

Briefly: the first phase will show in detail the production process of functionalized powders, from the synthesis of the pyrrolic oxidizing compound to the final Ag-functionalized powders.

The second phase will concern the physico/chemical characterization of powders and allotrope-based suspensions through different laboratory devices and techniques.

Finally, the third phase will outline all the experimental protocols and analyses followed during the antimicrobial screening of the allotrope-based suspensions.

Figure 1.11 – Schematic representation of the experimental workflow.

2 Materials and Methods

2.1 Materials

Escherichia coli JM109 (DSM No. 3423) were purchased from the German Collection of Microorganisms and Cell Cultures (DSMZ, Braunschweig, Germany).

High surface area graphite (HSAG) Graphite Nano 307 (SA = 335 - 365 m^2/g, Particle size distribution: 0.20 – 20 μm, Purity > 97%) was purchased from Asbury Graphite Mills Inc. (Kittanning, US). Chemical composition determined from elemental analysis was, as wt%: carbon 99.5, hydrogen 0.4, nitrogen 0.1, oxygen <0.05 (Elemental analysis was performed with a Thermo FlashEA 1112 Series CHNS-O analyzer after samples were pretreated in an oven at 100 °C for 12 h.). Brunauer-Emmett-Teller (BET) surface area analysis was determined by applying ASTM D6556 method and was found to be 330 m^2/g.

Multiwalled Carbon Nanotubes (NC7000, SA = 250 – 300 m^2/g, Average diameter = 9.5 nm, Average length = 1.5 μm, Purity = 90%) were purchased from Nanocyl (Sambreville, Belgium). BET surface area of 275 m2/g.

Carbon Black N326 (Regal 300, SA = 78 m^2/g, Average spherical diameter = 30 nm, Purity > 95%) was purchased from Cabot (Alpharetta, US). BET surface area of 77 m^2/g.

Serinol was kindly provided by Bracco (Milano, Italy).

2,5-Hexanedione ($C_6H_{10}O_2$, MW = 114.14 g/mol) and *Sodium Nitrate* ($NaNO_3$, MW = 84.99 g/mol) were purchased from Merck KGaA (Darmstadt, Germany).

Silver Nitrate (AgNO3, MW = 169.87 g/mol) and *Ammonia solution* (NH_4OH, 30% v/v) were purchased from Carlo Erba Reagents (Cornaredo, Italy).

Acetone (C_3H_6O, MW = 58.08 g/mol), *Propylene Glycol* ($C_3H_8O_2$, MW = 76.09 g/mol), Sodium Hydroxide (NaOH, MW = 39.99 g/mol), Potassium Chromate (K_2CrO_4, MW = 194.19 g/mol), *Dulbecco's Phosphate Buffered Saline* (PBS), *Luria-Bertani* (LB) *broth* powder (Tryptone 10 g/L, Yeast extract 5 g/L, NaCl 5 g/L), deuterated chloroform ($CDCl_3$, δ_H= 7.26 ppm), dimethyl sulfoxide (DMSO-*d*6, δ_H= 2.50 ppm) and *Agar* powder were purchased from Sigma-Aldrich (St. Louis, US).

Polycarbonate (PC) resin was purchased from Vernici Caldart (Bellusco, Italy).

2.2 Production process – Phase 1

In our thesis work, sp^2 CA were functionalized through a double-step process: the first step provided allotropes with a functionalizing molecule, namely the serinol pyrrole (SP), in order to increase allotrope's hydrophilicity creating at the same time several binding sites for Ag NPs that will be grafted on the graphitic structure; the second step regards the Ag NPs addition, aimed to enhance the antimicrobial potential of the allotropes.

Every step described below (chapter 2.2.2 and 2.2.3) was performed on Graphite Nano 307, Multi-Walled Carbon Nanotubes NC7000 and Carbon Black N326.

2.2.1 Synthesis of serinol pyrrole (SP)

2-(2,5-dimethyl-1H-pyrrol-1yl)-1,3-propanediol (serinol pyrrole, SP) (Figure 2.1) is a molecule belonging to the pyrrole compounds family, obtained from the reaction of 2-amino-1,3-propanediol (serinol, S) with 2,5-hexanedione (HD) (Figure 2.2).

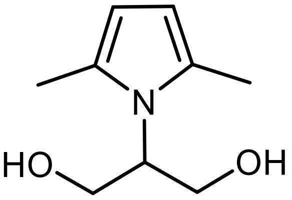

*Figure 2.1 - Chemical structure of 2-(2,5-dimethyl-1*H*-pyrrol-1yl)-1,3-propanediol (serinol pyrrole, SP).*

The synthesis of SP was performed through a Paal-Knorr reaction, recently described by Barbera et al. [26], [72], and was performed following a patented process of synthesis [73] in a completely sustainable and eco-friendly way, without solvents or catalysts and with only H_2O as a byproduct.

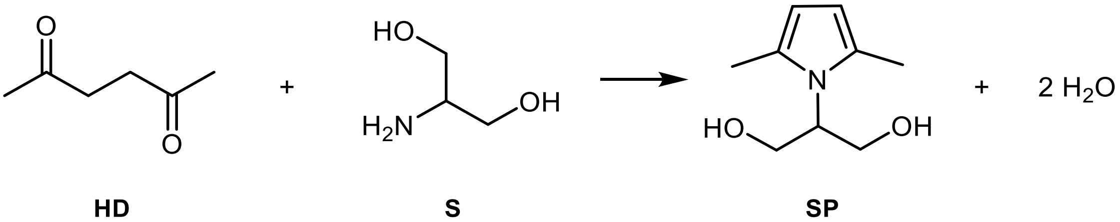

Figure 2.2 - Reaction pathway for the synthesis of serinol pyrrole (SP)

Briefly, 6.46 g of serinol powder (MW = 91.11 g/mol) were poured inside a round bottomed flask equipped with a magnetic stirrer and heated at 155°C for 15 minutes under shaking, then 8.10 g of 2,5-hexanedione (MW = 114.14 g/mol) was added dropwise to the liquid serinol.

The obtained solution was stirred for 2 hours in the same flask equipped with a reflux condenser to avoid sample evaporation. The condenser was then removed and the solution heated for an additional hour (Figure 2.3).

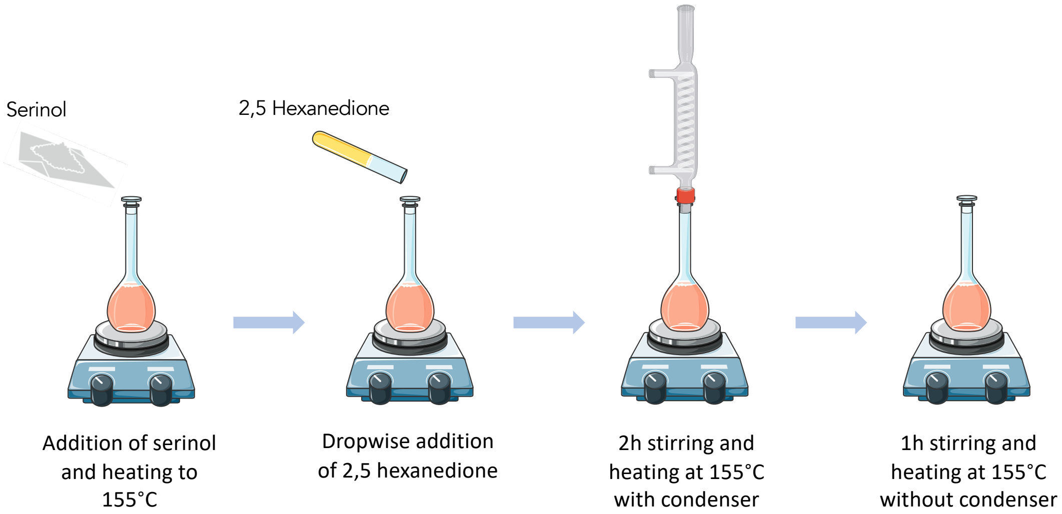

Figure 2.3 - Sustainable synthetic process of serinol pyrrole (SP).

The resulting SP (MW = 169.22 g/mol) was then recovered in a glass vial and stored at room temperature (R.T., 20 ± 1 °C) in dark conditions to avoid photodegradation. Gas Cromatography – Mass Spectroscopy (GC-MS) analysis (Agilent 5973 Inert GC-MS System, Agilent Technologies) was carried out to obtain a first insight about the reaction yield and NMR spectroscopy analysis were performed by the chemistry group of Professor Galimberti (ISMaterials) with the collaboration of the Laboratory of NMR and MS of the DCMIC "Giulio Natta" at Politecnico di Milano to identify the C-H framework of SP.
The reaction yield was calculated by computing the area below the SP peak and dividing it by the total area (Equation 2.1).

$$SP\ synthesis\ yield = \frac{SP\ peak\ area}{Total\ area}$$

Equation 2.1 - Equation for the estimation of SP synthesis reaction yield in a GC/MS analysis.

^{1}H NMR and ^{13}C NMR spectra were recorded respectively on a Bruker 400 MHz and a 100 MHz, and on a Varian Unity (400 MHz) instrument. Chemical shifts were reported in ppm with the solvent residual peak as internal standard (DMSO-d$_6$: δ_H = 2.50 ppm, CDCl$_3$: δ_H = 7.26 ppm). NMR analysis on newly-synthetized SP found the following spectra: ^{1}H NMR (CDCl$_3$, 400 MHz); δ (ppm)= 2.24 (s,

6H); 4 (d, 2H); 4.30 (t, 1H); 5.70 (s, 2H). ^{13}C NMR (DMSO-*d6*, 100 MHz); δ (ppm)= 127.7; 105.9; 71.6; 62; 14.
Chemical shifts are given in ppm against or with TMS as internal standard.

2.2.2 sp^2 carbon allotropes functionalization with SP

SP previously synthesized was used to functionalize the three raw CA. The enrichment occurred through a cycloaddition domino reaction described in detail by Barbera et al. [72].
To obtain a proper solubility enhancement, a 10% (w/w) functionalization with SP oxygenated moieties was chosen as a right trade-off in order to grant a sufficient amount of Ag-linking sites whilst keeping unaltered the carbon latticework of the allotropes, which could have altered their intrinsic mechanical and electrical properties.

Briefly, 2.00 g of CA and 0.47 g of SP were poured into a glass reaction flask, then 50 mL of acetone were added.
Subsequently, the suspension was sonicated through a bath sonicator apparatus (Ultrasonic Cleaner 2200 S3, Sonica) for 20 minutes, then acetone was removed with a rotavapor machine (Rotavapor RII, BUCHI Switzerland) at 40°C and 300 mbar.
Afterwards, the dried sample was heated at 100°C, then to 180°C through a 2 hours ramp rate heat-up under shaking as summarized in Figure 2.4.

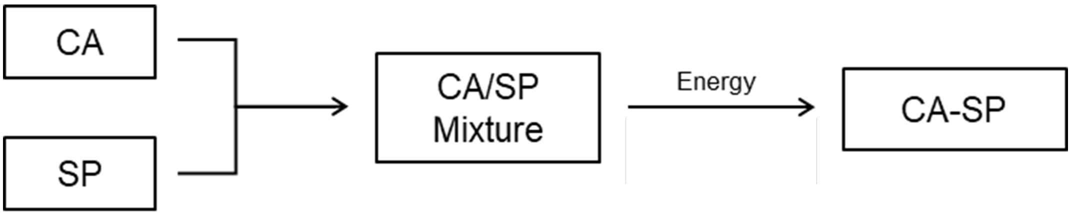

Figure 2.4 - Block diagram for the preparation of CA-SP adducts.

50 mL of acetone were then poured in the reaction flask and the sample kept overnight (ON) at R.T. under shaking.
After approximately 18 hours, the sample was recovered through vacuum filtration in a Büchner funnel and the obtained powder dried (Universal Oven UNE400, Memmert) at 90°C for 3 hours (Figure 2.5).

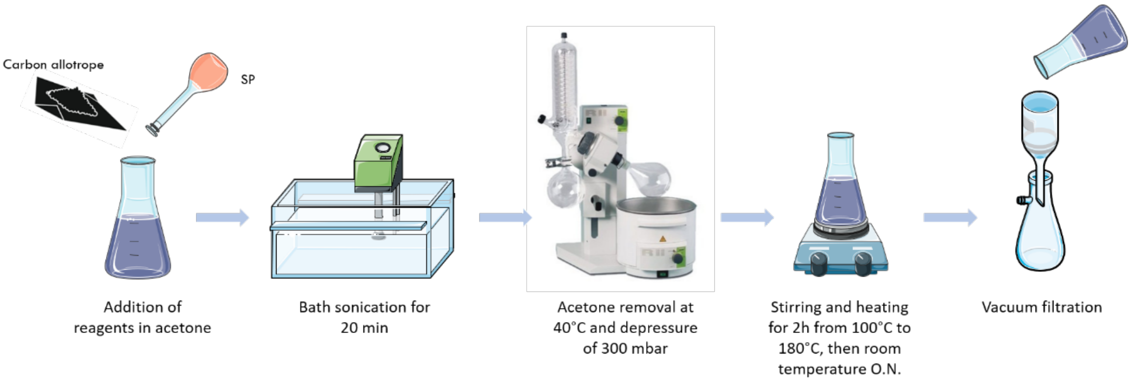

Figure 2.5 - Functionalization process: first step. Addition of SP to CA.

We will refer to these SP-functionalized compounds (Graphite + SP, Carbon Black + SP and MWCNT + SP) as the starting materials (CA-SP) from which Ag-functionalized samples (CA-SP-Ag) will be obtained. For the sake of simplicity, hereinafter these starting materials will be named respectively Graphite (G), Carbon Black (CB) and Carbon Nanotubes (CNT).

2.2.3 sp^2 carbon allotropes decoration with silver

As previously outlined, the first functionalization step with SP was followed by a second enrichment of the starting materials with Ag. In our case, functionalization was carried out by means of the Tollens' assay.

Firstly, Tollens' reagent was prepared as follows: 1 mL of a 0.6 M $AgNO_3$ solution and 1 mL of a 2.8 M NaOH solution in distilled water (dH_2O) were mixed in a glass vial causing the formation of a brown precipitate, thus, NH_4OH was added dropwise until a complete precipitate dissolution was achieved. The resulting solution is the Tollens' reagent.

A small aliquot of this reagent was next withdrawn and used to assess its functionality: 1 mg of glucose (an aldehyde) were transferred in a test tube and the Tollens' reagent added dropwise while shaking until the characteristic silver mirror appeared. The appearance of the mirror validates Tollens' reagent functionality.

Tollens' reagent was next used to functionalize our three samples (G, CB and CNT) with Ag NPs. During our work, we decided to functionalize every CA using two different Tollens' reactive doses to evaluate whether the Ag amount could influence the antimicrobial activity. Briefly, two suspensions of 250 mg of the starting material dispersed in 5 mL of dH_2O were prepared in two separate reaction tubes (15 mL falcon conical centrifuge tubes), hence, 350 µL and 650 µL of Tollens' reagent were added respectively. Therefore, two different functionalized samples were produced for each allotrope.

From now on, we will refer to them with the suffix 350 and 650: for instance, Graphite (G) functionalized with 350 µL of Tollens' reagent will be called Graphite350 (G350) and the one functionalized with 650 µL will be named Graphite650 (G650).

Each sample was next brought to volume (final volume: 7 mL) with dH_2O and centrifuged (Refrigerated Centrifuge 3-16PK, Sigma Laborzentrifugen) at 4,000 rpm for 15 minutes. Afterward, the supernatant was discarded, the pellet resuspended in 7 mL of dH_2O and the whole centrifuged. This step was repeated a last time resuspending the pellet in acetone. Wet powders were then collected in a crystallizing dish and left for drying ON at R.T. (Figure 2.6).

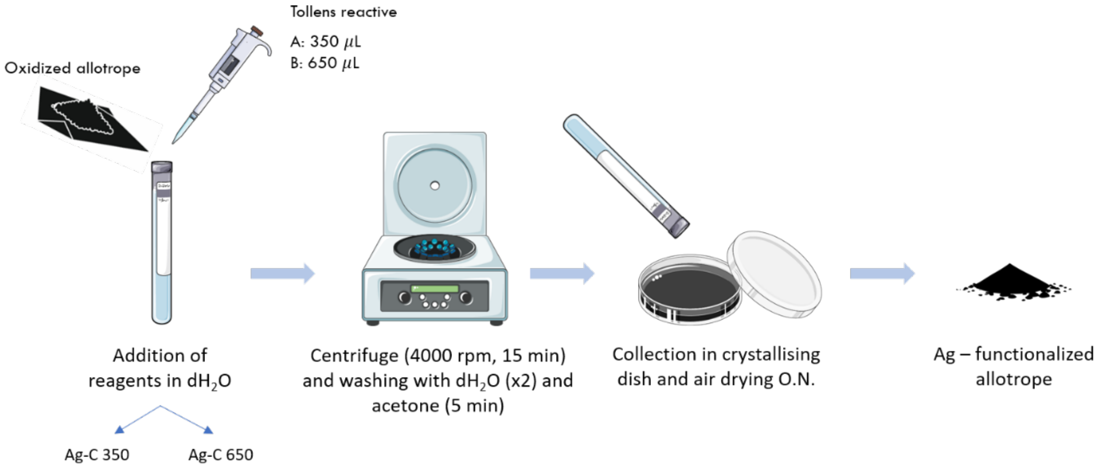

Figure 2.6 - Functionalization process: second step. Addition of Ag NPs to CA.

Dried powders were collected in glass vials and stored in dark conditions at R.T. until use.

At the end of this stage, samples were used in physico/chemical characterization test and antibacterial screenings. Ag-functionalized (CA-SP-Ag) samples are summarized in Table 2.1:

Table 2.1 - Table of available samples. On the left, a brief description of the functionalizing procedure experienced by each allotrope is provided.

Table of samples

	Graphite	Carbon Black	MWCNTs
Functionalization with SP	G	CB	CNT
Functionalization with SP + addition of 350 μL of Tollens' reagent	G350	CB350	CNT350
Functionalization with SP + addition of 650 μL of Tollens' reagent	G650	CB650	CNT650

2.3 Samples characterization – phase 2

A detailed investigation of the physico/chemical parameters of the allotropes was performed as described herein below.

The following paragraphs will focus on characterization methods used to characterize our samples from a physico/chemical point of view.

2.3.1 TGA analysis

Small amounts of each sample were collected and accurately transferred in glass vials and used for characterization of allotropes composition through Thermo Gravimetric Analysis (TGA).

Analyses were carried out by LAC (Laboratorio Analisi Chimiche) at Politecnico di Milano by means of a TGA/SDTA 851, Mettler Toledo AG, using the standard method ISO9924-1: the procedure, performed on 10 mg of CA-SP and CA-SP-Ag samples, consists in a heating ramp (10°C/min) from 30 up to 300°C, followed by 10 minutes isotherm at 300°C, then another heating ramp (20°C/min) up to 550°C and a subsequently 15 minutes isotherm at 550°C; a final heating ramp (10°C/min) up to 900°C was followed by a 20 minutes isotherm to the end of the experiment. The whole procedure was performed in N_2 atmosphere except for the last 20 minutes, in which the gas in the chamber was switched to O_2.

Obtained data were used to get allotropes composition in terms of weight percentages through an automated electronic datasheet (Microsoft Excel, Microsoft Office 2019).

2.3.2 HRTEM analysis

High Resolution Transmission Electron Microscopy (HRTEM) analyses were carried out by SAMM (Servizio di Analisi Microstrutturali dei Materiali) with a Philips CM200, Agilent Technologies, field emission gun microscope working at an accelerating voltage of 200 kV.
1 mg/mL PBS suspensions of ‘650 samples (i.e. G650, CB650 and CNT650) were prepared and few drops were poured on a lacey carbon-coated film on a 200-mesh copper grid and air-dried for several hours. Low beam current densities and short acquisition times were employed.

Micrographs were analyzed through ImageJ, NIH, in order to perform a dimensional analysis on aggregates, Ag NPs and allotropes characteristic structures: after calibrating micrographs through the scalebar provided by HRTEM software, a reasonably high number of entities (approximately 20) was measured and statistically analyzed calculating mean, minimum, maximum values and standard deviations.

An additional analysis was carried out by means of Gatan Microscopy Suite in order to evaluate interplanar spacing between graphene layers for each allotrope: after dimensional calibration, a Fast Fourier Transformed (FFT) filter was applied on a portion of the HRTEM higher magnification micrographs in which a repetitive pattern was visible. The resultant filtered image was further analyzed isolating bright spots and subsequently an Inverse Fast Fourier Transformed (IFFT) filter was used to point out a clear periodic pattern; the interplanar spacing was finally identified calculating the period of the repetition (Figure 2.7).

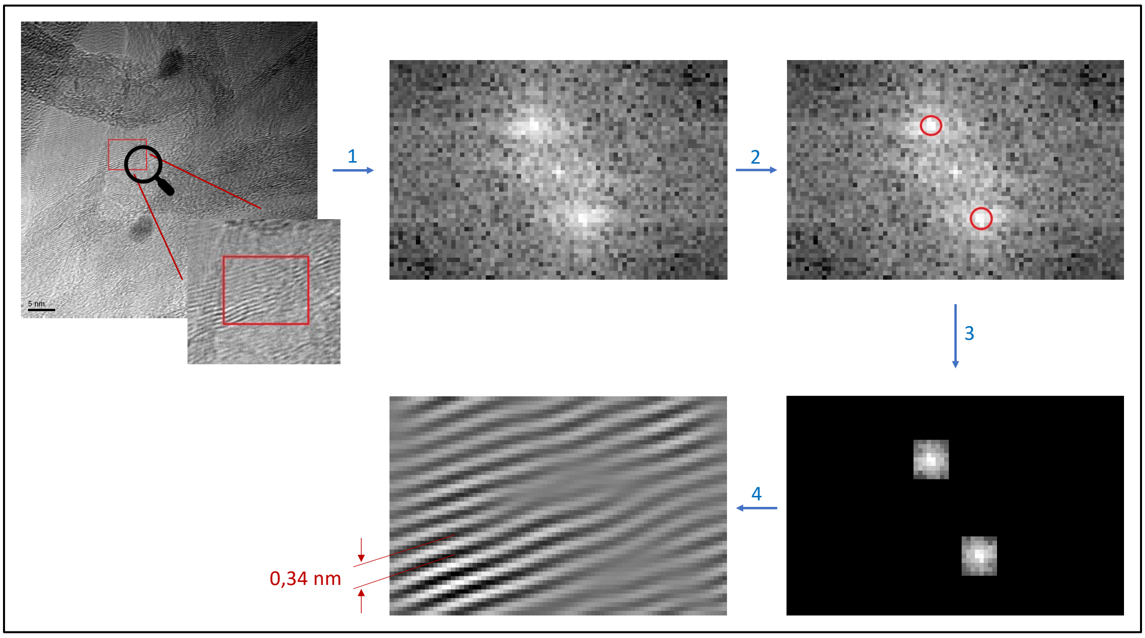

Figure 2.7 - Image processing workflow. 1: Application of FFT filter on the chosen image portion (red square in the first picture). 2: Individuation of bright spots relative to repetitive patterns. 3: Application of a mask to isolate bright spots. 4: Application of IFFT filter to evidence repetitive patterns; interplanar spacing is computed as the distance between two consecutive dark lines.

2.3.3 Wide angle X-ray diffraction analysis (WAXD)

XRD analyses were carried out by the research group of Professor Galimberti (ISMaterials). WAXD patterns were obtained in reflection, with an automatic Bruker D8 Advance diffractometer, with nickel filtered Cu–K_α radiation. Patterns were recorded in 4° – 90° as the 2θ range, being 2θ the peak diffraction angle. The d interplanar distance between crystallographic planes of sp^2 CA was calculated from the Bragg's law (Equation 2.2):

$$d = \frac{n\lambda}{2\ \sin\theta}$$

Equation 2.2 - Bragg's law.

where λ is the wavelength of the irradiating beam (1.5419 Å, Cu-K_α), θ is the diffraction angle and n is a positive integer number.

The $D_{hk\ell}$ correlation length, in the direction perpendicular to the hkl crystal graphitic planes, was determined applying the Scherrer equation (Equation 2.3):

$$D_{hkl} = \frac{K\lambda}{\beta_{hk\ell} \cos(\theta_{hk\ell})}$$

Equation 2.3 - Scherrer Equation.

where K is the Scherrer constant, λ is the wavelength of the irradiating beam (1.5419 Å, Cu-K_α), $\beta_{hk\ell}$ is the width at half height, and $\theta_{hk\ell}$ is the diffraction angle. The instrumental broadening, b, was determined by obtaining a WAXD pattern of a standard silicon powder 325 mesh (99%), under the same experimental conditions. The width at half height $\beta_{hk\ell} = (B_{hk\ell} - b)$ was corrected, for each observed reflection with $\beta_{hk\ell} < 1°$, by subtracting the instrumental broadening of the closest silicon reflection from the experimental width at half height, $B_{hk\ell}$. Graphs were obtained and analyzed with the software Origin, OriginLab Corporation.

2.3.4 UV-vis spectroscopy

The stability of our suspensions was evaluated in terms of variations of light absorbance by means of a UV-visible (UV-vis) spectrophotometer (HP 8452A Diode Array Spectrophotometer, Agilent Technologies).
Tests were performed on starting powders only (G, CB and CNT) assuming that stability behaviors will be similar between pristine materials and their functionalized counterparts. Pure PBS was taken as the blank solution.

A calibration curve was obtained prior to measurements for each allotrope. Powders were dispersed in PBS at 1 mg/mL, ultrasonicated with a probe ultrasonicator (Fisherbrand Model 505 Sonic Dismembrator, Fisher Scientific) and then diluted to obtain several suspensions at known concentration of 0.5

mg/mL, 0.1 mg/mL, 0.05 mg/mL, 0.01 mg/mL, 0.005 mg/mL and 0.001 mg/mL.

Ultrasonication was carried out with the following parameters:

- Duration: 5 minutes ultrasonication
- Probe dimension: 3 mm
- Volume of sonicated suspension: 5 mL
- Sonication amplitude: 30%
- Other conditions: ice cooled

Each suspension was then analyzed and relative absorbance at 300 nm recorded. Lambert-Beer law (i.e. the linear relation between concentration and absorbance values) was applied in the linear range of fitted data: calibration curves were obtained for this linear range calculating the coefficients of linear regression computed by means of the software Microsoft Excel, Microsoft Office 2019.

Afterwards, unfunctionalized allotropes suspensions (i.e. G, CB and CNT) were prepared in PBS at the same concentrations as those used for antimicrobial experiments (see chapter 2.4.2.2 – Inoculum with CA-SP-Ag suspensions) and their stability evaluated keeping the same experimental conditions.

Briefly, 1 mL (named A in Figure 2.8) was withdrawn from these suspensions, then suspensions were sonicated (with the same parameters listed above) and another 1 mL aliquot (named B in Figure 2.8) was withdrawn from these new sonicated suspensions. These aliquots, i.e. A and B, were stored at 37°C in static conditions and further analyzed through UV-vis spectrophotometer at 3 hours and 24 hours.

Ultrasonicated suspensions were quickly analyzed after ultrasonication to record their UV-vis absorbance spectrum. 3 hours kinetics were performed in order to evaluate absorbance variations during time as an estimate of suspensions stability after ultrasonication.

At the end of kinetic, the UV-vis absorbance spectrum of aliquot A and B was recorded and compared to quantitatively evaluate the influence of ultrasonication after 3 hours of static storage at 37°C. The same procedure was followed after 24 hours.

Absorbance spectra were exported as .CSV files and graphs were obtained with the software Matlab_R2019a, Mathworks (Figure 2.8).

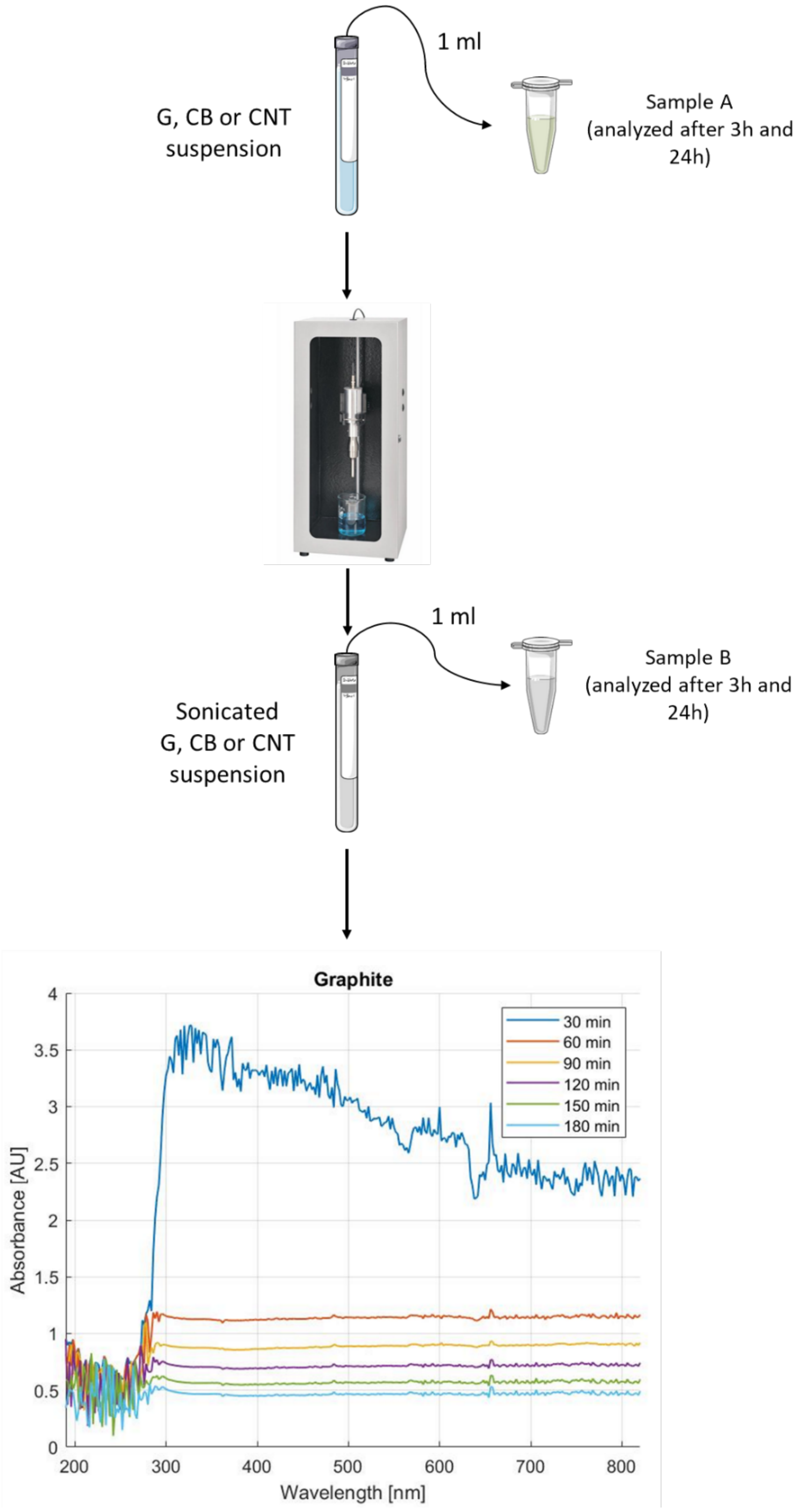

Figure 2.8 - Schematic graph of UV-vis absorbance measurements. The final output shows a typical absorbance spectrum graph obtained with Matlab_R2019a, Mathworks processing data from CSV file of sample G.

Finally, the Precipitated Mass Fraction for each allotrope at 3 hours and 24 hours was estimated.

$$A = \varepsilon \cdot b \cdot C$$

Equation 2.4 - Lambert-Beer law.

The Equation 2.4 represent the Lambert-Beer law. ε [L mol^{-1} cm^{-1}] is the molar extinction coefficient which is characteristic of the analyte: the more the coefficient is, the more the analyte has the capability to prevent light to get through it; b [cm] is the optical path length characteristic of the device.
Using parameters from the calibration curves, the supernatant concentration for each sample was computed by means of the Lambert-Beer's equation, thus, knowing the initial sample concentration (i.e. the concentration at which the sample was prepared and tested), the percentage of precipitated mass was calculated at 3 hours and 24 hours as shown by the following equation:

$$Precipitated\ Mass\ Fraction_t = \frac{C_0 - C_t}{C_0} \cdot 100\%$$

Equation 2.5 - Equation for the estimation of the Precipitated Mass Fraction at a specific time step t (3 hours or 24 hours) from the initial sample concentration C_0 and supernatant sample concentration C_t at time step t.

2.3.5 DLS and ELS measurements

Colloidal suspensions of G, CB and CNT samples were next analyzed through Dynamic light scattering (DLS) and Electrophoretic light scattering (ELS) to evaluate their sizes and surface charge in terms of their hydrodynamic diameters (D_H) and Zeta potential (ζ_P) respectively.

Suspensions of each sample were firstly prepared in PBS at a concentration of 0.5 mg/mL, then suspensions were diluted in separate test tubes up to 0.05 mg/mL and 0.005 mg/mL respectively to evaluate the optimal concentration for both type of measurements.

Once the best concentration was chosen (0.5 mg/mL for G and CB samples, 0,05 mg/mL for CNT samples) particles dimensions were measured under three different experimental conditions for each allotrope: not-sonicated sample in PBS, ultrasonicated sample in PBS, ultrasonicated sample in 50% v/v LB/PBS (Figure 2.9).

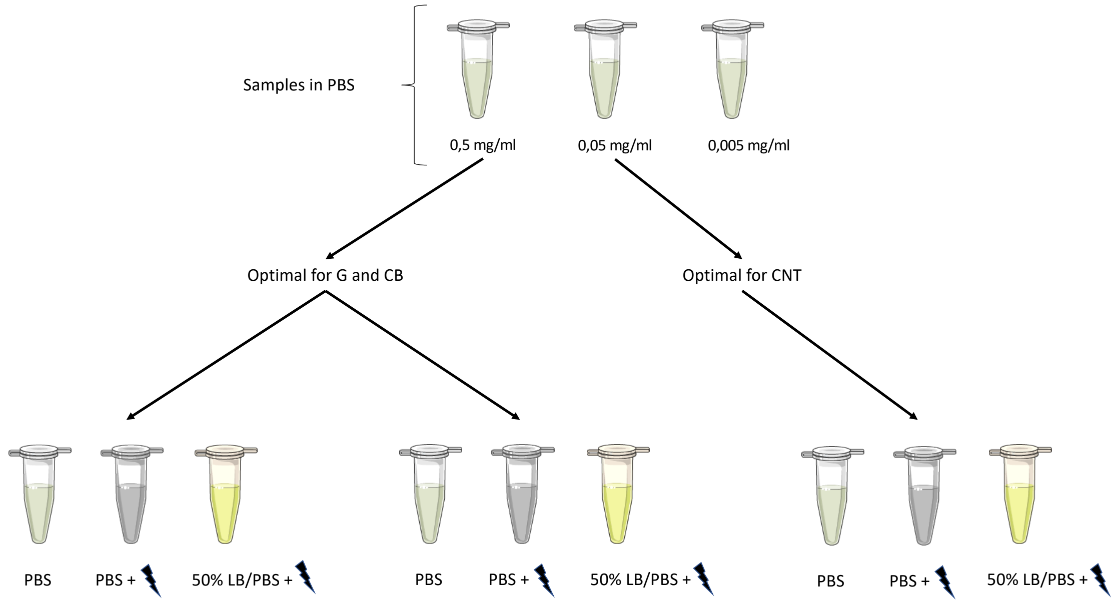

Figure 2.9 - Schematic graph of DLS and ELS measurements workflow. The best concentration was evaluated for samples diluted in PBS, therefore, optimal concentration was used to test samples diluted in PBS (not sonicated and sonicated) and 50% LB/PBS (sonicated).

DLS measurements were carried out with a Zetasizer Nano ZS, Malvern Instruments with the following parameters:

- Type of measurement: Hydrodynamic Diameter (D_H)
- Analyzed volume: 500 µL
- Cuvette type: Low volume disposable (ZEN 0112)
- Attenuation: manual, 8
- Temperature: 25°C
- Material: Graphene
- Number of measurements: 3
- Number of runs per measurement: 10

Aside from D_H, the ζ_P of suspended particles was analyzed by means of ELS using the same device (Zetasizer Nano ZS, Malvern Instruments) with the following parameters:

- Type of measurement: Zeta Potential (ZP)
- Analyzed volume: 600 µL
- Cuvette type: Low volume disposable (DTS 0012)
- Attenuation: automatic
- Temperature: 25°C
- Material: Graphene
- Number of measurements: 3
- Number of runs per measurement: 10

All measurements for each sample and method were done at least in triplicate (see Number of measurements in parameters). Ordinary one-way ANOVA tests were performed by means of the software GraphPad Prism 8 comparing results derived from the three tested experimental conditions for each allotrope and for each measurement (i.e. D_H and ζ_P). Significance levels (α) were set at 5%, thus confidence interval was 95%).

2.3.6 Ag^+ ions detection assay

In order to quantify the amount of Ag^+ ions released from CA-SP-Ag suspensions, a titration assay for Ag^+ ions detection based on the spectrophotometric quantification of sodium chromate (CrO_4^-) concentration was performed.

First, 7 mL of CA-SP-Ag 650 suspensions (i.e. G650, CB650, CNT650) diluted in PBS were prepared at the following concentrations: 0.90 mg/mL for G650, 0.81 mg/mL for CB650 and 1.25 mg/mL for CNT650 (equal to those used during antimicrobial screening tests). An $AgNO_3$ 2000 µM solution was analyzed in parallel to CA-SP-Ag 650 suspensions as a control test following the same procedure.

These samples were stored at 5°C for 24 hours. Suspensions were further ultrasonicated (Fisherbrand Model 505 Sonic Dismembrator, Fisher Scientific – 5 minutes; 3 mm probe; 5 mL volume; 30% amplitude, ice-cooled) and centrifuged (Refrigerated Centrifuge 3-16PK, Sigma Laborzentrifugen – 4000 rpm, 5 minutes) to separate pellet from the supernatant. 5 mL of the last one were collected in a separate test tube and added with 5 mL of K_2CrO_4 2.4 mM. The solution was next mixed through a vortex tube shaker (Vortex Mixer EMXS, EuroClone) for 6 times every 3 minutes. Afterward, the solution was centrifuged again and the supernatant was discarded keeping the red pellet (Ag_2CrO_4).

Then, 2 mL of $NaNO_3$ 0.25 M were added to the red pellet (Figure 2.10) and the whole vortexed 6 times every minute. Samples were then centrifuged (4000 rpm, 5 minutes) and the supernatant discarded. These last processes were repeated twice (from $NaNO_3$ addition) and the supernatant kept for further UV-vis absorbance measurements.

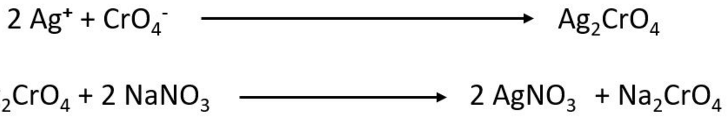

Figure 2.10 - Ag+ ions titration assay: the first reaction occurs when chromate anion is added, while the second reaction is caused by the further addition of $NaNO_3$ to the red precipitate.

UV-vis measurements were performed by means of a spectrophotometer (HP 8452A Diode Array Spectrophotometer, Agilent Technologies) and absorbance values at 375 nm recorded. All measurements for each sample were performed at least in triplicate.

Ag^+ ions concentrations were derived from a calibration curve previously obtained by the chemistry group of Professor Galimberti (ISMaterials).

The whole assay was further repeated substituting PBS with dH_2O in order to avoid issues related to the presence of ions derived from salts in PBS (for instance, NaCl).

2.4 Antimicrobial activity of CA-SP-Ag suspensions – Phase 3

In this paragraph, a detailed description of the antibacterial tests will be provided. A preliminary optimization phase was performed with the aim to overcome issues related to the use of carbon-related nanomaterial during antimicrobial screening tests. Therefore, this section will firstly describe these optimization steps; afterward, the definitive optimized protocol will be presented.

2.4.1 Preliminary optimization

This section will summarize the major modifications implemented on a standard antibacterial assessment protocol (ASTM E2315-16) [74] in order to optimize the evaluation in the case of carbon-related materials suspension.

The common method for the assessment of the bacterial charge during laboratory experiments involves optical density (OD) measurements of bacteria suspensions. In our antibacterial screening tests, this evaluation method was substituted with the enumeration of viable bacteria through plate culture method performed on LB-agar Petri dishes (Ø = 100 mm) divided in four sectors (Figure 2.11).

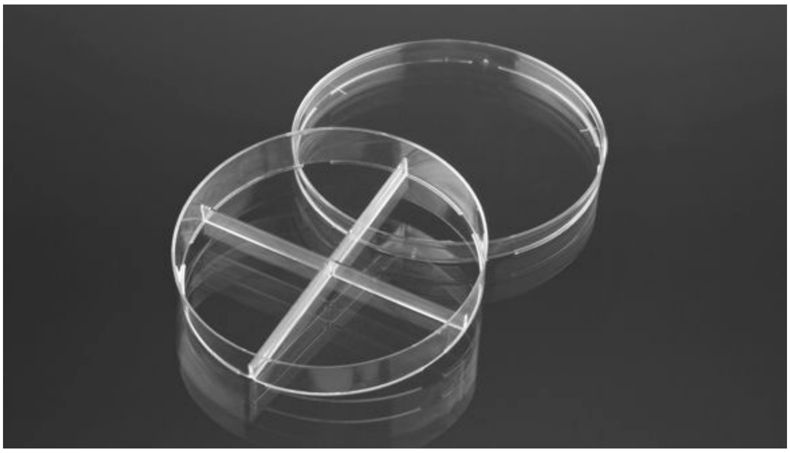

Figure 2.11 - Petri dishes (Ø = 100 mm) divided into four sectors. This configuration holds up to 4 separate samples in a single Petri dish, avoiding waste of three additional plates.

LB-agar plates were prepared starting from liquid LB-agar broth, obtained dissolving 20 g of LB broth base and 15 g of agar powder in 1,000 mL of dH_2O. The mix was magnetically stirred until a complete dissolution of powders was achieved, then the solution was sterilized by autoclaving it at 121°C for 20 minutes.

Then, 3 mL of liquid LB-A broth were poured inside each sector of Petri dishes under sterile conditions and the plates were left for drying 30 minutes without lids under the safety cabinet. The plates were next covered, stored at R.T. and used after no longer than 1 week.

The culture medium is a second fundamental parameter regarding antimicrobial screenings since the presence of nutrients, salts, and proteins strongly affect bacterial behavior and their interactions with nanomaterials. In our case, we used a 1% (v/v) diluted LB in PBS as culture medium instead of pure LB.

LB liquid broth was prepared dissolving 20 g of LB broth base in 1,000 mL of dH_2O. The mix was magnetically stirred until a complete dissolution of powders was achieved, then the solution was sterilized by autoclaving it at 121°C for 20 minutes.

2.4.2 Antimicrobial evaluation protocol

Antimicrobial screening tests were aimed to assess the antibacterial efficacy of our compounds, i.e. G, CB, CNT and their Ag-functionalized counterparts (G350, G650, CB350, CB650, CNT350, CNT650) against *E. coli* JM109.

Tests, performed at least in triplicate for each material, were carried out following a standard guide for the assessment of antimicrobial activity (ASTM E2315-16) [74] modified with the implementations described in chapter 2.4.1 – Preliminary optimization.

An initial evaluation of samples sterility grade was performed to establish the absence of living contaminant species which could have altered the successful outcome of experiments: results reported no viable microorganisms inside powders.

2.4.2.1 Preparation of test inoculum

Antimicrobial properties of Ag-functionalized CA were tested against *E. coli* JM109, which is a commonly used Gram-negative bacterial strain employed as a model organism for antimicrobial screening tests.

Bacteria were cultured in 5 mL of LB broth at 37°C under shaking at 135 rpm, until reaching an OD at $\lambda = 600$ nm (OD_{600nm}) ≈ 0.1, approximately corresponding to 10^9 bacteria/mL. The OD was analyzed by a Nanodrop2000, Thermofisher.

Afterward, the bacterial suspension was centrifuged (Refrigerated Centrifuge 3-16PK, Sigma Laborzentrifugen – 5 minutes, 4,000 rpm) and the supernatant discarded. Bacterial pellet was resuspended in 5 mL of 2% (v/v) diluted LB/PBS and the OD of the bacterial suspension was measured again to confirm the initial concentration. Therefore, the bacterial suspension was diluted to reach the desired *microbial population* of 10^6 bacteria/mL (Figure 2.12) and small aliquots of 20 µL plated out on LB-agar Petri dishes to verify this concentration through the plate count of viable Colony Forming Units (CFUs). This bacterial suspension will be our *inoculum suspension*.

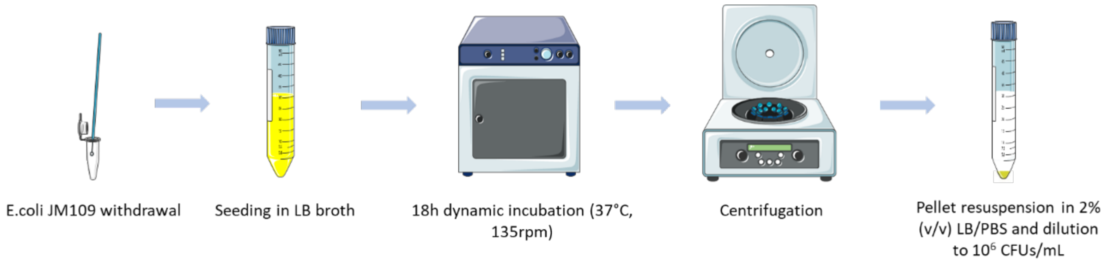

Figure 2.12 - Preparation of the inoculum suspension at 10^6 CFUs/mL bacterial concentration.

A precise weighted mass of material's powder was dispersed in 4 mL of PBS solution to obtain the desired molarity of Ag associated with each compound (4000 µM Ag). For unfunctionalized samples, i.e. pristine starting materials G, CB and CNT, an "Equivalent Ag Molarity" was estimated in order to make it possible the comparison between these pristine samples and their Ag-functionalized counterparts. Unfunctionalized compounds were prepared and tested at the same SP concentration as for '350 samples. Therefore, the Equivalent Ag Molarity will correspond to the Ag concentration that the unfunctionalized samples would have had if they had been functionalized in the same manner as for their '350 counterparts. In our opinion, this is the best way to make comparable the results of unfunctionalized and Ag-functionalized samples standardizing our screening tests on the Ag molarity.

Ag and SP moles for each sample were known relying on computation of TGA results (see chapter 3.2.1 – Analysis of Graphene-based nanomaterials composition).

Prior to 8-fold serial dilutions, samples were ultrasonicated following the procedure described in the paragraph *2.3.3*, to homogenize particles dimensions and powders dispersibility.

Afterward, the following 4 serial dilutions referred to Ag molarity (or equivalent Ag molarity for pristine samples) were prepared: 4000 µM, 500 µM, 63 µM, 8 µM (Figure 2.13).

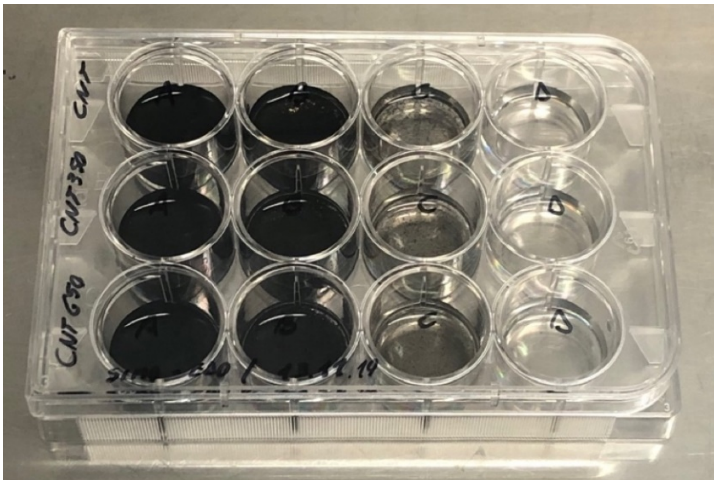

Figure 2.13 - 8-fold serial dilutions of CNT, CNT350 and CNT650 samples. Letters refer to dilutions: A = 4000 µM, B = 500 µM, C = 63 µM, D = 8 µM.

2.4.2.2 Inoculum with CA-SP-Ag suspensions

400 µL of each one of the aforementioned sample dilutions were delivered to 400 µL of bacterial suspension in sterile 2 mL eppendorf test tubes and subsequently incubated in dynamic conditions (8 rpm) at R.T. for 24 hours onto a home-made device to avoid precipitation of powders (Figure 2.14).

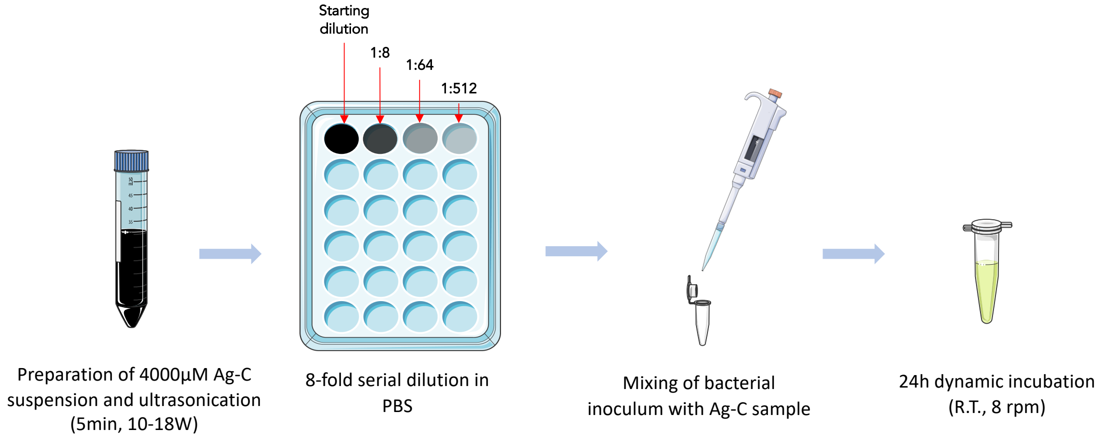

Figure 2.14 - Bacterial seeding with CA-SP-Ag suspensions: four 8-fold serial dilutions were performed for each sample and then delivered to bacteria.

The rotating system was designed with the 3D CAD software SolidWorks and holds up to 96 eppendorf test tubes (1.5 – 2 mL) (3 rotating disks, 32 eppendorf per disk). Rotation is given by a high torque 12 V DC geared motor with a maximum speed of 20 rpm. Rotational speed can be adjusted by means of a PWM electronic modulator (dimmable duty cycle from 0 to 100%) (Figure 2.15). The system was manufactured in polycarbonate in order to avoid issues related to high levels of humidity characteristic of cell incubators.

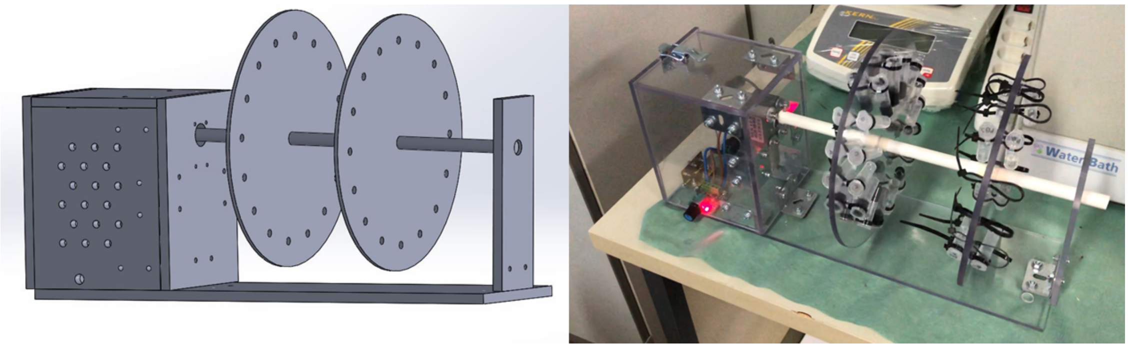

Figure 2.15 - Self-made polycarbonate device: on the left the 3D CAD model, on the right the final device. A third rotating disk could be held by the rotating shaft, not shown in the figure.

For each sample, the following 4 final dilutions referred to Ag molarity (or equivalent Ag molarity for pristine samples) were tested: 2000 µM, 250 µM, 31 µM, 4 µM.

Bacterial suspension inoculated in PBS was used as test negative control (CTRL$^-$, i.e. optimal viability conditions) whilst bacterial suspension inoculated in a 50 µM $AgNO_3$ solution was used as test positive control (CTRL$^+$, i.e. total death). The $AgNO_3$ bactericidal effect of this concentration on *E. coli* JM109 was previously tested in a dedicated experiment.

2.4.2.3 Plating and enumeration of viable bacteria

Viable bacteria were enumerated performing 10-fold serial dilutions of the inoculum of each sample in LB medium. 20 µL of each dilution (from the 2nd to the 8th column in Figure 2.16), as well as 20 µL of each inoculum from the tested specimens (TQ, the first column in Figure 2.16), were poured into separate sectors of sterile LB-agar Petri dishes. Poured drops were then spread on the LB-agar surface by means of sterile glass beads (the feasibility of a different plating method was tested separately from these experiments. Though it is not as reliable as the one eventually used, we reported its procedure in the Appendix 5.3). The whole plating procedure was performed in triplicate. Petri dishes were then incubated upside down at 37°C (R.H. > 90%) for 24 hours (Figure 2.17).

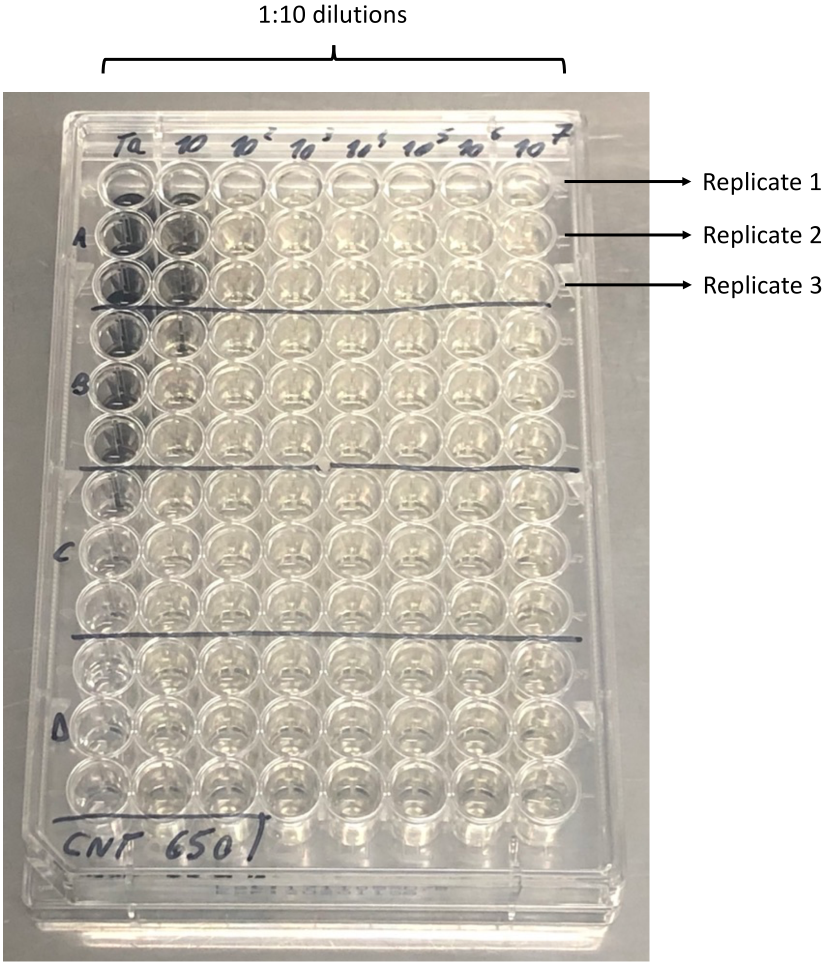

Figure 2.16 - Photograph of a 96 multiwell used for the development of 10-fold serial dilutions from TQ (sample recovered from test specimens) to $1:10^7$. The number of CFUs diminishes proportionally with dilutions, creating a range of enumerable CFUs per sector of the Petri dish. A, B, C and D refer to the four analyzed dilutions of the tested material (in this case CNT650).

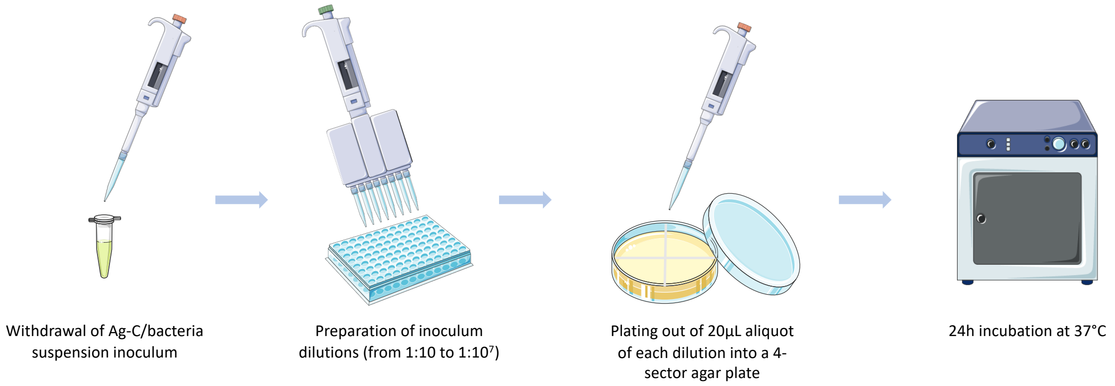

Figure 2.17 - Plating out process.

After incubation, CFUs were enumerated for each plate sector which contain from 1 to 300 of well-separated colonies. For each replicate (thus for each series of dilutions from 1:10 to 1:10^7), CFUs number from at least two significant dilutions was recorded, as well as the dilution factor used for each significant sector. Bacterial concentration (C) was calculated for each significant dilution by means of the Equation 2.6, where V is the plated volume (20 µL) and D is the dilution factor:

$$C = \frac{counted\ CFUs}{V} \cdot D$$

Equation 2.6 - Equation for the computation of the bacterial concentration C starting from the CFU count obtained during antimicrobial screening tests.

The final bacterial concentration for each triplicate was computed averaging the obtained bacterial concentration (C) of the significant dilutions.

2.4.2.4 Data processing and statistical analyses

Obtained data of concentration were reported into an automated electronic datasheet (Microsoft Excel, Microsoft Office 2019), where mean and standard deviation (SD) between triplicates were computed (see Appendix 5.2). These data were used to generate antimicrobial dose-response curves obtained by means of the software Prism 8, GraphPad Software. Experimental results were fitted with second-order polynomial, sigmoidal 4PL or log-log line curves according to the best fitting result.

The aforementioned approximant curves were eventually used to estimate the Minimal Bactericidal Concentration (MBC), defined as the minimal dose of antibacterial agent which elicits a 99.9% bacterial killing.

3 Results and Discussion

3.1 Evaluation of the production process

The aim of this thesis work is to characterize and validate the antimicrobial properties of three different sp^2 carbon allotropes (CA), namely high surface area graphite (HSAG), carbon black and multiwall carbon nanotubes (MWCNTs), functionalized with Ag NPs. To accomplish this purpose, the first step regards the synthesis of these Ag-fuctionalized derivatives: bare CA were firstly functionalized with a specific pyrrole compound, the serinol pyrrole (SP), then a second functionalization step was carried out in order to enrich materials with Ag NPs. Synthesis was followed by a physico/chemical characterization of the products, aimed to evaluate their relative composition, characteristic dimensions and precipitation stability in watery suspension. Finally, antibacterial screening tests were carried out to validate their antimicrobial activity and, specifically, the role of Ag was outlined and investigated more deeply.

In the first part of this chapter, results of the synthesis of Ag-functionalized CA will be discussed, relating them with those reported in the scientific literature: an in-depth knowledge of the reaction mechanism, a fine control of synthesis parameters and a correct evaluation of the final products are fundamental to obtain good-quality materials, necessary to properly carry out further steps of characterization and validation.

3.1.1 Synthesis of Serinol Pyrrole (SP)

Sp^2 carbon allotropes (CA), such as HSAG, carbon black and MWCNTs, are highly hydrophobic materials, hence, achieving a homogenous dispersion in watery solvents avoiding aggregation and precipitation is a challenging issue. For this reason, functionalization represents indeed a widely-used procedure to overcome these problems and to tune solubility parameters of CA, extending their potential fields of applicability [26].

One of the aims of our work was the functionalization of CA with a simple, sustainable, green and cheap process for a large scale production. Moreover, in order to enhance the antibacterial properties of these materials functionalization could be used to enrich CA with Ag NPs [60].

A *Janus* molecule, 2-(2,5-dimethyl-1*H*-pyrrol-1yl)-1,3-propanediol (serinol pyrrole, SP) was chosen as the organic compound able to react with sp^2 CA, improving their solubility parameters [72]. In addition, the presence of SP in the functionalized sp^2 CA is a key factor to sussessfully carry out the further functionalization step with Ag NPs, serving as binding site.

SP is a five-membered heterocyclic aromatic molecule belonging to the family of pyrrole compounds. The synthesis of SP is a sustainable process that has been recently patented by the research group of Professor Galimberti (ISMaterials) at Politecnico di Milano [73].

The synthesis of SP was performed through the Paal-Knorr reaction between the primary amine 2-amino-1,3-propanediol (serinol, S) and 2,5-hexanedione (HD). It is worth mentioning that the synthesis of SP occurred in the absence of solvent and catalysts, with water as the only by-product, as showed in Figure 3.1 [75].

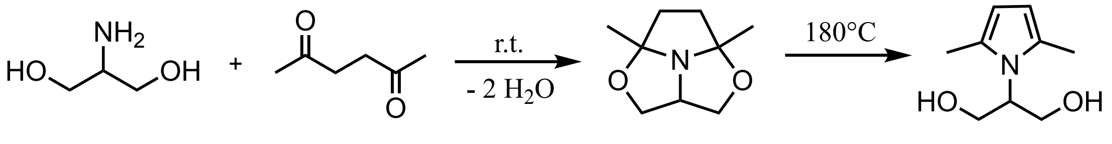

S HD HHP SP

Figure 3.1 - Reaction pathway for the synthesis of SP [75].

In our case, as reported in detail in the experimental chapter 2.2.1 – Synthesis of serinol pyrrole (SP), the reaction between S and HD was carried out at 155°C for 3 hours. The reaction mixture was monitored by means of GC-MS (Gas Chromatography - Mass Spectroscopy apparatus, Agilent 5973 Inert GC-MS System, Agilent Technologies). The GC-MS chromatograph showed an intense peak corresponding to the formation of SP (MW = 169 g/mol). However, the tricyclic intermediate (2a,4a-dimethylhexahydro-1*H*-2,5-dioxa-2a^1-azacyclopenta[*cd*]pentalene, HHP), showed in Figure 3.1, had the same molecular weight of SP. This intermediate is an isomer of SP and it was recognized from its higher hydrophobicity: the lack of hydroxyl groups leads to a lower affinity with the hydrophilic stationary phase of the chromatographic column, hence its elution was anticipated compared to that of SP (HHP exits the column at 12 minutes, SP at 17 minutes). In our case, the SP reaction yield was up to 95%.

A further NMR analysis was carried out by the research group of Professor Galimberti (ISMaterials) to validate the synthesis: chemical shifts in the NMR spectra confirmed that the production of SP was successfully achieved.

The reaction product SP appeared as a highly viscous liquid of brown color, difficult to handle for routine measurements at room temperature. Thus, a preliminary warming phase (100°C, 20 minutes) was needed prior to its manipulation (Figure 3.2).

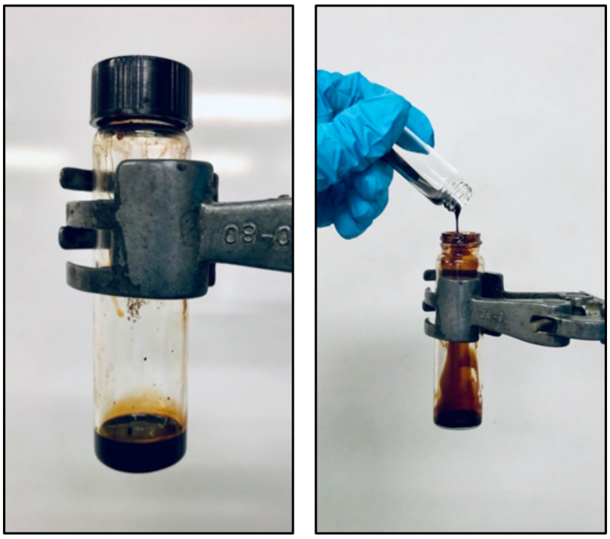

Figure 3.2 - SP physical appearance after heating it up to 120°C (on the left) and after few minutes of cooling down at R.T. (on the right).

3.1.2 Evaluation of the functionalization procedure

The functionalization of sp^2 CA with SP and Ag NPs was carried out through a sustainable and cheap method without using metallic catalysts. The absence of these catalysts is important to avoid unmeasurable influences on the antibacterial activity of the final products: purification procedures can not assure the complete elimination of metallic contaminants from samples and the presence of these residuals could interfere with the evaluation of antimicrobial properties of CA powders functionalized with Ag, due to the fact that metallic impurities could have an intrinsic antibacterial activity.

The whole preparation process of CA-SP-Ag derivatives has also the advantage to be easily scalable, paving the way for the implementation of large-scale production chains.

The reaction mechanism elaborated by Barbera et al. [26] describes a cascade reaction composed of two steps: a first carbocatalyzed oxidation followed by a Diels-Alder reaction (Figure 3.3).

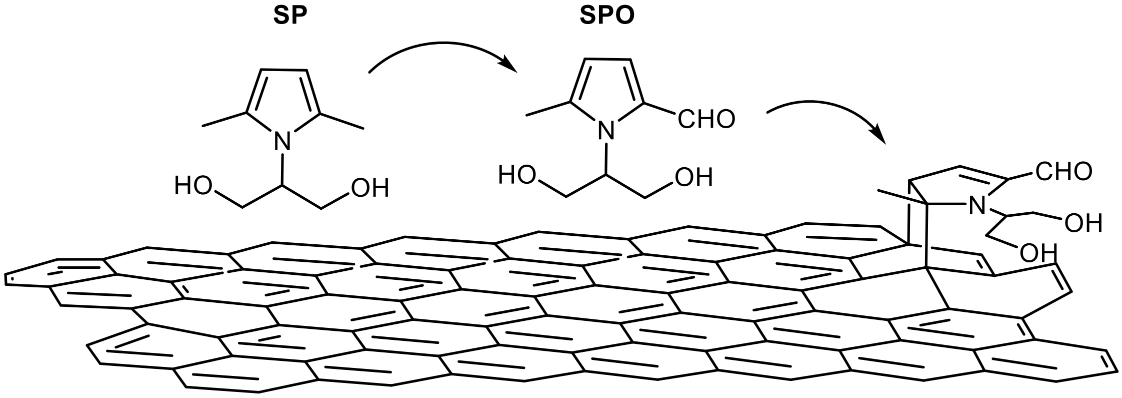

Figure 3.3 - Hypothesized mechanism for the decoration of graphene layers with SP. A preliminary oxidation of SP catalyzed by the carbon skeleton (from SP to SPO) is followed by a cycloaddition reaction between SPO and the carbon structure.

The first step of the reaction is assumed to be the carbocatalyzed oxidation of SP, which leads to an oxidized SP derivative (IUPAC: 1-(1,3-dihydroxypropan-2-yl)-5-methyl-1*H*-pyrrole-2-carbaldehyde; SPO). It was hypothesized that the graphitic substrate promotes the oxidation of SP, which does not occur in the absence of sp^2 carbon allotrope, and stabilizes the pyrrole ring, which maintains its aromatic nature. The second step of the reaction is assumed to be the cycloaddition reaction (a Diels-Alder reaction). The Diels-Alder reaction occurs between the double bond of the pyrrole ring, activated by oxidized lateral substituent (aldehydic group) and the graphitic substrate. The activated pyrrole molecule would act as the dienophile and the graphene layer as the diene.

In this work, CA were functionalized first with SP and then with Ag NPs. Hence, CA-SP-Ag adducts were efficiently prepared through a two-step procedure:

- functionalization of CA with SP, forming CA-SP derivatives;
- functionalization of CA-SP derivatives with Ag NPs, forming CA-SP-Ag derivatives.

CA were functionalized with SP aiming to obtain a 10% (w/w) functionalization ratio between SP oxygenated moieties and the final powders. This 10% (w/w) ratio was previously used and experimented by Professor Galimberti's research group (ISMaterials), hence, the precise amounts of materials to achieve this functionalization ratio were kindly provided to us.

Briefly, CA and SP were bath sonicated in acetone for 20 minutes, the solvent was further eliminated and the dried sample was ramp heated up to 180°C under magnetic stirring for 2 hours. The sample was then dissolved again in acetone and left under stirring at room temperature for 18 hours. It was finally recovered through vacuum filtration and dried.

A preliminary result to state the efficacy of the functionalization procedure was given by the appearance of the filtrate at the end of this first functionalization step: the more the turbidity of the filtrate, the less the functionalization effectiveness. Our filtrates appeared very clear and slightly yellow-colored, indicating that the majority of SP was presumably grafted on the allotropes and that functionalization of CA occurred properly (Figure 3.4).

Figure 3.4 - Picture of the filtrate at the end of the first functionalization step. CA: Graphite.

Regarding the second functionalization step, that is the preparation of CA-SP-Ag derivatives, a huge amount of literature reports different methods for functionalization of carbon-related materials with Ag NPs. These methods mainly rely on surface functionalization of carbon-related materials through different physico/chemical reduction processes of Ag^+ ions by means of L-Arginine [76], hydrazine [27], $Na_3C_6H_5O_7$ [63], $NaBH_4$ [61], glucose and UV irradiation [25] or heating at 200°C [60].

In our thesis work, the functionalization of CA with Ag NPs was carried out through a simple mechanism of deposition of metallic Ag using Tollens' reagent. The Tollens' assay is a common and simple test to detect the presence of aldehydes in a sample. Chemical reactions involved in this test were described in detail by Benet et al. [77]. Briefly, the redox reaction caused by the interaction between Tollens' reactive and aldehydes leads to massive precipitation of metallic Ag (Figure 3.5), leaving the characteristic silver mirror on the test tube walls (Figure 3.6).

$$3OH^- + 2Ag(NH_3)_2 + RCHO \longrightarrow 2Ag + 4NH_3 + RCOO^- + H_2O$$

$$\text{Tollens reactive + aldehyde} \longrightarrow \text{Silver precipitate}$$

Figure 3.5 – Tollens' reaction: silver precipitation (Ag) in presence of aldehydes (RCHO). The reaction is favored in a basic environment (plenty of OH^-), thus, NaOH behave as a reaction enhancer.

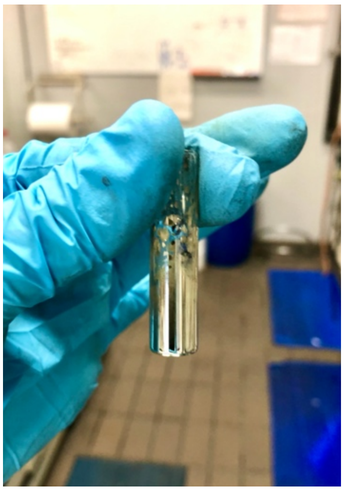

Figure 3.6 - Appearance of the characteristic silver mirror on test tube walls: this effect was the result of the reaction between few drops of Tollens' reactive and glucose (i.e. an aldehyde). This phenomenon validates Tollens' reactive functionality.

At the beginning of this investigation, Tollens' reagent was selected to underline the presence of aldehydes, thus the covalent bonded SP on the CA surface. Nevertheless, after mixing CA-SP with Tollens' reagent, Ag was discovered to deposit on sp^2 CA rather than on glass walls [V.Barbera, M. Galimberti et al. – Unpublished results]. The hypothesized mechanism for the decoration of graphene layers with Ag NPs is reported in Figure 3.7.

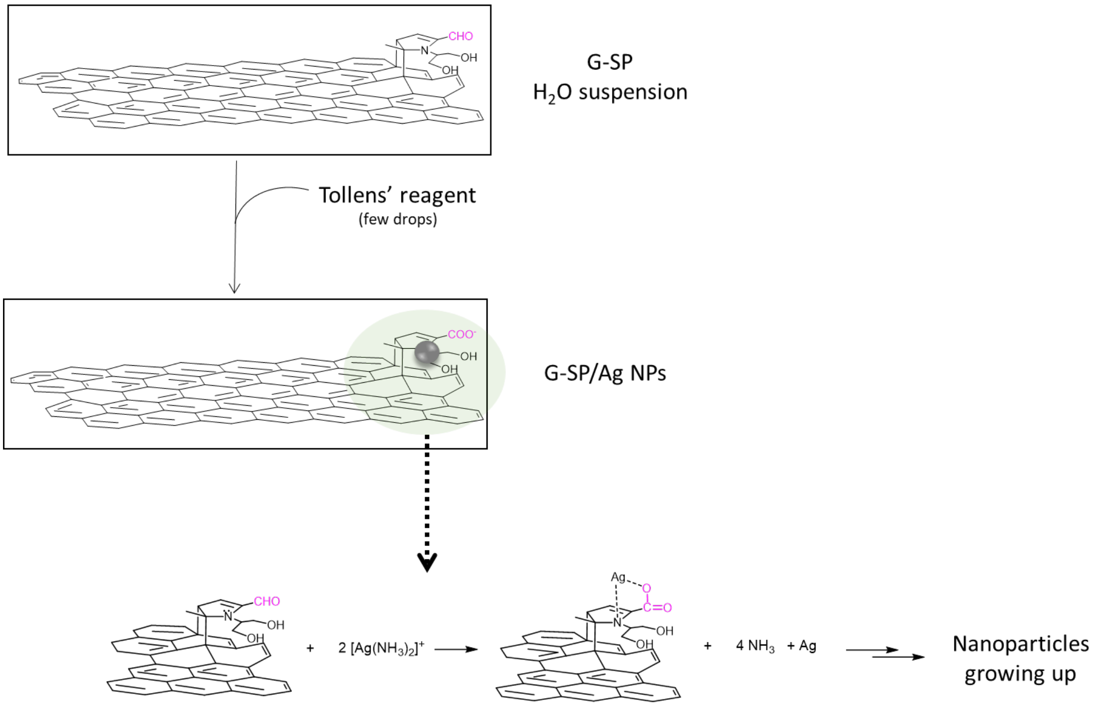

Figure 3.7 - Hypothesized mechanism for the decoration of graphene layers with Ag NPs.

In the case of our CA-SP derivatives, Tollens' reactive is able to interact with the aldehyde group of oxidized SP grafted on the graphitic structure. This could determine the precipitation of Ag and its bonding with the oxidized SP molecules. The mechanism involves electron pairs of nitrogen atoms (N) of SP as potential linkers between metallic Ag and the graphitic structure.

CA functionalization with Ag did not cause macroscopic alterations of powders' color or density in CA-SP-Ag products, which were dried and eventually collected in separate glass tubes (Figure 3.8).

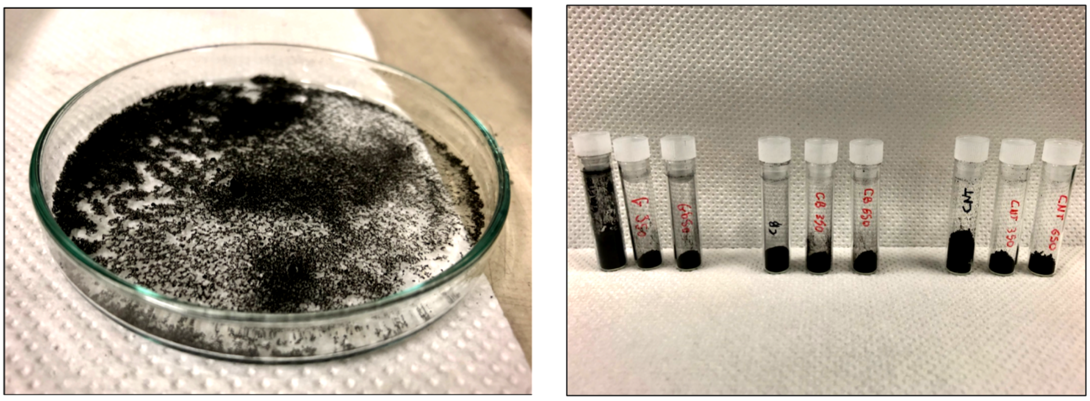

Figure 3.8 - Dried sample in a crystallizing dish (CNT650 sample) on the left and functionalized samples collected in glass tubes on the right.

3.2 Characterization of Graphene-based nanomaterials

This chapter will focus on the physico/chemical characterization of graphene-based nanomaterials, providing a detailed insight about their composition, nanometric structures and chemico/physical features of their colloidal suspensions.

3.2.1 Analysis of Graphene-based nanomaterials composition

Thermogravimetric analysis (TGA) provided information regarding the composition of CA-SP-Ag derivatives in terms of weight percentages [78].
TGA was performed on each sample, hence, all of them were paired with a specific TGA graph indicating their composition. For the sake of simplicity, we will report only the graph of sample G650 (Figure 3.9), referring the reader to the appendix (Appendix 5.1 – TGA graphs) for a broader outlook on the other samples.

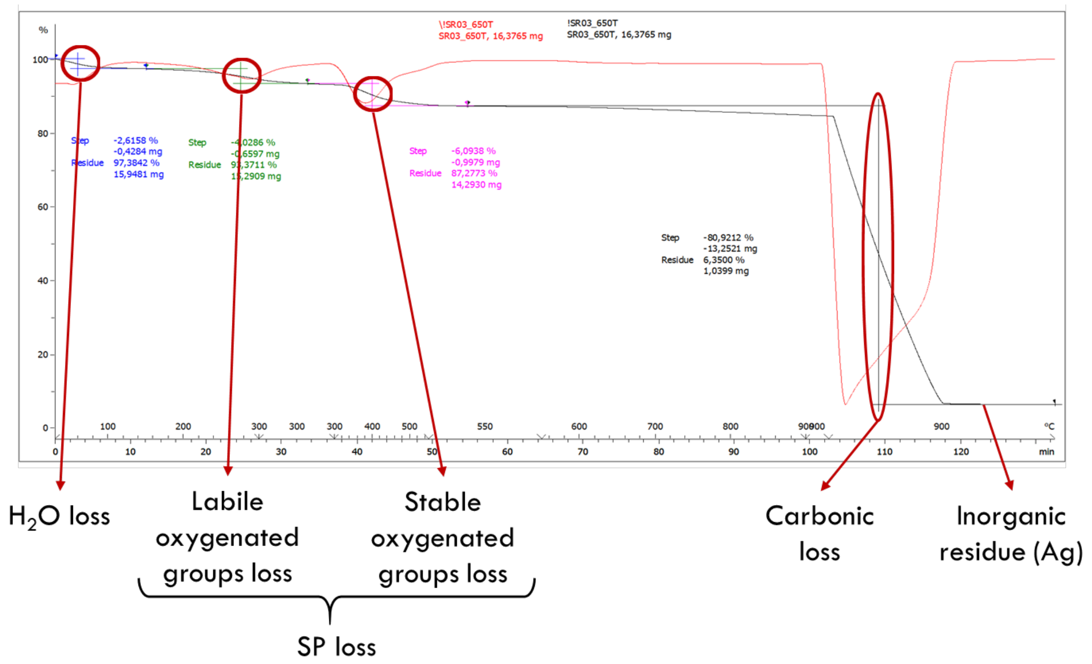

Figure 3.9 - Example of a TGA output for sample G650. From left to right, steps represent weight losses of water (blue), labile oxygenated group (green), stable oxygenated group (pink) and carbonic part (black ramp after switching from N_2 to O_2 flux). The residue represents the inorganic part, predominantly Ag in our case. Red lines represent the first derivative of the black curve and its peaks indicate the points of greatest rate o change on the weight loss curve.

The graph precisely points out four distinct regions, each one associated to the loss of a specific fraction of the sample. The region between 0°C and 100°C refers to the loss of adsorbed water. Between 150°C and 300°C, weight loss is caused by the decomposition of labile oxygenated groups (e.g. hydroxyl or epoxy groups), while between 300°C and 500°C the loss is associated to the removal of more stable oxygenated groups (e.g. carbonyl or carboxyl groups) [79], [80]. We hypothesized these two regions belonged to the removal of SP: this molecule show indeed both hydroxyl and carbonyl moieties. Therefore, the sum of these losses was attributed to the loss of oxygenated groups of SP molecules and, for the sake of simplicity, this weight fraction was considered as the total SP loss.
Above 500°C, the influx of O_2 for 20 minutes promoted the pyrolysis of the carbon skeleton at 900°C, leaving a residue related with the inorganic part, presumably Ag in our case.

Data from TGA were converted from SP, carbonic and Ag masses to their corresponding moles (Table 3.1).

Table 3.1 - Automated tool for the computation of SP, C=C and Ag moles per 100 mg of sample. Sample: G650, the table is associated to values from the image of the TGA graph above.

GRAPHITE 650

H_2O loss [%]	2.6
Labile oxygenated groups loss [%]	4.0
Stable oxygenated group loss [%]	6.1
Carbonic loss [%]	80.9
Inorganic residue [%]	6.4
TOTAL	100.0

MW [mg/mmol]

SP	183
Ag	108
C=C	24

RESULTS

Compound	Composition [%]	Concentration [mmol/100 mg]
SP	10.12	0.0553
Ag	6.35	0.0588
C=C	80.92	3.3713

The conversion of the carbonic loss from mass to moles proved to be a challenging issue: the graphene layer is a latticework composed by an undefined number of hexagonal carbon rings, thus the computation of its molar counterpart needs the identification of a representative chemical unit which is repeated through its structure. Usually, this chemical unit is represented by the 6 carbon atoms aromatic ring, hence, its molecular weight (MW = 72.06 g/mol) is used to obtain the number of moles for the carbonic part [26]. However, this choice presents a huge drawback: it does not depict the optimal chemical unit to model the graphene structure since adjacent hexagonal rings share carbon atoms, hence, this kind of modelling necessarily generates an overestimation in the number of repetitive units.

For this reason, we decided to use a 2 carbon atoms unit (C=C) as representative chemical unit: in our model the graphene layer is not seen as a lattice of hexagonal aromatic rings but as a series of several 2 double-bondend carbon atoms, in which repetitive units share no atoms among them. By this assumption, no overestimation in the number of chemical units occurs. Thus the molecular weight of the C=C repetitive unit (MW = 24.02 g/mol) was used to more precisely compute the carbonic molar fraction.

The informations regarding molar fractions of each component per 100 mg of powder of each sample were listed and re-elaborated to obtain desired ratios between components (Table 3.2). These results will be used to estimate the amount of each desired element during the preparation of CA-SP-Ag suspensions during antimicrobial screening tests.

Table 3.2 - Automated table for the calculation of molar ratios and weight fractions between components of each sample.

	GRAPHITE			**CARBON BLACK**			**MULTIWALL CARBON NANOTUBES**		
	G	**G350**	**G650**	**CB**	**CB350**	**CB650**	**CNT**	**CNT350**	**CNT650**
C=C Moles [mmol/100mg]	3.65	3.44	3.37	3.70	3.02	2.46	3.96	2.87	2.91
SP Moles [µmol/100mg]	63.30	58.30	55.30	54.60	56.20	56.90	19.80	69.80	56.60
Ag Moles [µmol/100mg]	-	42.50	58.80	-	150.60	252.60	-	159.10	160.70
SP Moles : C=C Moles [µmol/µmol]	0.017	0.017	0.016	0.015	0.019	0.023	0.005	0.024	0.019
Ag Moles : C=C Moles [µmol/µmol]	-	0.012	0.017	-	0.050	0.103	-	0.055	0.055
SP Functionalization Rate [% (w/w)]	11.6	10.7	10.1	10.0	10.3	10.4	3.6	12.8	10.4
Ag Functionalization Rate [% (w/w)]	-	4.6	6.4	-	16.3	27.3	-	17.2	17.4

Results suggested that a proper 10% (w/w) functionalization rate between SP oxygenated moieties and CA occurred, except for the sample CNT, where this functionalization rate was of 3.6%. This difference may be caused by systematic errors during TGA analysis. This hypothesis was validated by the fact that samples CNT350 and CNT650 showed a proper 10% functionalization rate between SP oxygenated groups and CA. In fact, these samples were derived from CNT sample and should display similar functionalization rates.

The rate of the functionalization of CA-SP derivatives with Ag was different among samples of the same type of allotrope and among samples of different allotropes: higher amounts of Tollens' reactive (i.e. '350 samples vs. '650 samples) effectively elicited higher Ag-functionalization rate (apart from MWCNT samples). Besides, remarkable differences between CA suggested an allotrope-dependent Ag-functionalization behavior. CB samples displayed the maximal Ag-functionalization rate while Graphite ones the lowest (almost 4-times lower). These results were corroborated by TEM micrographs in the following chapter with a qualitative analysis.

We speculated that the discrepancy between Ag-functionalization rate of Graphite and those of CB and MWCNTs was attributable to the higher availability of SP moieties exposed on the surface of both CB and MWCNTs samples. On the other hand, the stacked architecture of Graphite presumably prevents Ag deposition between layers, favoring only edging positions or self aggregation between metallic Ag NPs. For similar reasons, we thought that CNT650 sample did not beneficiate of the higher amount of Tollens' reactive: the saturation of all accessible oxygenated moieties could be responsible for this phenomenon.

3.2.2 Structural and dimensional analyses

Structures of sp^2 CA were studied by means of High Resolution Transmission Electron Microscopy (HRTEM) and Wide Angle X-ray Diffraction (WAXD). A morphological investigation of G650, CB650 and CNT650 was performed by means of HRTEM analyses. Simultaneously, the efficiency of CA functionalization with Ag nanoparticles (AgNPs) was also evaluated.

Results confirmed the expected structures and relative characteristic dimensions for each carbon allotrope, such as acinus size for Carbon Black and nanotubes diameter for MWCNTs: results were found to be in accordance with scientific literature [32], [45], [81] and the specifics provided by manufacturers.

Each sample was characterized by different structures at different scale levels. HRTEM micrographs confirmed the presence of clusters of microscopic dimensions and a qualitative analysis of micrographs suggested that microscopical particles are the result of aggregation due to the high hydrophobic behavior of carbon related materials, which tend to agglomerate if not dispersed in proper solvents. In addition, aggregation was visibly enhanced for MWCNTs because of their tendency to entangle. Exact dimensions of such agglomerates were difficult to confirm through HRTEM micrographs due to the partial superimposition between them, caused by sample dehydration and resultant precipitation on the copper grid. Despite this, a dimensional analysis on each allotrope was performed using ImageJ in order to estimate sizes of isolated particles through the calculation of the Feret's diameter.

ImageJ analysis was performed on aggregates of the sample G650 revealing a mean size of 1,05 ± 0,55 µm, although two different dimensional distributions were visible: one composed by smaller aggregates with sizes ranging between 0,30 - 0,54 µm and another one by massive clusters of graphite particles of approximately 1,57 - 1,93 µm. Similar observations could be done for CB650 micrographs in which, against a mean diameter of 1,30 ± 0,68 µm, small aggregates of 0,30 - 0,63 µm and large clusters of 2,11 - 2,37 µm were simultaneously detectable (Figure 3.11 B). These findings are in accordance with DLS results. Large entangles were clearly identifiable for CNT650 sample. A dimensional quantification of aggregates was impossible to perform due to the lack of images at lower magnification (Figure 3.12 B). Moreover, entangles of CNTs are difficult to approximate to a spherical geometry, hence, we believe the Feret's diameter could not be the proper parameter for size evaluation. For these reasons, even if the nanotubes aggregation was macroscopically and microscopically visible, a dimensional characterization of macroscopic entangles will not be provided in this work.

As mentioned herein above, HRTEM images were used also to evaluate the quality of Ag enrichment of samples. Ag NPs appeared as black spherical particles due to their higher electronical density compared to graphene allotropes, thus their presence was easily confirmed by high magnification micrographs.
A dimensional analysis for Ag NPs revealed a high number population of nanometric particles ranging from 3 – 7 nm for each sample (Figure 3.10 images C, D; figure 3.11 images C, D; figure 3.12 images C, D) in accordance with scientific articles dealing with functionalization of carbon related materials by means of Ag [25], [27], [61], [62]. However, few larger agglomerates of approximately 100 – 200 nm diameter were clearly visible in the case of G650 (Figure 3.10 B, C, D). Relying on these findings, for Ag-functionalized Graphite samples, it seems that Ag NPs were more likely to form large aggregates rather than grafting on graphite structures. To overcome this issue, we suggest that longer ultrasonication times during the Ag-functionalization phase could potentially solve the problem, inhibiting self-aggregation of small Ag NPs.

The structure of the pristine allotropes at nanometric scale was also analyzed. Graphene flakes were clearly visible for G650 sample: 4 – 23 nm thick stacked structures could be observed (Figure 3.10 B). Assuming a theoretical 0.34 nm distance between each graphene layer [45], it is possible to infer that the number of graphene layers composing our graphite samples approximately ranges from 10 to 70. This theoretical distance of 0.34 nm was almost identical to the experimental 0.32 nm interplanar spacing resulted from the software analysis carried out through the software Gatan Microscopy Suite. These findings led to hypothesize that the original interplanar spacing was not altered after the functionalization process, thus oxygenation of graphite samples occurred predominantly on the edges. These results differ from other scientific works, which clearly reported the successful interplanar functionalization of graphene layers with oxygenated groups [62].

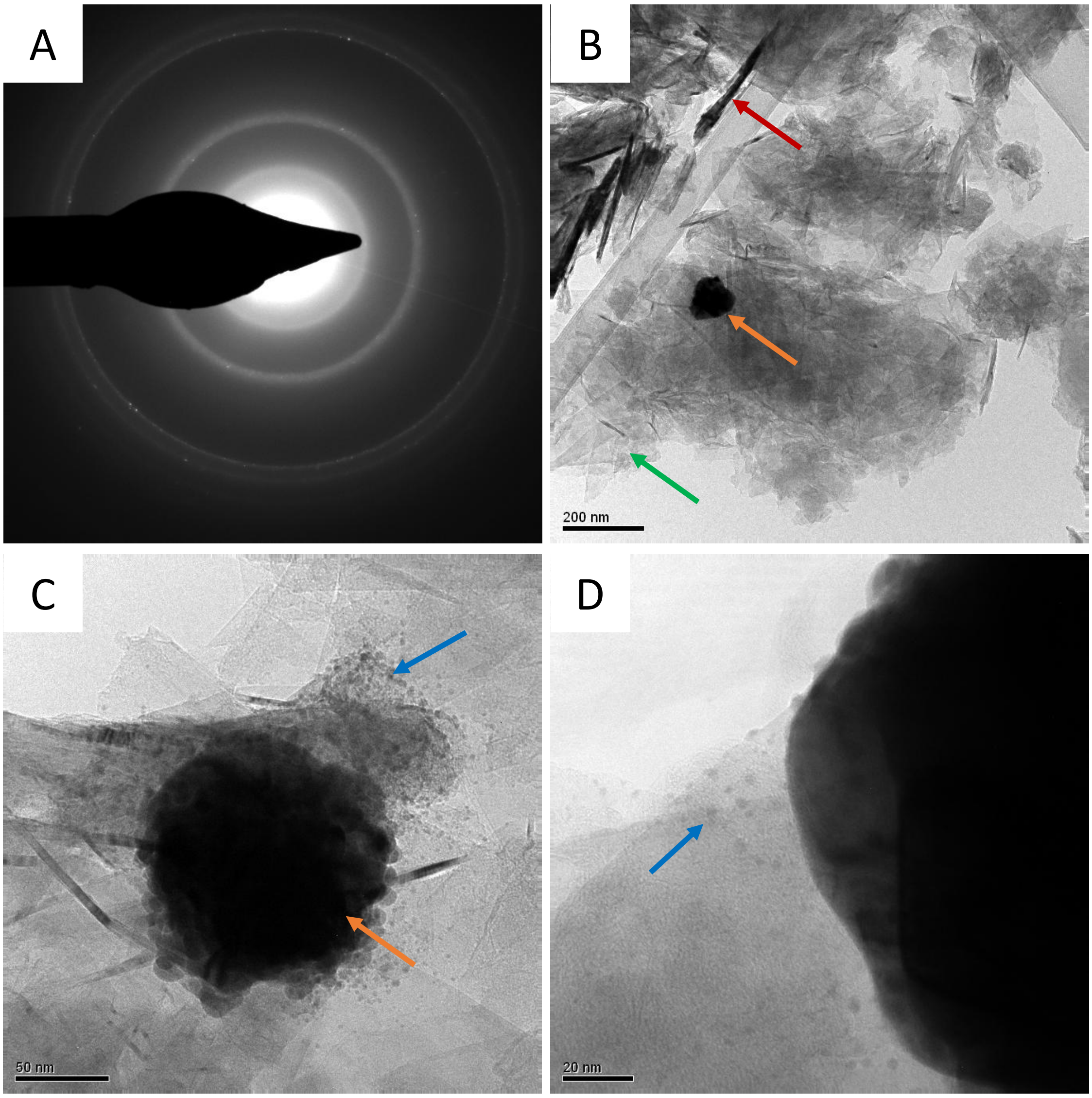

Figure 3.10 - HRTEM micrographs for the sample G650. (A) Diffraction pattern. (B) Scalebar: 200 nm. Red arrow evidences one of graphite stacked structure, i.e. several graphene layers parallelly stacked onto each other; green arrow indicates graphene flakes; orange arrow points out a large aggregate of Ag NPs also visible in micrographs (C) and (D). (C), (D) Scalebar: 50 nm and 20 nm respectively - where small spherical Ag NPs are evidenced by blue arrows.

Regarding CB650 sample, a first insight at lower magnifications allowed to detect microscopical agglomerates (Figure 3.11 B). Peculiar spherical structures of CB were observed at higher magnifications (Figure 3.11 C, D), resulting in 42 ± 6 nm diameter acini, in accordance with literature and specifics provided by manufacturers. The interplanar spacing calculated from image processing was of 0.52 nm: the discrepancy between this value and the theoretical one could be due to the turbostratic deposition of graphene layers, resulting in a mesomorphic structure and irregular clustering which could have altered the characteristic interplanar spacing of 0.34 nm [53].

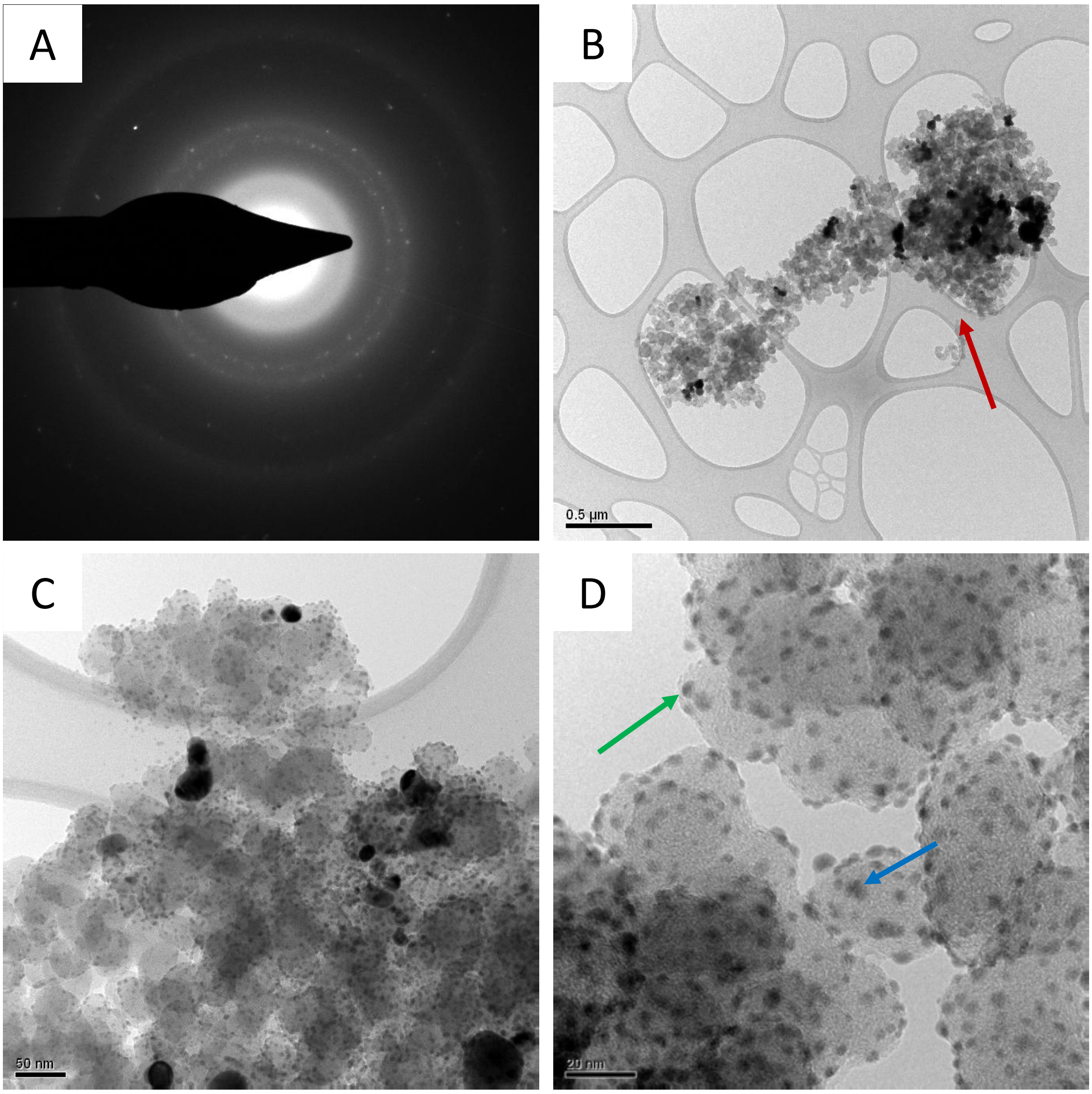

Figure 3.11 - HRTEM micrograph for sample CB650. (A) Diffraction pattern. (B) Scalebar: 500 nm. Carbon Black tend to aggregate forming micro agglomerates (red arrow). (C), (D) – Scalebar: 50 nm and 20 nm respectively – Carbon Black spherical structures are clearly visible (green arrow) together with an excellent decoration provided by Ag NPs (blue arrow).

CNT650 sample was characterized by nanotubes peculiar bundles of filaments (Figure 3.12 B). The diameter of a single nanotube ranged from 5 to 9 nm (Figure 3.12 C), with a mean value of 7 ± 1 nm, in accordance with specifics provided by manufacturer. Interplanar spacing between concentric walls resulted to be 0.34 nm. This value is in accordance with scientific literature [32].

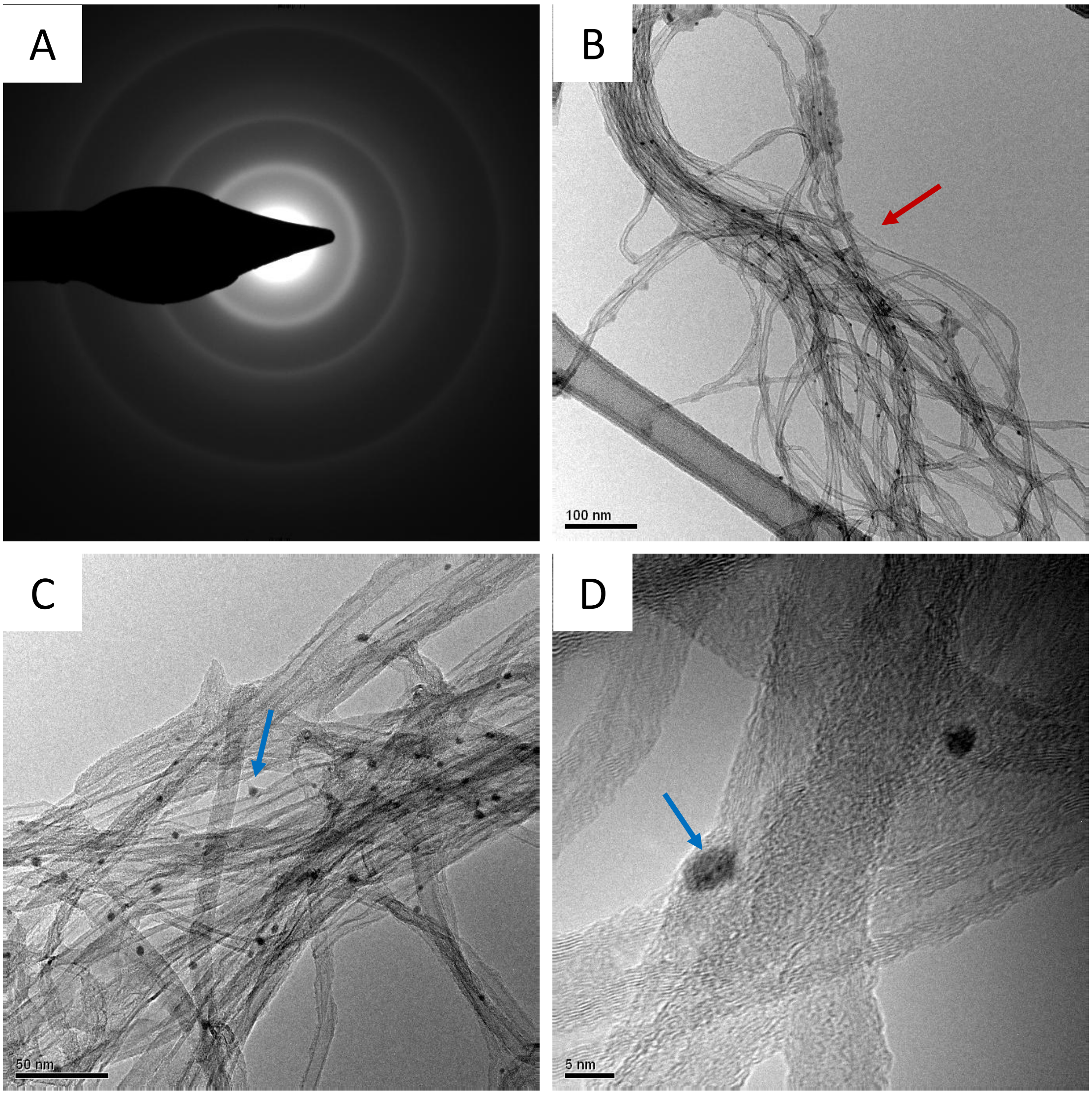

Figure 3.12 - HRTEM micrograph for sample CNT650. (A) Diffraction pattern. (B) Scalebar: 100 nm. Carbon nanotubes characteristic bundles of filaments are visible (red arrow). (C), (D) – Scalebar: 50 nm and 5 nm respectively – Ag NPs are linked to CNT in this case too. Their dimension is easily obtainable from micrograph (D)

Structures of pristine sp^2 CA (Graphite Nano 307 (HSAG), MWCNTs NC7000 and CB N326), CA functionalized with SP (CA-SP: G, CB, CNT samples), CA-SP-Ag 350 (G350, CNT350, CB350 samples) and CA-SP-Ag 650 (G650, CNT650, CB650 samples) derivatives were then analyzed by means of Wide-angle X-Ray diffraction analysis (WAXD).

Figure 3.13 shows WAXD patterns taken on powders of pristine CA, CA-SP, CA-SP-Ag 350 and CA-SP-Ag 650 derivatives.

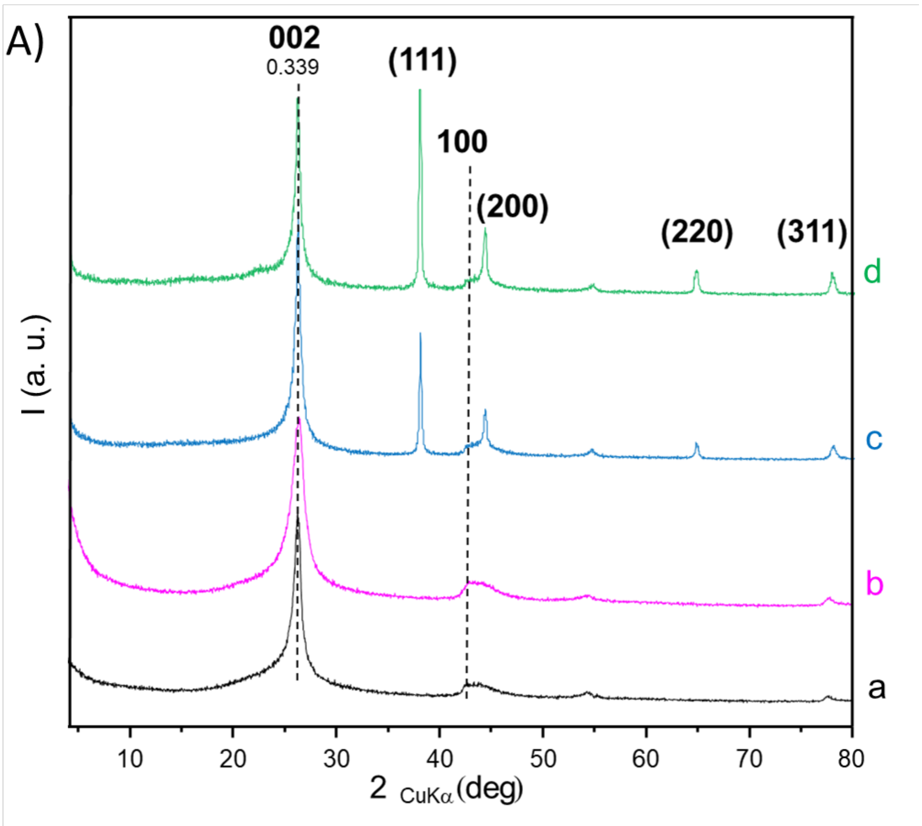

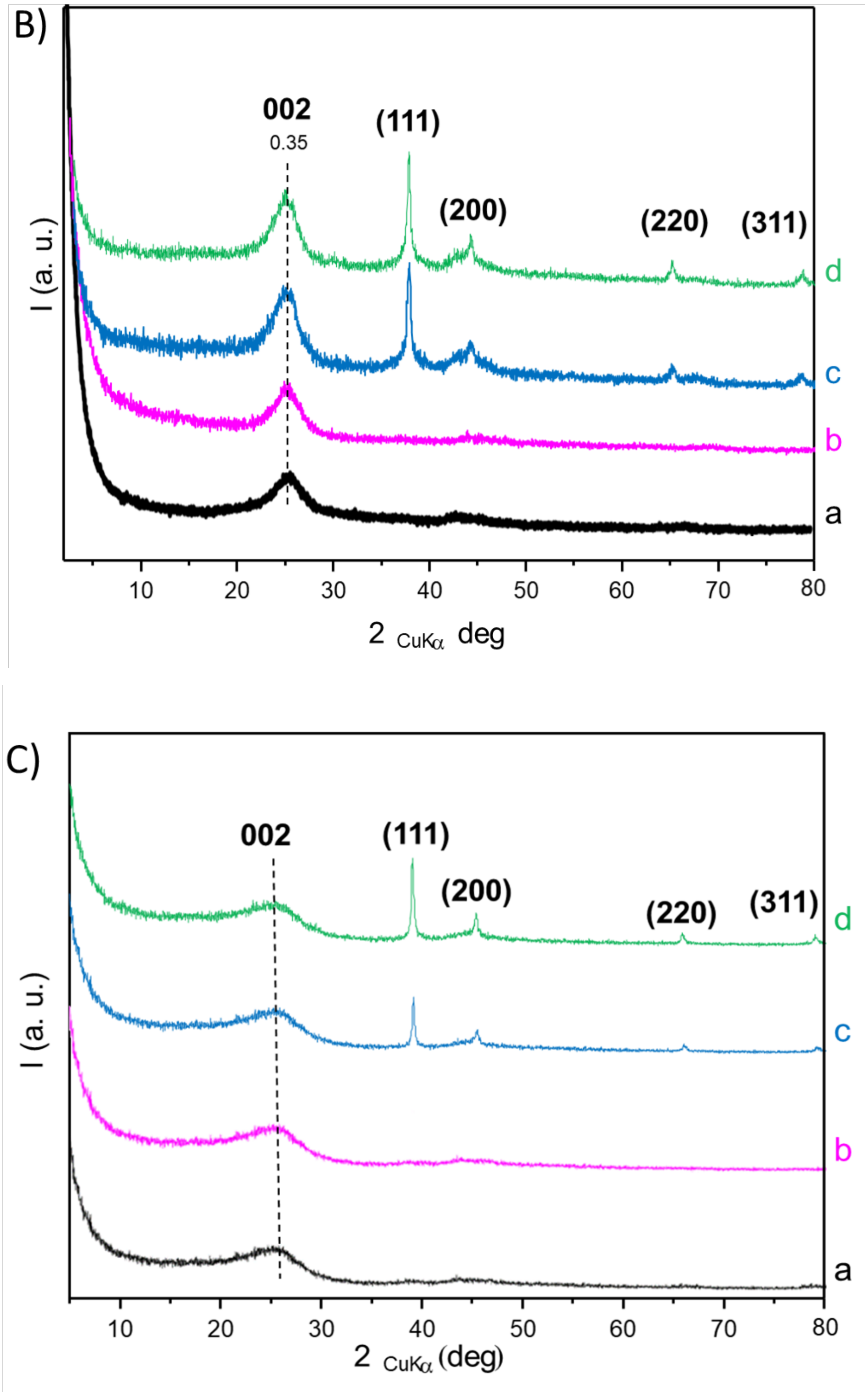

Figure 3.13 - WAXD patterns of (A) graphite samples: Graphite Nano 307 (HSAG)(a), G (b), G350 (c) and G650 (d); (B) carbon nanotubes samples: MWCNT NC7000 (a), CNT (b), CNT350 (c) and CNT650 (d); (C) carbon black samples: CB N326 (a), CB (b), CB350 (c) and CB650 (d).

In pristine HSAG, MWCNT and CB, crystalline order in the direction orthogonal to structural layers is revealed by (002) reflection at 26.6°, which corresponds to an interlayer distance, obtained from the Bragg's law (chapter 2.3.3 – Wide angle X-ray diffraction anlysis (WAXD)), of 0.338 and 0.350 nm for HSAG and MWCNT respectively, confirming values obtained from HRTEM analyses of G650 and CNT650 samples. These interlayer distances are slightly larger than the one of ordered graphite samples (d_{002} = 0.335 nm). The in-plane order is shown by 100 and 110 reflections, at 42.5° and 77.6° respectively. In the graphitic samples, by applying the Scherrer equation to (002) and (110) reflections, respectively, the out-of-plane ($D_{\perp}$) and the in-plane ($D_{\parallel}$) correlation lengths were calculated. Values were 9.8 nm for ($D_{\perp}$) and 30.2 nm for ($D_{\parallel}$). The in-plane correlation length is thus larger than the out-of-plane correlation length. From the values of ($D_{\perp}$) and of the interlayer distance, the number of stacked layers was estimated to be about 35 for Graphite Nano 307 (HSAG) and 12 for MWCNT NC7000. These results reveal the turbostratic nature of HSAG [75] that has however remarkable crystalline order inside the structural layers. (002) reflection in the patterns of the sp^2 derivatives samples remains at the same 2θ value, indicating that the formation of the derivatives did not promote expansion of the interlayer distance.

The number of stacked layers in G and CNT samples was calculated by applying the Scherrer equation to 002 reflection. From the calculation G, G350 and G650 samples show 21, 19 and 19 stacked layers respectively. CNT, CNT350 and CNT-650 show the same number of stacked crystalline layers of their pristine counterpart (12).

Patterns of carbon black samples present broad 002 reflections. The out-of-plane correlation lengths ($D_{\perp}$) were estimated, by applying the Scherrer equation, to be about 1.9 nm which corresponds to a number of layers stacked in crystalline domain of about 5. Low intensity can be observed for the broad reflections characteristics of the order inside the graphitic planes. In all samples, 101 and 112 reflections are negligible. The absence of (hkℓ) reflections with $\ell \neq 0$, other than (002), is a clear indication of the structural disorder of starting CB.

Figures 3.13Ac, 3.13Ad, 3.13Bc, 3.13Bd, 3.13Cc and 3.13Cd report the XRD patterns of G350, G650, CNT350, CNT650, CB350 and CB650 samples. All patterns reported shows the diffraction peaks at 38.24°, 44.27°, 64.59° and 77.50° corresponding to the (111), (200), (220) and (311) facets of the Ag NP deposited on CA.

3.2.3 Stability of suspensions and kinetics of precipitation

The assessment of the stability of CA-Ag suspensions was carried out by analyzing UV-Vis absorption spectra of the pristine starting materials, i.e. G, CB and CNT. We speculated that the precipitation kinetics of pristine CA and their Ag-functionalized counterparts could not exhibit strongly different behaviors. Indeed, the enrichment with Ag did not cause a dramatic change in graphene allotropes solubility, shape and/or mass. Hence, the stability of the suspensions should follow the same trend over time.

To evaluate the precipitation phenomena, we have chosen to quantify samples concentration of supernatant over time by means of UV-Vis spectrophotometric analyses. Thereby it was possible to provide a precise quantification of the carbon-related material dispersed inside PBS, i.e. able to elicit an antimicrobial effect. The principal aim of this analysis was to evaluate whether ultrasonication provided a beneficial effect in terms of suspension stability, thus comparisons between sonicated and not-sonicated samples will be provided.

Firstly, a calibration curve was obtained: using the Lambert-Beer law it is possible to evaluate the analyte concentration (C) knowing the sample absorbance at a specific wavelength (A). It is important to mention that the Lambert-Beer law is reliable only in a specific linear working range of concentration, which may differ between different samples. Thus, its individuation is of primary importance for further computations.

Each ultrasonicated starting material was diluted in PBS at different concentrations (1 mg/mL, 0.5 mg/mL, 0.1 mg/mL, 0.05 mg/mL, 0.01 mg/mL, 0.005 mg/mL and 0.001 mg/mL) and analyzed. Absorbance values at 300 nm were recorded and displayed as a function of concentration [mg/mL] as reported in Figure 3.14, where the linear region for each sample is clearly visible for concentrations ranging from 0 mg/mL to 0.1 mg/mL.

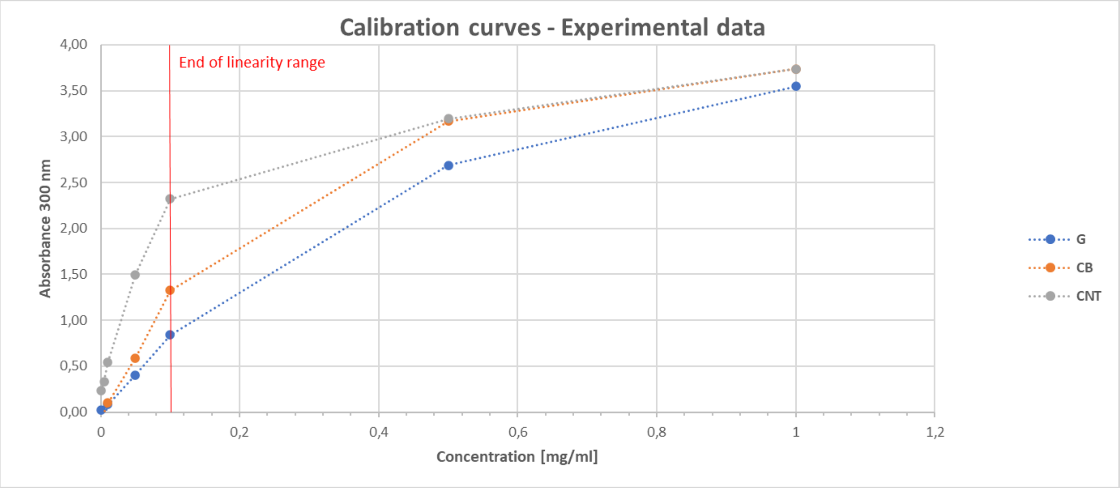

Figure 3.14 - Experimental data from UV-Vis spectrophotometric analysis for G, CB and CNT samples diluted in PBS at known concentrations. The linear range is clearly visible for each allotrope below the concentration of 0.1 mg/mL (left of the red vertical line).

The following calibration curves (Figure 3.15) were obtained from starting materials and will be useful for both functionalized and not-functionalized G, CB, and CNT samples. In addition, for each curve, relative equations and R^2 parameters are provided. The computed angular coefficient (m) is equal to the term $(\varepsilon \cdot b)$ of the Lambert-Beer law, thus higher values of m will relate with higher values of ε while keeping unaltered the optical path length b.

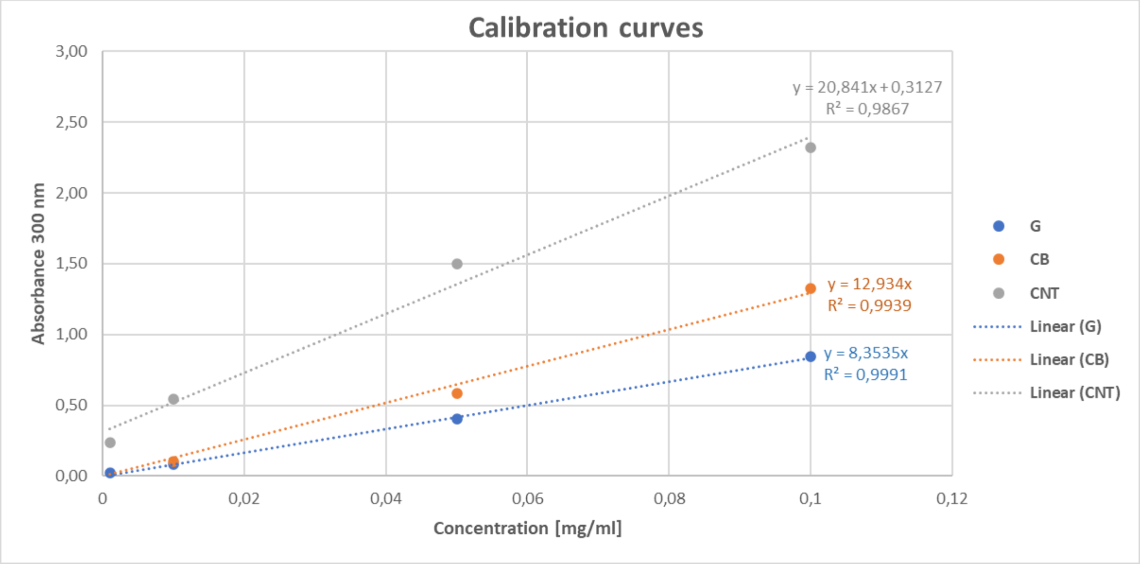

Figure 3.15 - Calibration curves for G (blue), CB (orange) and CNT (grey) samples evaluated in the linear range below 0.1 mg/mL. For each curve, equations and R² parameters are provided.

Different precipitation profiles among the three allotropes were clearly identified and variations introduced by the ultrasonication procedure were observed (Figure 3.16) and quantified by means of the Precipitated Mass Fraction parameter as described in chapter 2.3.4 – UV-vis spectroscopy (Table 3.4). This parameter quantifies in percentage the fraction of the total mass of dispersed material which has precipitated at a certain time after the preparation of the suspension.

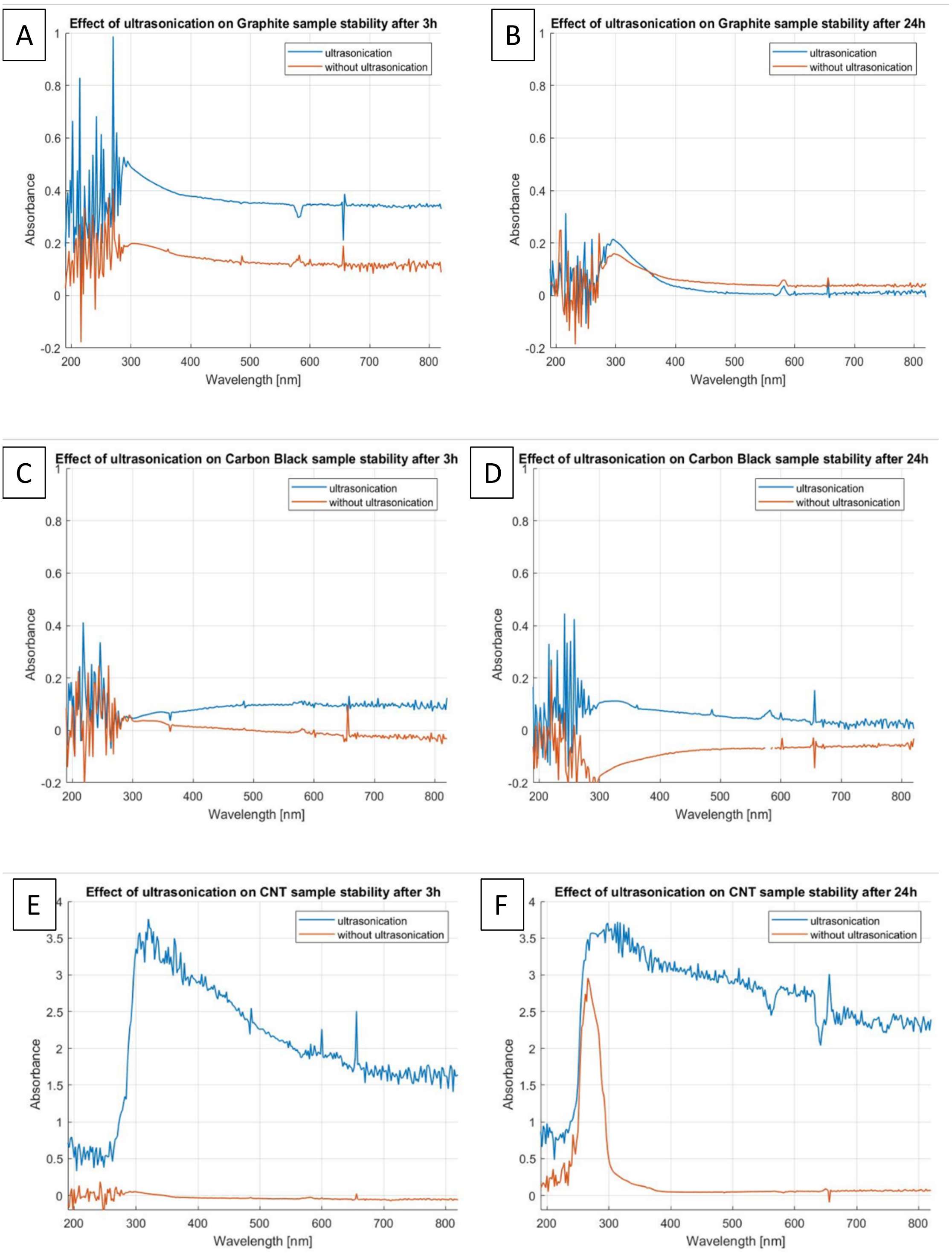

Figure 3.16 - Effect of ultrasonication (blue lines) on allotropes stability 3 hours and 24 hours after ultrasonication. Sample G after 3 hours (A) and 24 hours (B); sample CB after 3 hours (C) and 24 hours (D); sample CNT after 3 hours (E) and 24 hours (F).

Table 3.3 - Precipitated Mass Fraction [%] for G, CB and CNT sample evaluated at 3 hours and 24 hours. Comparison between sonicated and not-sonicated samples.

Precipitated Mass Fraction [%] for G sample

	Sonicated	Not-sonicated
3 h	96.3	98.5
24 h	98.4	98.8

Precipitated Mass Fraction [%] for CB sample

	Sonicated	Not-sonicated
3 h	99.6	99.7
24 h	100.0	100.0

Precipitated Mass Fraction [%] for CNT sample

	Sonicated	Not-sonicated
3 h	o.o.r.[a]	100.0
24 h	o.o.r.	100.0

[a] o.o.r.: out of the linearity range for the conversion from absorbance to concentration

A great difference between sonicated and not-sonicated samples resulted for MWCNTs with respect to the other allotropes, meaning that the ultrasonication procedure brought considerable benefits to the CNT samples stability. This positive effect was retained for long times, as proved by the absorbance spectra at 3 hours and 24 hours (Figure 3.16E - 3.16F). As reported in the Table 3.3, the Precipitated Mass Fraction of CNT sonicated sample couldn't be computed. This issue was related to very high 300 nm absorbance value for 3 hours and 24 hours (respectively 3,36 A.U. and 3,29 A.U.), far above the upper limit of the linearity range (equals to 2,32 A.U.) defined through the CNT calibration curve. Since this upper limit relate with a sample concentration of 0,1 mg/mL (see Figure 3.15), it was possible to infer that the supernatant sample concentration was far above that concentration and the Precipitated Mass Fraction at 3 hours and 24 hours very little.

On the other hand, Graphite sample seemed to have received poor mid-term benefits from ultrasonication, as it is visible from Figure 3.16A and Table 3.3, in which the difference between The Precipitated Mass Fraction of sonicated and not-sonicated samples at 3 hours is reduced. In addition, this narrow gap is completely nullified at 24 hours, meaning that ultrasonication was not able to increase the long-term stability of the G sample (Figure 3.16B).

Carbon Black stability resulted to be totally unaffected by the sonication procedure, since no differences are visible between sonicated and not-sonicated samples neither at 3 hours nor at 24 hours (Figure 3.16C – 3.16D and Table 3.3).

In the light of these results and the difference between precipitation behaviors of the three tested allotropes, an investigation on the causes of this peculiar behavior could be performed from our data and results: the three tested samples, i.e. G, CB and CNT, are chemically identical, being composed only by a graphitic structure enriched with SP molecules, with a functionalization ratio between SP oxygenated moieties and CA around 10% for all samples (see chapter 3.2.1 – Analysis of Graphene-based nanomaterials composition). The differences found among the different CA involve the architecture in which graphene is organized, thus divergent precipitation behaviors could be probably linked with the intimate graphitic structure and not to their chemical composition.

We speculate that these differences are caused by peculiarities in the formation of CNTs aggregates: whereas G and CB tendency to aggregate is only caused by their hydrophobic nature, for CNTs the entanglement phenomenon should be also considered [82].

Based on our results, we could claim that ultrasonication is capable to disrupt large tangles of CNTs, whose filaments could create a wide network which prevents them from reaggregation and precipitation in a short time [83]. We hypothesized that such a dispersion of untangled nanotubes is characterized by a high entropy, a disordered state which difficultly will be reversed in the short/medium terms. This phenomenon should not affect G and CB suspensions since their characteristic structures would obstruct any type of entanglement. Further analysis (e.g. TEM/SEM micrographs taken after the ultrasonication process or molecular dynamics simulations) should be carried out in order to confirm these hypotheses.

The following paragraphs will clarify the precipitation behaviors of each single allotrope, describing in detail their precipitation phenomena over time through 3 hours kinetics measurements.

Graphite

As reported in Figure 3.17, Graphite sample stability showed a time-dependent behavior. Absorption spectra indicated a gradual decrease of absorbance during time: the absorbance value at 300 nm was 80% lower 3 hours after ultrasonication with respect from the starting value (30 minutes after ultrasonication, Figure 3.17B), indicating poor stability of the sample under the examined experimental conditions. This dramatic loss in sample stability occurred after the first 30 minutes, as it is demonstrated from the huge gap between curves at 30 and 60 minutes in the entire kinetics depicted in Figure 3.17A.

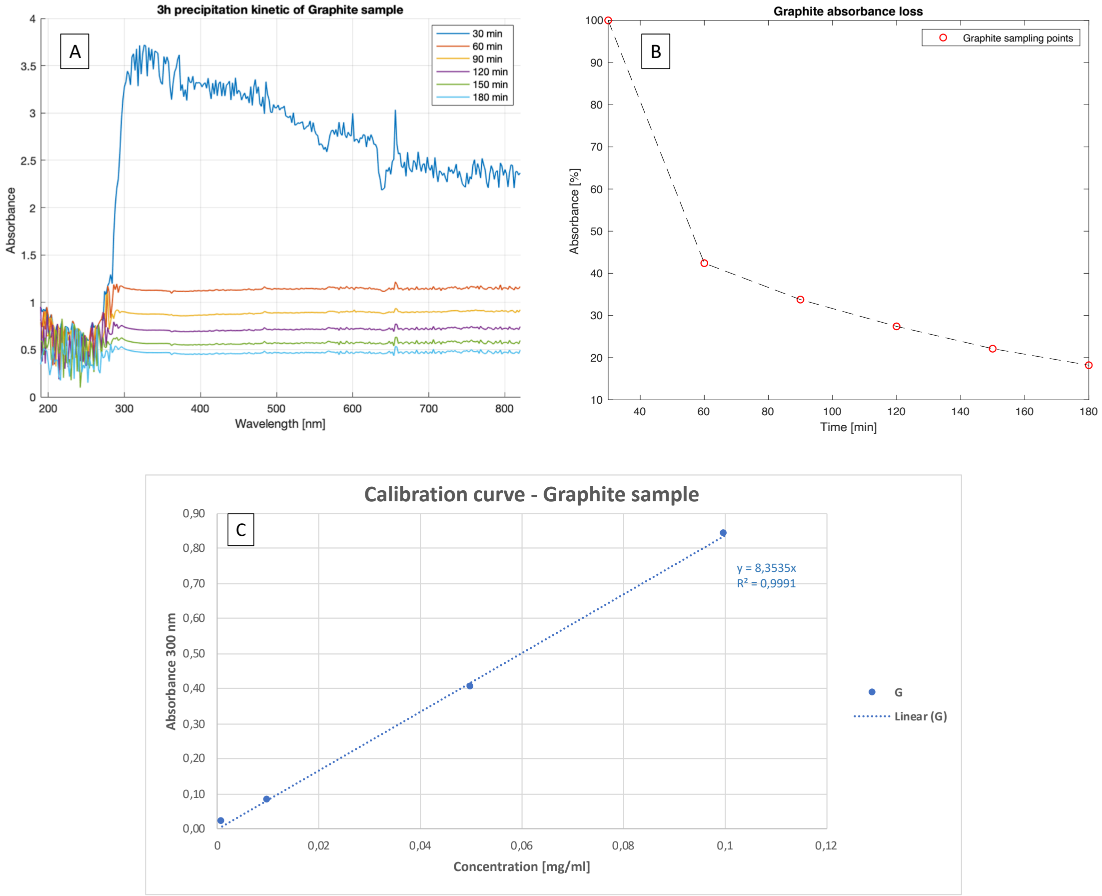

Figure 3.17 - (A) Absorbance spectra for G sample at different times: 30, 60, 90, 120, 150, 180 minutes after ultrasonication. Absorbance values were recorded using pure PBS as the blank solution (PBS $_{Absorbance}$ = 0); (B) Absorbance loss (as percentage [%] with respect from initial value at 30 minutes) as a function of time; (C) Graphite sample calibration curve.

Carbon Black

Ultrasonication was less less effective on CB sample: the sample lost approximately the 90% of its absorbance at 300 nm during the 3 hours evaluation (Figure 3.18B). This proved that the ultrasonication effect is completely reversible in a very short time. As for Graphite, a huge decrease in stability was detectable during the second half of the first hour (Figure 3.18A).

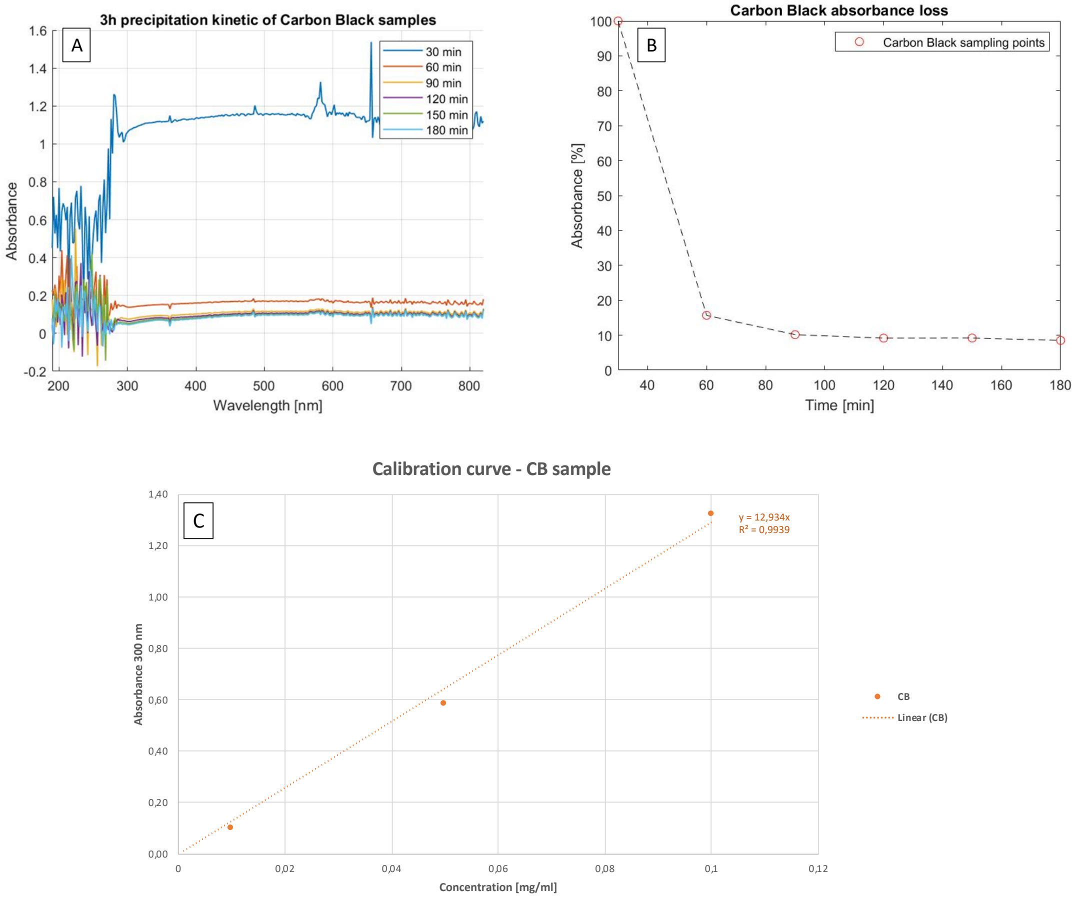

Figure 3.18 - (A) Absorbance spectra for CB sample at different times: 30, 60, 90, 120, 150, 180 minutes after ultrasonication. Absorbance values were recorded using pure PBS as the blank solution (PBS $_{Absorbance}$ = 0); (B) Absorbance loss (as percentage [%] with respect from initial value at 30 minutes) as a function of time; (C) CB sample calibration curve.

Multi-walled Carbon Nanotubes

As previously mentioned, ultrasonication was very effective in the case of CNT with respect from G and CB samples: the sonicated sample was able to retain a high 300 nm absorbance value during the whole 3 hours kinetics, with an absorbance loss of approximately 10% after 3 hours compared with the starting values (Figure 3.19A - 3.19B).

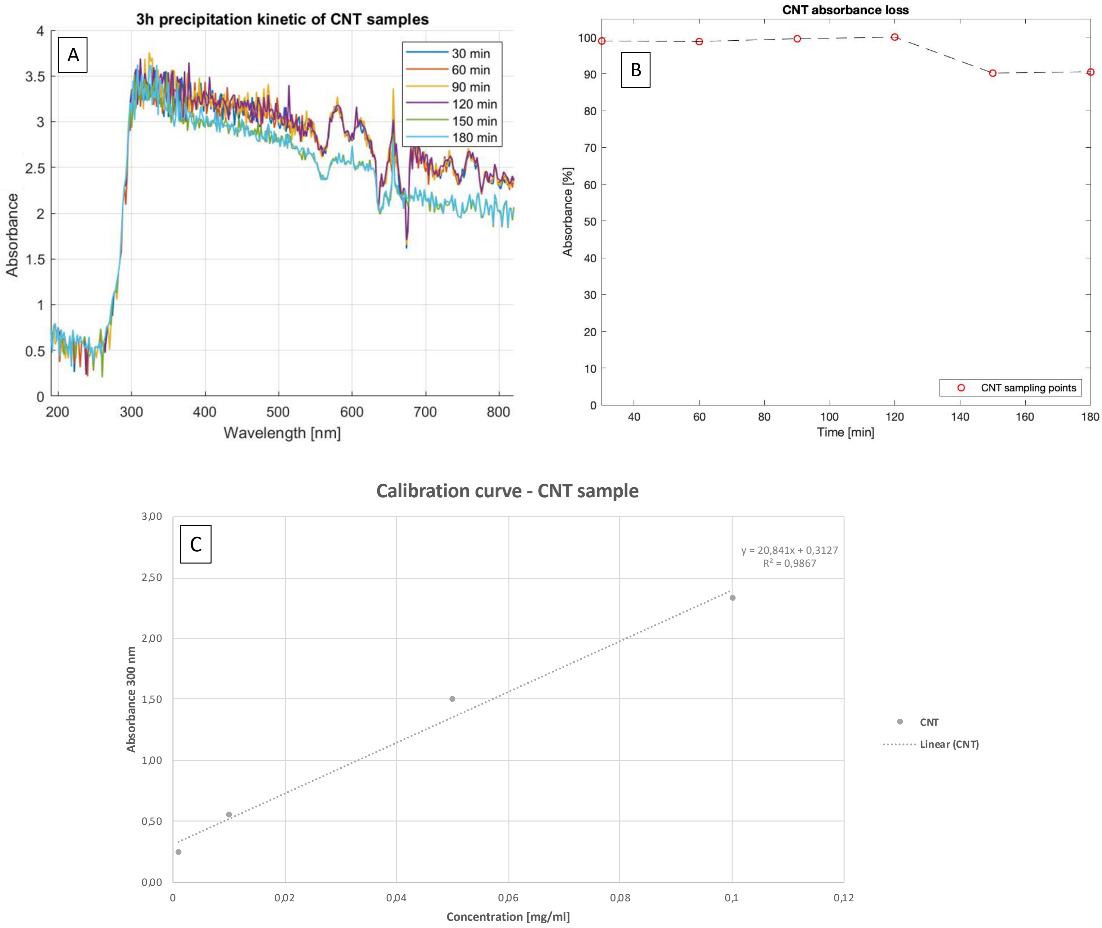

Figure 3.19 - (A) Absorbance spectra for CNT sample at different times: 30, 60, 90, 120, 150, 180 minutes after ultrasonication. Absorbance values were recorded using pure PBS as the blank solution (PBS $_{Absorbance}$ = 0); (B) Absorbance loss (as percentage [%] with respect from initial value at 30 minutes) as a function of time; (C) CNT sample calibration curve.

Taken together, these results bring to light the importance of taking into account the precipitation phenomena caused by the hydrophobic nature of sp^2 CA: especially for G and CB, significant precipitation occurred in a very short time (in the order of minutes). It is evident that ultrasonication is not sufficient to guarantee a proper mid/long-term stability of the examined CA-Ag suspensions under the examined experimental conditions. Nonetheless, it is worth of note that the ultrasonication process is extremely important to ensure a proper dispersibility in the very first minutes from the preparation of the starting suspension. In fact, ultrasonication allows to break down macroscopic aggregates: this means that small aggregates of each allotrope stood still in the solution in the very first minutes after sonication, avoiding pellet formation. This condition of higher homogeneity allows to manipulate carbon-based suspensions in order to produce samples or dilution of samples at desired concentrations. In this framework, we suggest that our ultrasonication procedure (see chapter 2.3.4) represents a good solution to overcome issues related to the serial dilution process of carbon-related materials dispersed in solvents not optimal for their solubilization.

In conclusion, despite the functionalization with an oxidized pyrrole compound (i.e. SP) and the ultrasonication procedure, a poor enhancement of CA-Ag dispersibility was obtained. The disrupting action of ultrasonication procedure was indeed reversible: agglomerates tend to reaggregate over time and eventually precipitate. Thus, dealing with long term incubation of bacteria with samples, further improvements of the setup were necessary.

Hence, a self-designed and home-made rotating tube system was specifically designed and manufactured in order to avoid precipitation of agglomerates maintaining the uniformity of our suspensions during the incubation process.

3.2.4 DLS and ELS analyses

Dynamic light scattering (DLS) measurements allowed to estimate the size of suspended particles derived from dispersion of the three types of CA used (CB, G, CNT) under three different experimental conditions: not-sonicated sample in phosphate buffer solution (PBS), sonicated sample in PBS and sonicated sample in 50% (v/v) PBS/LB.

One of the advantages of this kind of measurement is to provide information about the dimension of particles dispersed into a solution. Results are given in terms of hydrodynamic diameter (D_H), while the polydispersity index (PDI) provide information regarding the distribution of such dimensions: the higher the PDI, the larger the distribution of dimensions. As a drawback, DLS analysis relies on a significant shape approximation: measured D_H corresponds to the diameter of a hypothetic spherical particle which moves at the same speed of the tested sample, thus significant errors could be made during analysis of stretched or planar particles [84].

Despite the CA functionalization with SP, their dispersibility in PBS proved to be lower than expected during preliminary tests. To overcome problems related to low homogeneicity of the samples we decided to ultrasonicate them, in order to disrupt large aggregates of CA-SP-Ag compounds improving powders dispersibility.

An issue was found during analysis of MWCNTs: both ultrasonicated samples (i.e. ultrasonicated sample in PBS and ultrasonicated sample in 50% PBS/LB) results reported a wide distribution of D_H (PDI = 1, the maximum value) with average size of 7785 µm and 3333 µm respectively, whilst for the not-sonicated sample the particle size was even out of DLS measurable range (i.e. between 10 nm and 10 µm.

This was probably caused by the presence of long floating filaments which interfered with size measurements of this specific allotrope: the MWCNTs supernatant before ultrasonication was visibly heterogeneous, with macroscopic particles probably generated by entanglements between filaments (Figure 3.20 – on the left) whereas, even if the ultrasonication macroscopically improved MWCNTs dispersibility (Figure 3.20 – on the right), aggregates still remained visible in ultrasonicated samples.

In addition, the light scattered by larger particles often swamp the light scattered by smaller ones since the light intensity is proportional to the diameter of the particle in the sixth power. These phenomena probably contributed to a huge overestimation of particle sizes during analysis [51].

These issues were corroborated by error messages from instrumentation, often reporting that not-sonicated PBS suspension of MWCNTs was not suitable for measurements (we decided to reduce concentration from 0.5 mg/mL to 0.05 mg/mL in order to overcome this issue, nevertheless error messages still seldomly appeared).

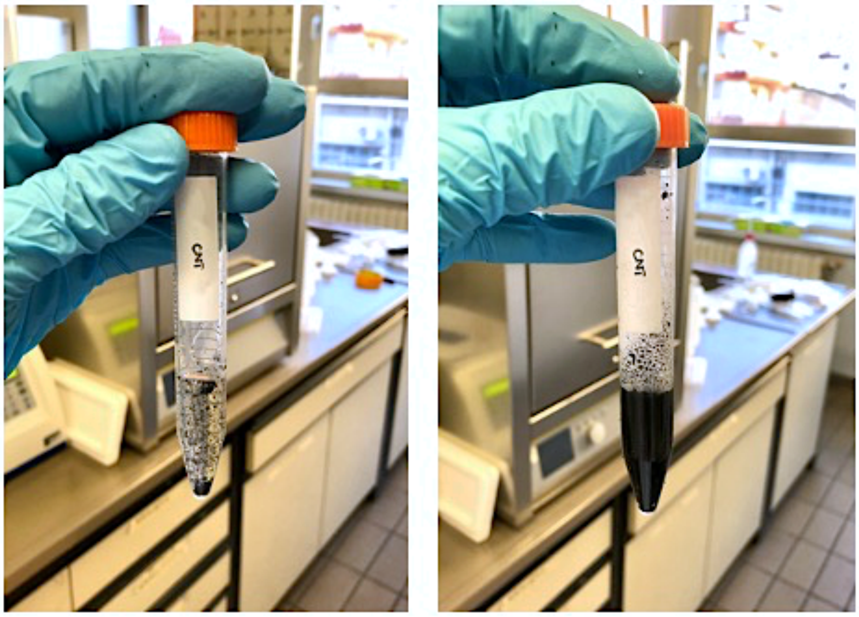

Figure 3.20 - Influence of ultrasonication on CNT sample. Not-sonicated sample on the left, sonicated sample on the right.

These findings, together with visual examination of samples, led us to suggest that DLS was not the optimal method for the characterization of suspended MWCNTs particles, despite the presence of scientific literature even suggesting that carbon nanotubes diameter and length could be computed from DLS results by combining this technique with Raman spectroscopy [49]. Probably the major cause of this outcome was attributable to the use of PBS during our measurements, whilst the majority of researchers we referred to used dH_2O as dispersant [49], [51], [85].

Results were different for Graphite and Carbon Black samples: suspensions were visibly homogeneous after ultrasonication, without precipitates nor macroscopically suspended particles. The sonication process supplied the energy needed to break large aggregates from the original suspension, creating a population of particles characterized by evenly distributed dimensions. The difference between not-sonicated and sonicated samples was particularly evidenced for Carbon Black: despite comparable D_H results, sonicated sample in PBS showed the lowest PDI (0.240 for the sonicated sample against 0.856 for the not-sonicated sample), indicating a monodispersed population of particles with D_H centered around 1447 µm. This discrepancy was not observable for Graphite samples probably because of the higher solubility of this allotrope, therefore, not-sonicated and sonicated samples were similar regarding both sizes (average D_H: 1912 µm and 1965 µm respectively) (Figure 3.21) and PDI (0.309 and 0.278 respectively) (Table 3.4). These results corroborate the presence of microscopic aggregates found in HRTEM micrographs (chapter 3.2.2 – Structural and dimensional analyses).

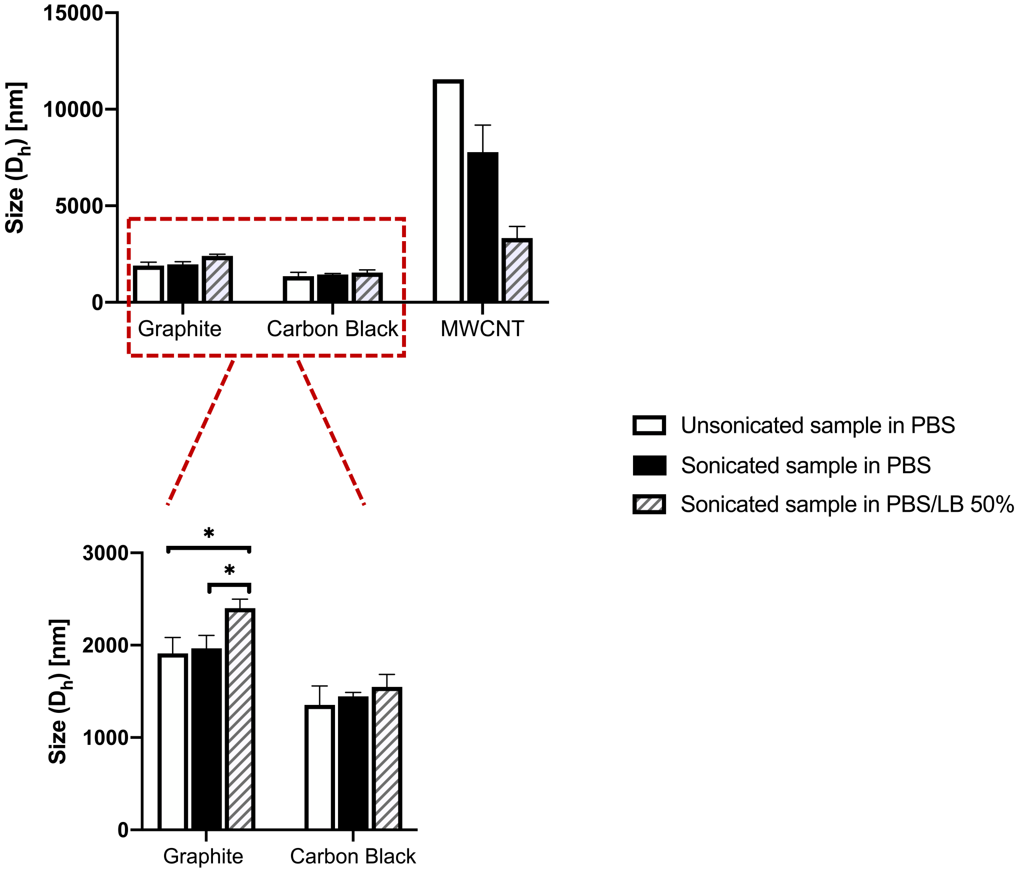

Figure 3.21 - Size comparison between allotropes tested under three different experimental conditions. The lower part of the image represents the detailed situation for Graphite and Carbon Black samples.

Table 3.4 - PDI values of CA under three tested different experimental conditions.

PDI values

	Not-sonicated sample in PBS	Sonicated sample in PBS	Sonicated sample in 50% (v/v) LB/PBS
Graphite	0.309 ± 0.050	0.278 ± 0.121	1.000 ± 0.000
Carbon Black	0.856 ± 0.107	0.240 ± 0.024	0.644 ± 0.092
MWCNT	1.000 ± 0.000	1.000 ± 0.000	1.000 ± 0.000

Overall, our samples displayed different sizes when dispersed in PBS or in 50% (v/v) LB/PBS. Our findings suggested that the presence of proteins like those included in LB medium could have lead to a mild increase in particle dimensions. We attributed this behavior to aggregation of proteins around carbon particles. The hypothesis of an external protein corona is strengthened by scientific literature [86], [87] and our ELS results, which reported a significant decrease of ZP in case of dispersion of powders in LB/PBS medium for every allotrope (Figure 3.22).

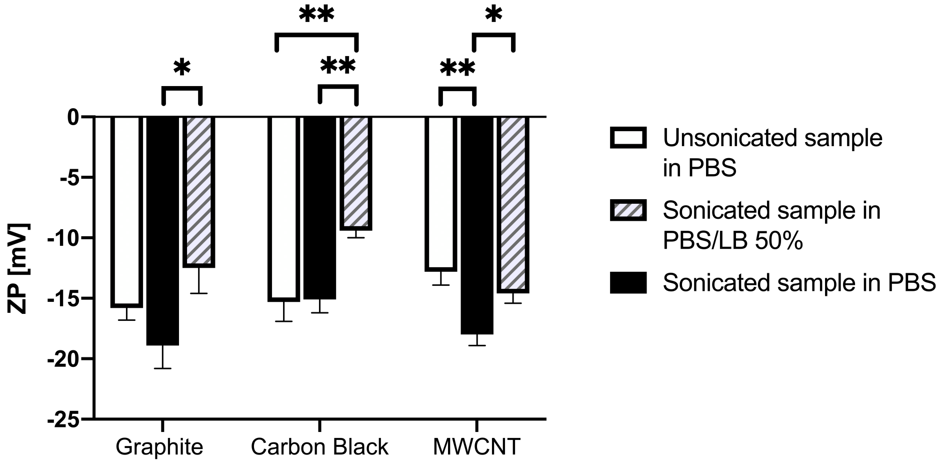

Figure 3.22 - Comparison of Zeta potential between allotropes tested under three different experimental conditions.

3.2.5 Analysis of Ag^+ release

Whereas the characterization of powders and suspension could be considered concluded by now, the role of Ag inside our compounds has to be investigated more deeply. A dedicated analysis for the quantification of Ag release from our CA-SP-Ag samples was performed with the aim to evaluate the presence of Ag^+ ions inside our suspensions.

A detailed and previously tested chemical procedure for Ag^+ ions quantification had been designed for our purpose. This method is based on the assessment of CrO_4^{2-} concentration through a titration assay. From this concentration, Ag^+ ions concentration was easily derived.

As outlined before (chapter 2.3.6 – Ag^+ ions detection assay), the following calibration curve (Figure 3.23) was obtained from Professor Galimberti's chemistry group (ISMaterials) in order to identify the assay sensibility and the Lambert-Beer's law working range. The linearity range was tested between Absorbance values at 375 nm of 0.01 and 0.20 (A.U.). Nevertheless, basing on results from the $AgNO_3$ control sample (2000 μM), we suggest it is possible to extend this linear range at least to 1 A.U., since the linearity was maintained up to this value.

The obtained equation will be useful to convert absorbance values at 375 nm into concentration values of Ag^+.

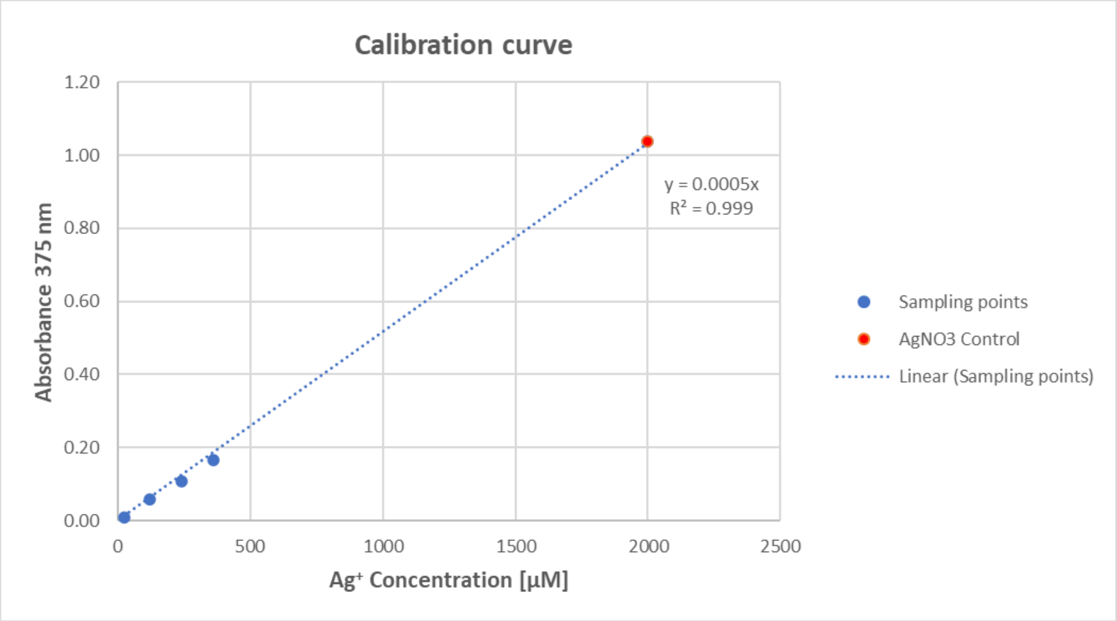

Figure 3.23 - Calibration curve for Ag+ ions detection. The curve equation and the R^2 parameter are provided. The $AgNO_3$ control sample is pointed out with a red dot. Sampling Ag^+molarity: 2000 µM. estimated value (from linear equation): 2077 µM.

The assay was preliminary performed on G650, CB650 and CNT650 samples suspended in PBS and resulted in an impossibility to quantify the Ag^+ content: the titration test was interrupted when, after the addition of K_2CrO_4 to the supernatant, no red precipitate was observable inside all samples. To verify whether this problem was due to the solvent or it was caused by a no-release condition, the assay was next repeated substituting PBS with deionized water (dH_2O - experimental condition different from future antimicrobial screening tests).

Results indicated a low, but detectable Ag^+ ions release in dH_2O for G650 (Figure 3.24A) and CB650 (Figure 3.24B). For CNT650 (Figure 3.24C) a higher Ag^+ supernatant content was detected. Results are merged in Figure 3.24D and Ag^+ molarities for each allotrope were obtained from relative absorbance values at 375 nm and merged in Table 3.5.

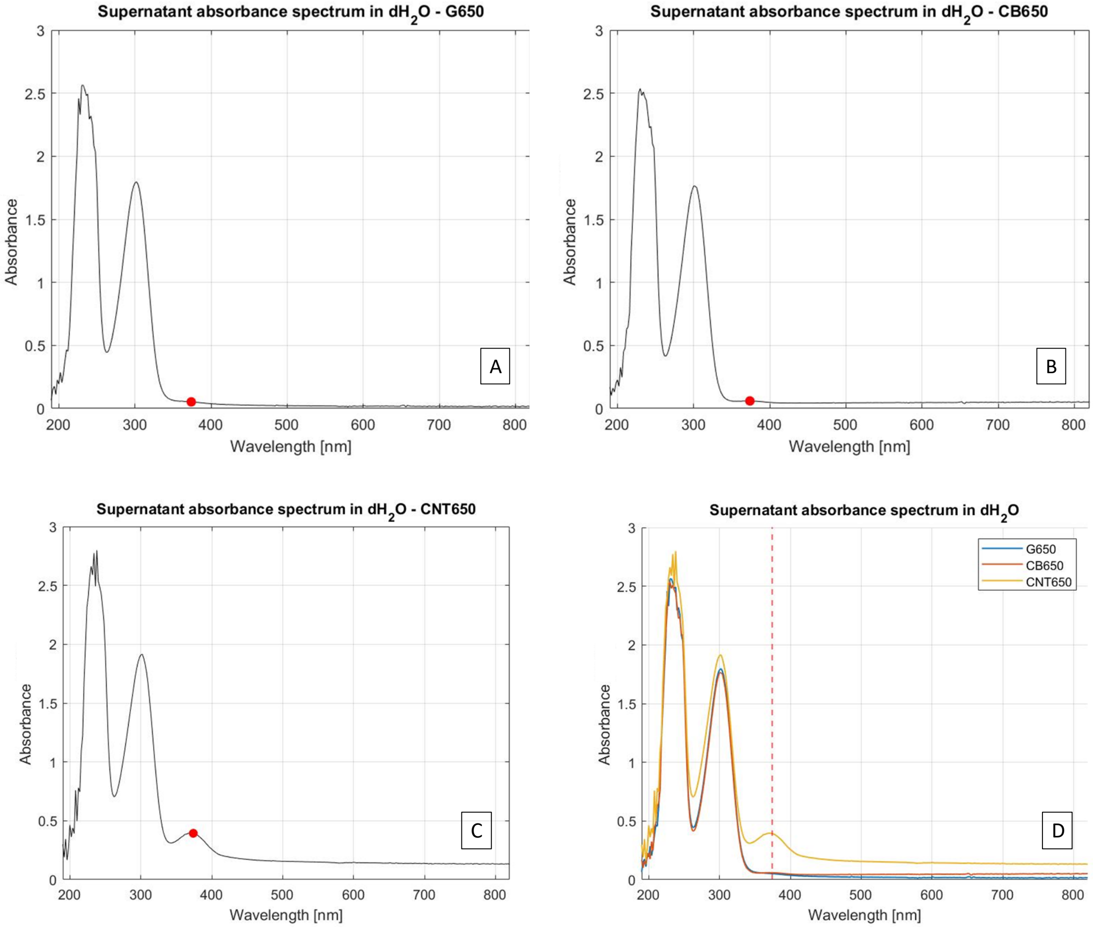

Figure 3.24 - UV-vis supernatant spectrum in dH₂O. The red dot marks the absorbance at 375 nm. (A) Sample G650; (B) sample CB650; (C) sample CNT650; (D) cumulative results for the three tested allotropes.

Table 3.5 - Ag^+ ions concentration in dH₂o and Ag released fraction [%] over total Ag amount inside '650 functionalized samples.

Quantification of Ag^+ release - dH_2O assay

	Ag^+ Supernatant Concentration [μM]	Released Ag [%]
G650	103,9	5
CB650	119,0	6
CNT650	786,7	39

As a first result, we hypothesized that the different Ag^+ release between PBS and dH_2O could have been caused by the ionic content inside these two different solvents: the presence of 0.9% (w/v) NaCl in PBS could hamper the Ag^+ release since silver cations tend to react with dissociated Cl^- anions to form AgCl [58], a white insoluble salt which precipitate during the centrifugation step falling into the discarded pellet. Its formation was confirmed when pure $AgNO_3$ was added in PBS, instantaneously causing the massive precipitation of a white compound. This phenomenon was already reported by Chambers et al. [57], where the effect of PBS on antimicrobial properties of Ag is evaluated.

This could explain the different behavior of samples dispersed in dH_2O: the lack of NaCl allows the release of Ag^+.

Comparing the supernatant concentration of Ag^+ ions detected in dH_2O with the total Ag concentration inside pristine CA-SP-Ag suspensions, it is clearly observable how the entity of the Ag^+ release phenomenon is relatively low (5 – 6% of the entire Ag content for G650 and CB650 samples). The highest Ag^+ content inside CNT650 sample could have been caused by an assay bias: despite a preliminar centrifugation step, MWCNTs stability in dH_2O resulted to be slightly higher than G650 and CB650, thus a fraction of this sample did not precipitate after centrifugation remaining in the supernatant during the analysis. For this reason, we hypothesized that a small amount of Ag^+ ions was strongly bonded to nanotubes without being released.

Such a problem prevent us from claiming with confidence the presence of very low quantity of Ag^+ ions inside our suspensions, even though we can suggest the amount of these species should be minimum or absent during antimicrobial screening tests due to the use of PBS as dispersant [57].

Inductive Coupled Plasma – Mass Spectroscopy (ICP-MS) could represent the most valid and reliable alternative for future developments concerning Ag^+ ions detection, however, high costs often lead to the exclusion of this kind of analysis during characterization experiments.

3.3 Evaluation of the antimicrobial efficacy of CA-SP-Ag suspensions

The crucial part of this work concerned the assessment of the antibacterial efficacy of our Ag-functionalized graphene-based materials. After the characterization process, useful to better understand CA-SP-Ag structural and chemical features which may be involved in the antibacterial activity of such materials, the experiments were set up as previously described in chapter 2.4 – Antibacterial activity of CA-SP-Ag suspensions. Briefly, antibacterial properties of CA-SP-Ag suspensions were tested at different concentrations administering them to *E. coli* inoculum and incubating the whole for 24 hours in controlled conditions of temperature, relative humidity and shaking parameters.

With a focus on culture medium, our first choice fell on 50% (v/v) diluted LB/PBS. LB broth provides nutrients and proteins for optimal viability conditions of bacteria, nevertheless, these environmental conditions seemed to dramatically hamper antimicrobial properties of the tested samples (experiments carried out only for G, G350 and G650). In accordance with these preliminary results (our choice was supported by DLS and ELS results reported in chapter 3.2.4 – DLS and ELS analyses), along with the tested and widely reported inhibition of the antibacterial properties by the nutrient broth protein adsorption on graphene materials [70], [88], we decided to change culture medium: antibacterial screening tests were performed in LB/PBS 1% (v/v) medium which provided the physiological amount of salts required by cells together with small amounts of nutrients to prevent starvation of bacteria.

Following this antibacterial screening procedure allowed us to obtain dose-response curves from which the antimicrobial activity of each compound was evaluated.

Before start showing antimicrobial results, we think it’s worth to mention a practical challenge encountered during experiments: the antimicrobial activity of nanomaterials is usually corroborated by results derived from the measurement of the optical density (OD, i.e. turbidity measurements) together with the direct enumeration of viable CFUs through plate count. OD is measurable by means of spectrophotometers and is a simple, fast and cheap method for the evaluation of bacteria viability inhibition exerted by antimicrobial agents, especially for the estimation of their Minimum Inhibitory Concentration (MIC).

Despite these remarkable features, OD measurements rely on absorbance readings, hence, turbid or colored solutions could potentially cause interferences leading to false-positive results. Moreover, technical issues related to device resolution generally prohibit to measure bacterial concentration below certain values (for example, the OD minimum value of 0.001 A.U. could refer both to 0 CFUs/mL or 10^6 CFUs/mL), leading to false-negative results.

For these reasons, after initial failing OD tests, the evaluation of bacterial viability during our experiments was based on direct plate count of colony-forming units (CFUs). Though this is a time-consuming method, we selected it as the best alternative for antimicrobial evaluations of CA-SP-Ag suspensions considering their black appearance. This choice was supported by literature [23], [89], [90].

Representative images of agar culture plates for the direct count of CFUs at the end of each experiment will be displayed on top of Figures 3.25 , 3.26 and 3.27.

First, the role of the Ag-functionalization was pointed out comparing '350 and '650 samples with their unfunctionalized (i.e. without Ag) counterpart for each allotrope. The following results are represented as CFUs counted vs Sample Ag Molarity [µM]. The less the CFUs counted, the less the bacteria survived in the antimicrobial suspension.

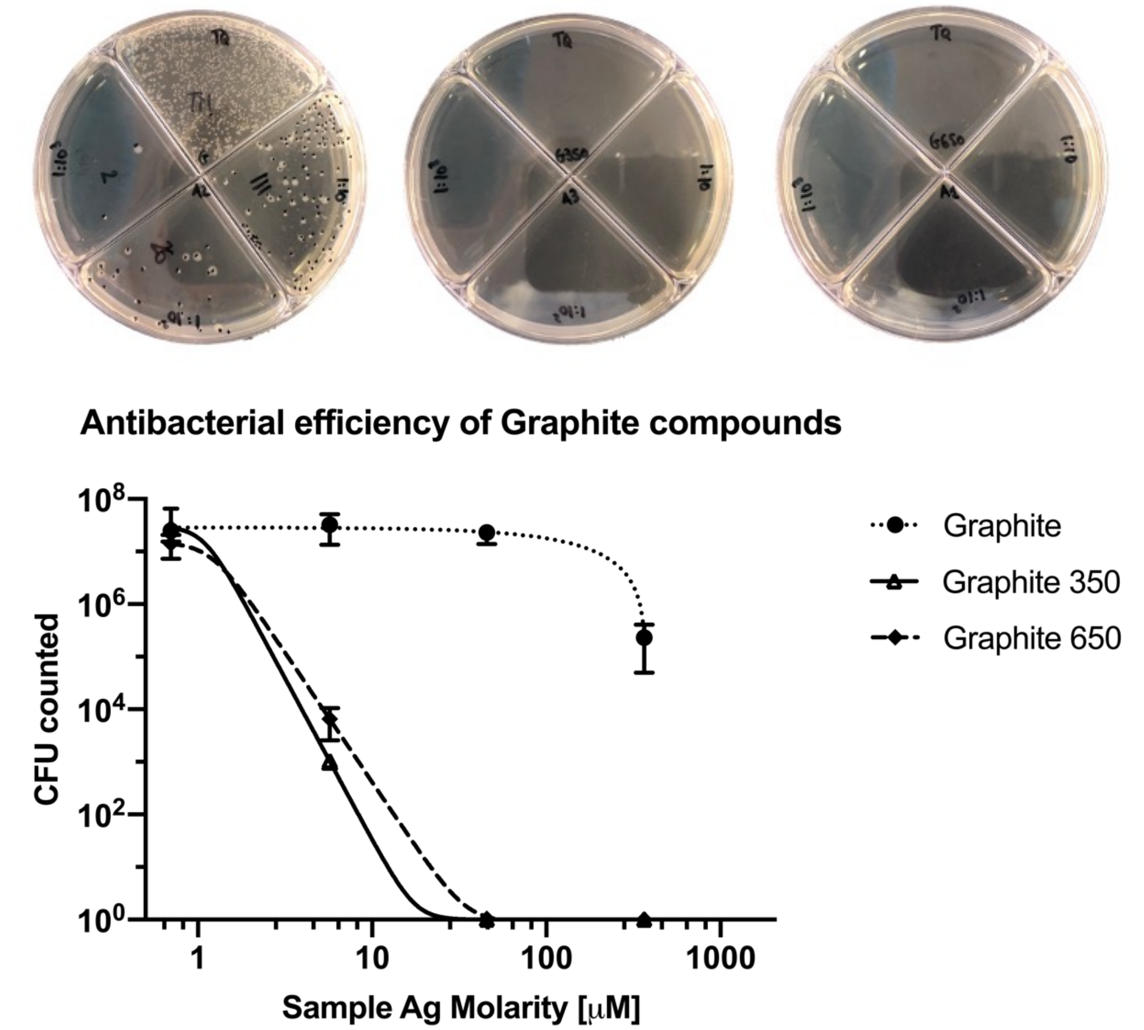

Figure 3.25 - On top: seeded culture plates at the end of antimicrobial experiments. Each plate contains four sectors, each sector delimited CFUs deriving from 1:10 serial dilutions of the starting TQ dilution. These dilutions allow to dilute bacteria to an enumerable range, thus, keeping in mind the dilution factor, one could determine TQ suspension concentration (otherwise impossible to calculate due to the high number of bacteria as it can be seen in the first plate, TQ sector (TM : too much to count)). From left to right, each plate refers to one of the three replicates of the maximum tested concentration (letter A) of G, G350, G650 respectively. Below: dose-resopnse curves of Graphite samples (G, G350 and G650) represented as number of CFUs counted over Sample Ag Molarity [μM]. The unfunctionalized sample (i.e. Graphite) is represented using its Equivalent Ag Molarity [μM]. Each curve is an approximant computed basing on the four experimental sampling points for each compound (dilutions A, B, C, D).

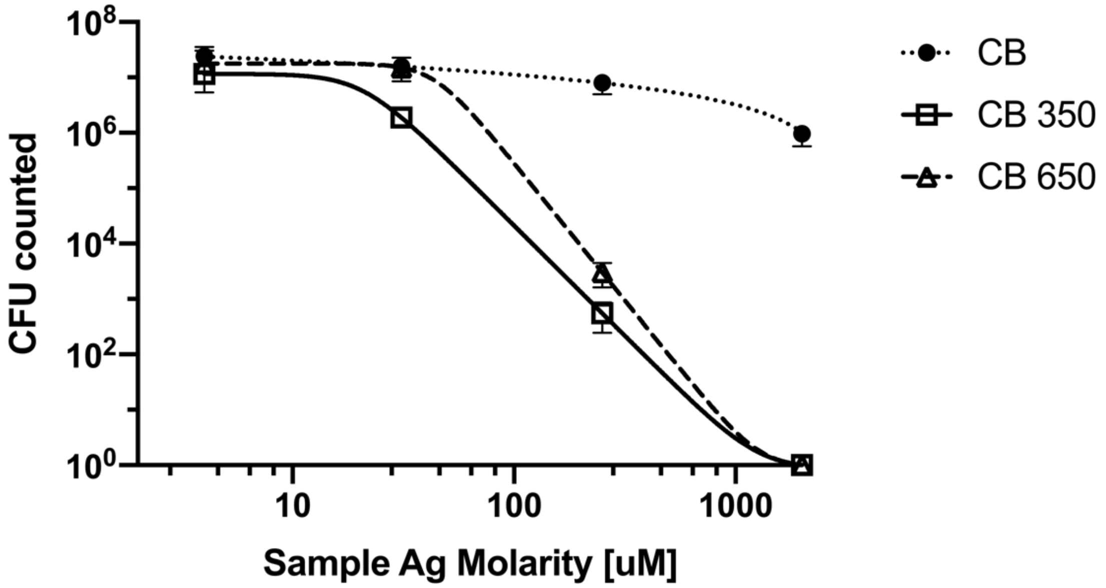
Antibacterial efficiency of Carbon Black compounds

Figure 3.26 - On top: seeded culture plates at the end of antimicrobial experiments. Each plate contains four sectors, each sector delimited CFUs deriving from 1:10 serial dilutions of the starting TQ dilution. These dilutions allow to dilute bacteria to an enumerable range, thus, keeping in mind the dilution factor, one could determine TQ suspension concentration (otherwise impossible to calculate due to the high number of bacteria as it can be seen in the first plate, TQ sector (TM : too much to count)). From left to right, each plate refers to one of the three replicates of the maximum tested concentration (letter A, [Ag] = 2000μM) of CB, CB350, CB650 respectively. Below: dose-response curves of Carbon Black samples (CB, CB350 and CBG650) represented as number of CFUs counted over Sample Ag Molarity [μM]. The unfunctionalized sample (i.e. CB) is represented using its Equivalent Ag Molarity [μM]. Each curve is an approximant computed basing on the four experimental sampling points for each compound (dilutions A, B, C, D).

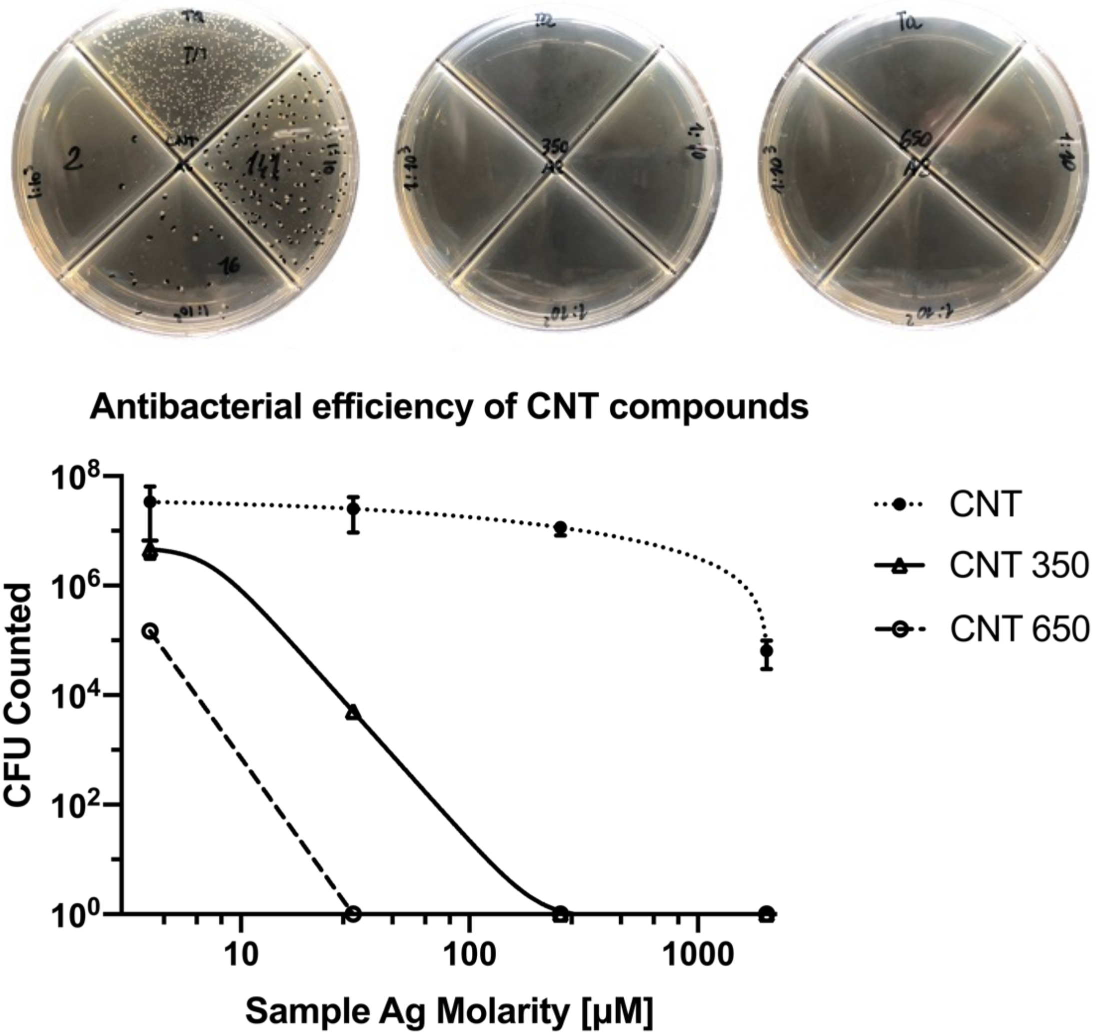

Figure 3.27 - On top: seeded culture plates at the end of antimicrobial experiments. Each plate contains four sectors, each sector delimited CFUs deriving from 1:10 serial dilutions of the starting TQ dilution. These dilutions allow to dilute bacteria to an enumerable range, thus, keeping in mind the dilution factor, one could determine TQ suspension concentration (otherwise impossible to calculate due to the high number of bacteria as it can be seen in the first plate, TQ sector (TM : too much to count)). From left to right, each plate refers to one of the three replicates of the maximum tested concentration (letter A, [Ag] = 2000μM) of CNT, CNT350, CNT650 respectively. Below: dose-response curves of CNT samples (CNT, CNT350 and CNT650) represented as number of CFUs counted over Sample Ag Molarity [μM]. The unfunctionalized sample (i.e. CNT) is represented using its Equivalent Ag Molarity [μM]. Each curve is an approximant computed basing on the four experimental sampling points for each compound (dilutions A, B, C, D).

These findings highlighted a remarkable influence of Ag in the enhancement of antibacterial activity: Ag-functionalized samples, i.e. '350 and '650, exhibited a strong capability to reduce the number of viable bacterial cells over Ag concentration with respect from their unfunctionalized samples. This behavior was observed for each allotrope, strengthening the hypothesis that Ag-functionalization could act as the main enhancer of antibacterial properties.

The estimation of MBC (Minimal Bactericidal Concentration – concentration of antibacterial agent necessary to kill at least 99,9% of bacterial cells) was also possible for Ag-functionalized compounds, i.e. the concentration of antibacterial compound in which it is possible to reach at least the 99.9% of bacterial cells death. Results are reported in Table 1.6.

For not-functionalized samples, i.e. G, CB and CNT, this computation was not possible because, even if such materials exhibited a mild antibacterial activity at high concentrations, they never reached the 99,9% killing threshold which defines the MBC parameter, as it is clearly visible looking at the graphs of Figures 3.25, 3.26 and 3.27.

Table 3.6 - MBC values for Graphite samples (G, G350 and G650). In the first column, values are reported in terms of Ag molarity [μM], while in the second column their counterparts in sample concentration [μg/mL] are reported.

MBC for Graphite samples

	Sample Ag molarity [μM]	Sample concentration [μg/mL]
G	/	/
G350	37.2	87.9
G650	55.5	94.9

MBC for CB samples

	Sample Ag molarity [μM]	Sample concentration [μg/mL]
CB	/	/
CB 350	1236.9	817.3
CB 650	1929.5	778.6

MBC for MWCNT samples

	Sample Ag molarity [μM]	Sample concentration [μg/mL]
CNT	/	/
CNT 350	294.1	184.9
CNT 650	50.4	31.4

Another interesting behavior is easily observable merging results from the graphs and the MBC tables for each sample: looking at ‘350 and ‘650 curves of Graphite and CB samples in the graphs of Figures 3.25 and 3.26, it could be noted the slightly higher antimicrobial efficacy displayed by ‘350 samples (curves below their ‘650 counterparts). This is confirmed by the MBC values expressed in terms

of Ag molarity (first column) in Table 3.6 for Graphite and CB samples: the MBC for ‘350 samples is approximately 1.5 times lower than the ‘650 counterpart.
The MBC values expressed in terms of sample concentration (second column of Table 3.6) should better clarify the real situation: though 350’ samples apparently seem to be the best compounds in terms of antimicrobial activity, comparing samples at the same Ag molarity inevitably lead to the production of ‘350 suspensions at higher concentrations (μg/mL of powders) with respect from ‘650 suspensions. This is due to the lower amount of Ag present in ‘350 samples. Hence, keeping constant the Ag molarity between samples, if one consider a potential antimicrobial effect elicited by the structure of the allotrope itself, is simple to understand how higher concentrations of that compound could potentially cause higher bacterial mortality rates. This concept is strengthened by the MBC values of the second column in the Table 3.6, where lower values of MBC are displayed for ‘650 samples of Carbon Black and CNTs, while results became comparable for Graphite with respect from those of its first column.
This finding is essential from a large-scale production point of view, since a higher loading of Ag during the functionalization phase would lead to the production of powders with enhanced antimicrobial properties, thus lower amount of carbon material will be needed to obtain the same efficacy. Conversely, higher loadings of Ag will necessarily require higher quantity of chemicals involved in the Tollens’ reactive, thus a trade-off between the use of pristine carbon material and the use of chemicals must be considered in this case.

Focusing our attention on the capability of Ag to elicit such an outstanding enhancement of the antimicrobial activity of CA, it is important to clarify which chemical species in our samples could elicit this bactericidal effect: even if its antibacterial performances are renowned from centuries, actually, the scientific literature has not yet clearly established if the bactericidal effect could be elicited by Ag^+ cations [58], [61] or Ag metallic NPs [25] deposited on CA surfaces.
The capability of Ag^+ ions to bind prokaryotes protein thiol groups (-SH) causing their denaturation and eliciting dysfunctionalities in many different metabolic processes (e.g. transmembrane active transport and antioxidant reactions) is

widely reported [5], [63], [91], as well as the formation of complexes between Ag^+ ions and nucleic acids, transmembrane carriers and/or cellular wall [58], [91]. However, different studies indicate the capability of metallic Ag NPs to catalyze the oxidative degradation of membranes and cytosolic content leading to the bacterial cell death. In particular, Davies et al. [5] mentioned that metallic Ag in aqueous medium could act as an “oxygen reservoir”: thanks to its electronic properties and lattice dimensions, metallic Ag collects oxygen atoms in its bulk and, when interfacing with organic content, leads to the formation of reactive-oxygen species (ROS) (e.g. hydroxyl (-OH), epoxide (-O-) and carboxyl (-COOH) free radicals), causing the complete destructive degradation of microorganisms through the membrane lipid peroxidation mechanism [92] (Figure 3.28).

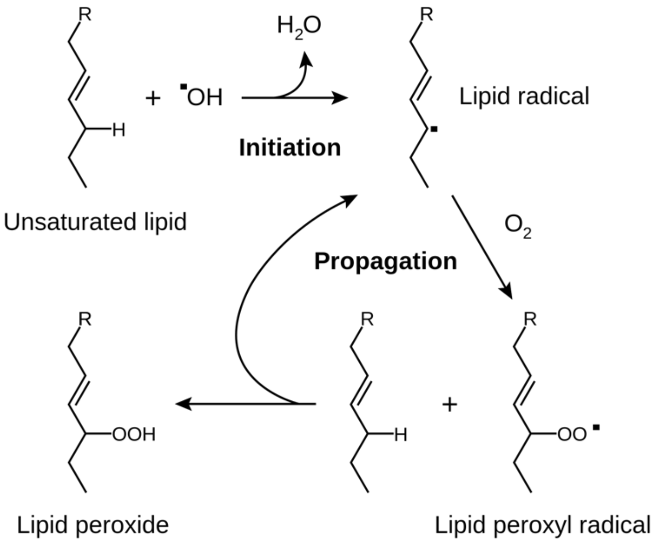

Figure 3.28 - Lipid peroxidation mechanism. The process rely on a free radical chain reaction mechanism which gradually disrupt the lipidic cellular membrane [Tim Vickers, after Young IS, McEneny J (2001). "*Lipoprotein oxidation and atherosclerosis*". Biochem Soc Trans 29 (Pt 2): 358–62].

Generally, while Ag^+ ions are released and diffuse at a certain distance over time, the metallic Ag oxidizing capability seems to be effective only on cells which are in direct contact with NPs and is practically instantaneous [5].

The radical differences between these bactericidal effects lead to distinct antibacterial behaviors, influencing the possible final application of CA-SP-Ag adducts.

The direct evaluation of the Ag antibacterial path renlies on complicated and time-expensive tests, such as the evaluation of glutathione (i.e. GSH) intracellular levels. For this reason, an indirect evaluation was chosen in order to quantify the Ag^+ ions content inside CA-SP-Ag suspensions (see chapter 3.2.5 –Analysis of Ag^+ release).

In the light of results displayed in the previous chapter, we can suggest that the Ag^+ ions influence on the CA-SP-Ag bactericidal efficacy during our antimicrobial screenings should be minimum or absent due to the use of PBS as dispersant. Nevertheless, we can affirm that the major contribute on CA-Ag bactericidal effects will probably derive from metallic Ag NPs [5] and from the allotropes intrinsic architecture [25], thus contact-dependent bactericidal mechanism should represent the most plausible pathway.

Besides the evaluation of the Ag role, a detailed insight on the different antimicrobial activities elicited by the three allotropes should be provided. A comparative analysis of this could be offered from Figure 3.29, where it is possible to graphically investigate whether the antibacterial activity of carbon-related materials was allotrope-dependent or not fixing the variable of Ag molarity. Similar conclusions could be inferred from Table 3.6 comparing MBC values between the three different allotropes.

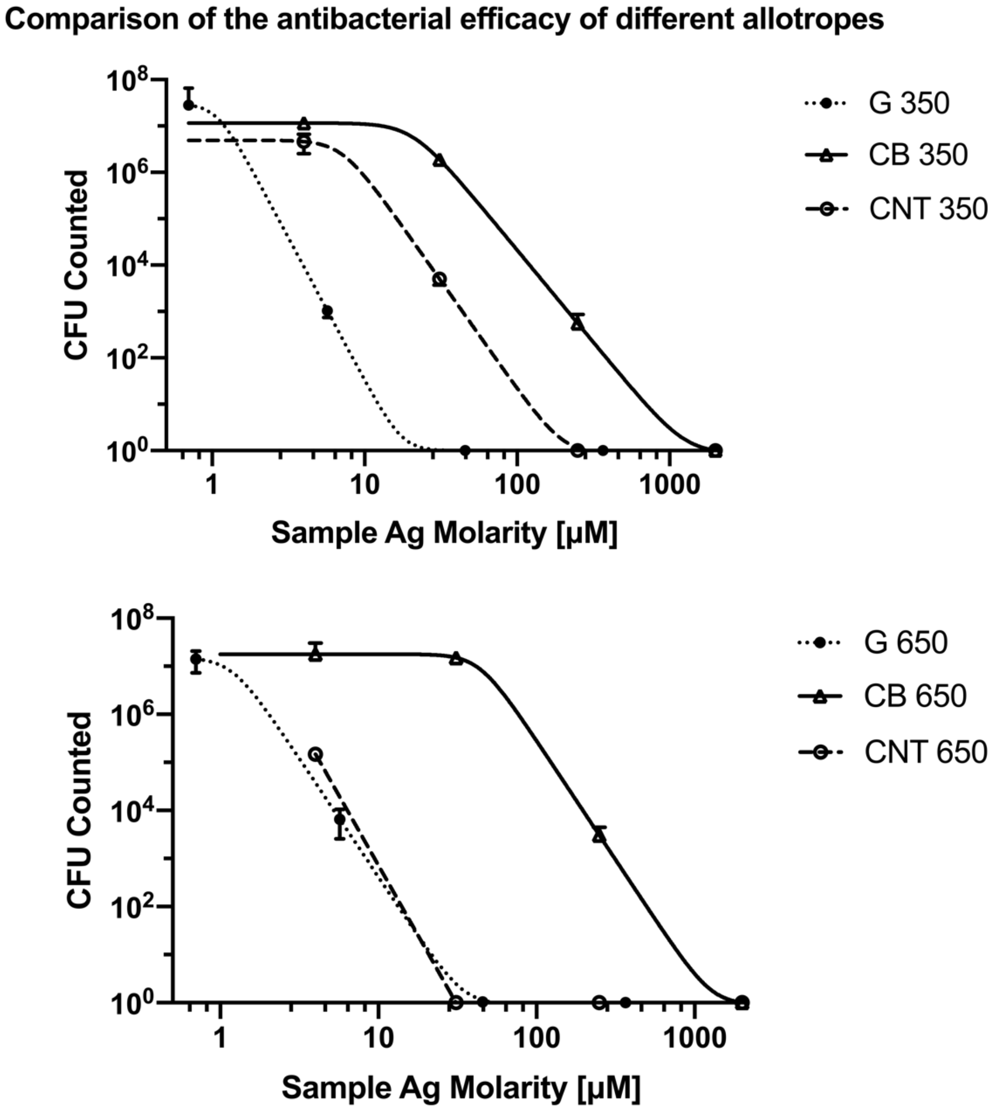

Figure 3.29 - On top: comparison of the antibacterial efficacy among '350 samples, i.e. G350, CB350 and CNT350. Below: comparison of the antibacterial efficacy among '650 samples, i.e. G650, CB650 and CNT650.

Results from the comparisons between '350 samples and '650 samples (Figure 3.29) clearly show how Graphite is the most effective allotrope whereas CB exhibited the lowest antibacterial efficacy. Regarding CNTs, they seem to have an intermediate antimicrobial power between Graphite and CB, even if the behavior of CNT650 is slightly different from its '350 counterpart: the gap between Graphite and CNT curves visible in tha graph on top is significantly reduced in the graph below.

In the light of these results, we believe that the antibacterial efficacy of our compounds relates as well to their nanometric structures and not just to the Ag content. Different arrangements of graphene layers generated characteristic architectures for each allotrope, leading to different modalities of interaction between these carbon nanomaterials and microorganisms.

According to recent achievements, two out of the three principal mechanism of antibacterial action rely on the characteristic structure of graphene, namely, nanoknives, resulting from the action of sharp edges on bacterial membranes (Figure 3.30), and wrapping/trapping of cells caused by the high flexibility of the graphene latticework. The third proposed mechanism involve oxidative stress elicited by the oxygenated groups of oxidated CA mediated with or without the production of ROS (i.e *ROS dependent* and *ROS-independent* mechanisms) [6].

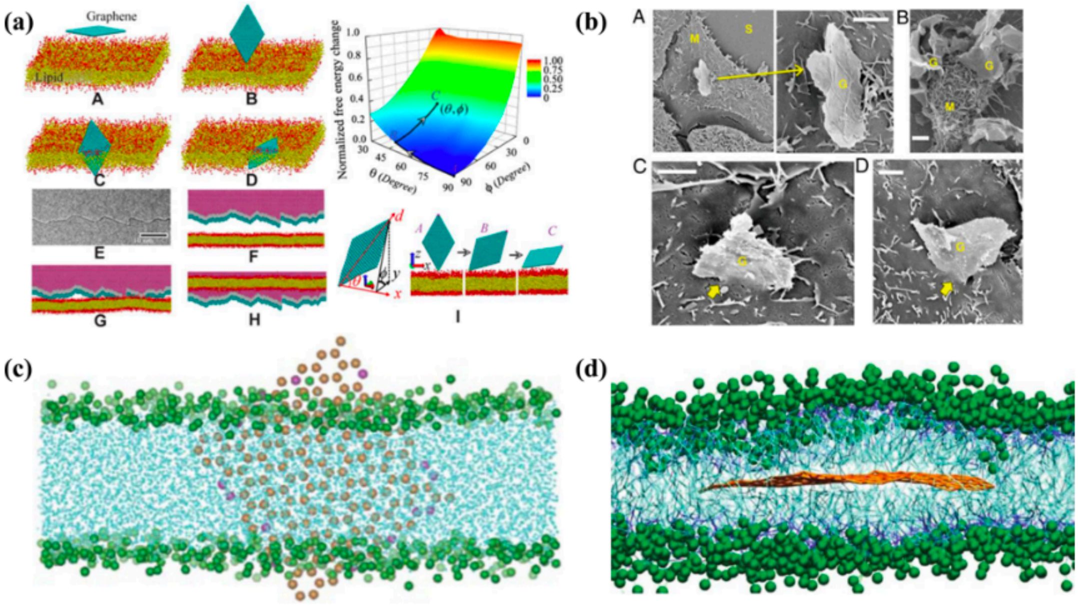

Figure 3.30 - Cell membrane interaction with graphene layers modelled through molecular dynamics simulations (a, c, d) and visualized through SEM micrographs (b) [6].

According to that, one possible explanation for the higher antimicrobial activity of Graphite samples is given by these proposed mechanisms. Graphite is indeed the allotrope which better retain graphene intrinsic layered structure, with sharp edges which could behave as nanoknives and/or high surface area layers which could trap bacteria impeding metabolic exchanges between the extracellular and the intracellular environments. The assumption of such a size-dependent bactericidal mechanism involving graphite was precisely evaluated by Liu et al. [47]. The authors, after a detailed physico/chemical characterization of samples, compared the antimicrobial efficacy of four graphene-based materials, i.e. Graphite (Gt), Graphite Oxide (GtO), Graphene Oxide (GO) and reduced Graphene Oxide (rGO, i.e. GO lacking the majority of oxygen containing groups). Taken together, their findings seemed to suggest that oxidative stress, though present, was not the main factor involved in bacterial death, paving the way for speculations supporting size-dependent bactericidal mechanism of action against *E. coli*.

Similar suggestions could be made for MWCNTs, which could act as nanodarts [4]. This hypothesis is strengthened by a significant study by Kang et al. [93] which reported a significantly higher bactericidal effect elicited by SWCNTs with respect from MWCNTs, leading them to speculate that the different diameter (0.9 nm and 30 nm, respectively) was the principal factor behind their different antimicrobial activities. Higher expression of genes related to cell damage for SWCNTs was detected, suggesting a size-dependent bactericidal mechanism involving membrane disruption.

The allotrope architecture is also fundamental to guarantee a proper interaction between Ag NPs and bacterial cells. In fact, since the antimicrobial effect due to Ag^+ ions release is negligible (see chapter 3.2.5 – Analysis of Ag^+ release), the spatial distribution of metallic Ag NPs on the allotrope surface is extremely relevant: it is worth to remind that the antimicrobial effect driven by metallic Ag is a contact-dependent oxidative degradation phenomenon [5], thus, only Ag NPs which can physically interact with bacterial structures will be able to elicit an antimicrobial activity. With this in mind, allotropes characterized by a high surface area exposed to the environment will benefit of a better Ag-related enhancement of their antimicrobial properties.

The planar geometry of Graphite, along with its high SA/V ratio (335 – 365 m^2/g as specified by the manufacturer), presumably facilitated the contact between surface-grafted Ag NPs and bacteria; moreover, the high tendency to wrap on bacterial cells of such material could significantly improve Ag NPs antibacterial action. CNTs showed similar behavior, probably because of their cylindric geometry characterized by a high exposed surface area (250 – 300 m^2/g). On the other hand, despite CB resulted to be the best-functionalized one, its peculiar clustered-acini structure is hugely disadvantaging for this material since the exposed surface area (78 m^2/g) is lower with respect from that of Graphite and MWCNTs samples, thus a relevant fraction of Ag NPs is localized in small gaps between acini and cannot directly interact with microorganisms. In fact, their dimensions (in the order of μm) prevent them from accessing small nanometric gaps.

In conclusion, results from antibacterial screening tests, along with information provided by the scientific literature, allowed us to claim that antimicrobial properties of CA-SP-Ag compounds are due to the synergic effect between allotropes peculiar architecture and oxidative stress elicited by Ag NPs.

4 Conclusions

The aim of this thesis work was to synthetize, characterize and evaluate the antibacterial activity of three different sp^2 CA (i.e. HSAG, Carbon black and MWCNTs) functionalized with Ag NPs, in order to evaluate how the enrichment with Ag and the differences in the nanometric architecture between CA would affect the antibacterial properties of these nanomaterials.

Our results suggest that the double-stage functionalization of graphene-based materials, i.e. G, CB and MWCNTs, resulted to be a reliable approach to enhance their intrinsic antimicrobial properties.

Functionalization with SP molecules, useful to enrich graphene allotropes with Ag-linking moieties, proved to be an affordable method, capable to assure the desired functionalization ratio between SP oxygenated groups and CA without using metal catalysts and avoiding harmful byproducts.

Ag functionalization was also successfully achieved: dimensional analysis on HRTEM micrographs proved that resulting CA-SP derivatives were properly enriched with Ag NPs, without altering the original nanometric architecture of sp^2 CA.

Results from antibacterial screening tests pointed out the significantly higher antimicrobial activity of CA-SP-Ag derivatives with respect to their not-functionalized counterparts, in particular for G and CNT functionalizes samples.

CA-Ag suspensions showed to be prone to a massive precipitation phenomenon, especially in PBS solution. Beside preliminary optimizations of the antimicrobial screening protocol, e.g. low intensity probe ultrasonication and dynamic incubation, future improvements should be employed to overcome issues related to low samples stability. To this end, we envision strategies to overcome the issues related to Ag-C suspensions stability in static conditions. In particular one approach involves a different functionalization procedure and the other one regards the use of alternative ultrasonication setups.

The SP functionalization, acting as a dispersibility enhancer, did not remarkably influenced sample stability in PBS solution: to overcome this issue the first possibility is to increase the SP functionalization ratio, the second strategy is to substitute SP with another functionalizing molecule such as a different pyrrolic compound.

Increasing the SP functionalization ratio, fixed around 10% (w/w) in our compounds, may be useful to mitigate the hydrophobic nature of graphene-based materials, leading to a better stability in suspension. However, a sharp increase in the functionalization ratio between SP oxygenated moieties and CA could give rise to side effects: the functionalization process could introduce defects and variations into the characteristic atomic order of graphene sheets, causing a loss of mechanical and/or electronical properties of such material [32]. For this reason, an increase of the SP functionalization ratio is feasible as long as these variations are properly evaluated.

Changing the functionalizing molecule could offer an alternative solution: a wide spectrum of different pyrrolic compounds was recently synthesized by ISMaterials (Professor Galimberti's research group) using the same process involved in the SP synthesis [26], with the advantage to obtain molecules with tunable solubility parameters. Even though this could be a suitable alternative, it should be always taken into account that the functionalizing molecule must successfully trigger the Tollens' reaction and bond Ag NPs as well, so only the molecules with specific chemical properties (i.e. with aldehyde groups and electron pairs able to bond Ag) should be considered as good substitutes.

On the other hand, we could try to improve the ultrasonication process to achieve better results in terms of sample dispersibility as well. In our thesis work, we opted for a low intensity probe ultrasonication (10 - 18 W) prolonged for short times (5 minutes), which was able to provide a moderate amount of energy (3.0 - 5.4 kJ) to the sample in order to disrupt larger aggregates. Increasing the ultrasonication intensity and/or time may result in an enhancement of CA-Ag suspensions stability, especially for the short/medium term [83]. However, a possible drawback for this solution could be represented by a significant change of the allotrope architecture: low intensity (<25 W) bath ultrasonication prolonged for long times (up to 460 hours) proved to exfoliate graphene sheets from graphite flakes [30] [94], causing a dramatic alteration of its lateral dimensions, or to elicit CNTs filaments disruption [82]. For this reason, additional investigations (e.g. SEM/TEM micrographs aiming to evaluate morphological changes after ultrasonication) should be carried out to further evaluate the influence of ultrasonication on samples structures. Another drawback related to this strategy concerns the reversibility of the aggregation state of carbon-related particles: the hydrophobic nature of these materials will always be an issue while dealing with polar solvents, thus reaggregation would always occur until further alterations of their chemical structure will be implemented. In our opinion, the synergic action of ultrasonication and chemical functionalization could offer an optimal solution. The disaggregation of clusters provided by ultrasonication could offer indeed a huge increase in the surface area exposed to environment, therefore further oxidation of materials should be more homogeneous and effective even at low doses.

Results of the functionalization with Ag NPs performed by means of the addition of Tollens' reagent were strongly influenced by the specific allotrope: whereas functionalization for CB and CNTs resulted to be generous and evenly distributed, G was poorly enriched by Ag NPs. In our opinion, ultrasonication of samples carried out immediately after the addition of Tollens' reagent could be useful to obtain a better Ag enrichment of CA-SP derivatives.

G and MWCNTs samples were the most promising antimicrobial carbon-related nanomaterials, eliciting a significantly higher bactericidal effect even at low concentrations. Conversely, CB samples were not able to display such a great antibacterial capability, showing a MBC value of approximately one order of magnitude higher than that of G and MWCNTs. Altogether, these results demonstrate an allotrope-dependent behavior, suggesting that the intrinsic differences between allotropes architectures may have induced a better interaction of Ag NPs with bacterial cells in the case of G and CNTs because of

their wrapping ability. Moreover, a synergistic bactericidal effect based on membrane perforation by means of sharp edges of G and CNTs was suggested.
Future studies would be useful to establish the exact mechanism behind the bactericidal effect of our CA-Sp-Ag derivatives: SEM micrographs depicting the interactions between bacteria and the allotropes may represent a first step towards this objective, followed by a further analysis on the antioxidant metabolism (e.g. the evaluation of oxidized GSH intracellular levels [95]) of bacteria.

In this thesis work, the differences between these bactericidal effects are caused by distinct antibacterial interactions between allotropes and microorganisms, influencing the possible final application of CA-Ag compounds. Possible applications might involve the immobilization of our antibacterial CA-Ag nanomaterials on surfaces: in a recent study [69], Pandit et al. thoroughly documented the difference in terms of antimicrobial efficacy between CVD (i.e. Chemical Vapor Deposition) graphene deposited horizontally on the surface with respect from a PECVD (i.e. Plasma Enhanced Chemical Vapor Deposition) vertically aligned graphene. The last deposition method provided outstanding results compared to its counterpart. Further assays excluded ROS-dependent antibacterial mechanisms of action, strengthening the hypothesis of membrane perforation as the principal bactericidal mechanism: the vertical alignment seemed to elicit bactericidal interactions between bacterial external membrane and sharp edges of graphene sheets.
Another application should exploit the antimicrobial properties of CA-SP-Ag derivatives to design and develop surfaces with enhanced antimicrobial effects. The production of inks or thin films with antimicrobial properties represents a promising approach, widely expanding the possible fields of application of graphene-related materials.
In this light, we already tried to design an antimicrobial ink in the very last phase of our work (Figure 4.1), however its development proved to be full of challenging issues whose resolution must be considered one of the main future improvements of this thesis work.

Figure 4.1 – CA-SP-Ag inks prepared dispersing powders in a blend of polycarbonate resin and propylene glycol. From left to the right: G-Ag ink, CB-Ag ink and CNT-Ag ink.

The design of inks or thin films required to disperse our CA-Ag nanomaterials in a polymeric matrix, forming a composite material where the antimicrobial powder is evenly distributed into a supporting matrix, hence, the choice of the proper polymeric material is fundamental. In this light, polymers represent a broad spectrum of different materials with countless perspectives, thus it is possible to specifically tune the ink features, such as density and/or viscosity. Moreover, the last decade paved the way for the design of *smart inks*, capable to react to specific environmental conditions (e.g. temperature, pH, shear stress, etc.) consequently enhancing their properties.

Despite that, the polymeric material should fulfill specific requirements: it should strongly adhere to the surface on which it is applied, it has to guarantee a stable retention of the CA-Ag filler avoiding a rapid surface degradation and, of course, the polymeric blend should be compatible with the ink deposition method (Figure 4.2).

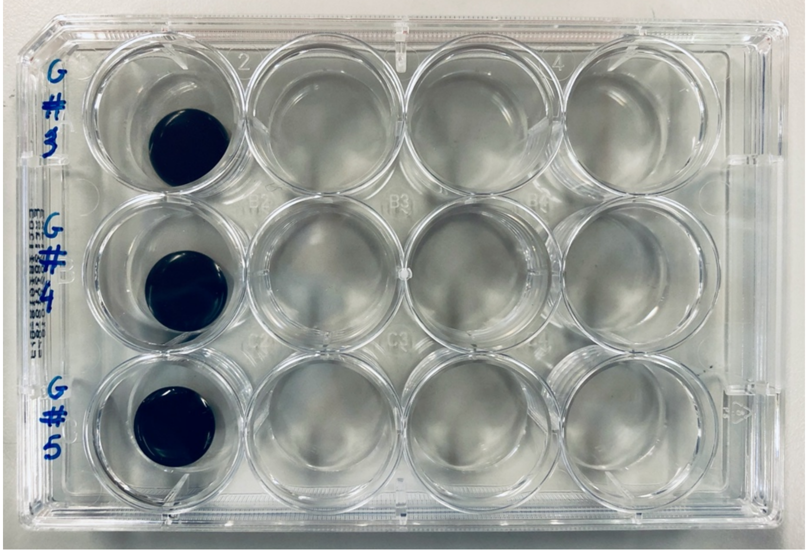

Figure 4.2 - Glass coverslips (Ø ≅ 15 mm) coated with three different formulations of CA-SP-Ag inks by means of a drop deposition method.

This last requirement proved to be a critical aspect while aiming to produce valid specimens suitable for antimicrobial screening tests. Homogeneity and thickness of samples are indeed of primary importance in order to establish the interaction area between specimens and the bacterial inoculum.

To assure all of these requirements, a proper trade-off between the amount of polymeric matrix and the CA-Ag antibacterial filler should be defined: a lack of the polymeric fraction could lead to bad adhesive behaviors and to inadequate viscosities, whilst its overabundance would hamper the antimicrobial features of CA-Ag compounds.

The design of an antimicrobial surface based on our CA-Ag compounds should also take into account the antibacterial performances: as previously discussed in chapters 3.2.4 – Ag^+ release analysis and 3.3 – Evaluation of the antimicrobial efficacy of Ag-C suspensions, we can assume that our CA-Ag compounds exploited the ability of metallic Ag NPs to induce bacterial oxidative degradation. This bactericidal mechanism is contact-dependent and does not involve any type of release from the bulk. This means that only the coating should be effective against bacteria, thus the deposition of thin films could be preferred to thick ones in order to maximize the antimicrobial efficacy while minimizing the waste of material.

An in-depth dedicated study should be carried out to choose all of the possible polymeric candidates to fulfill each requirement and to properly define deposition parameters in order to obtain a functional and adequate ink.

In conclusion, we believe the great versatility of graphene-related compounds, together with their multitude of intrinsic properties in association with their antimicrobial features, would open the way for several applications and future developments in different domains (Figure 4.3).

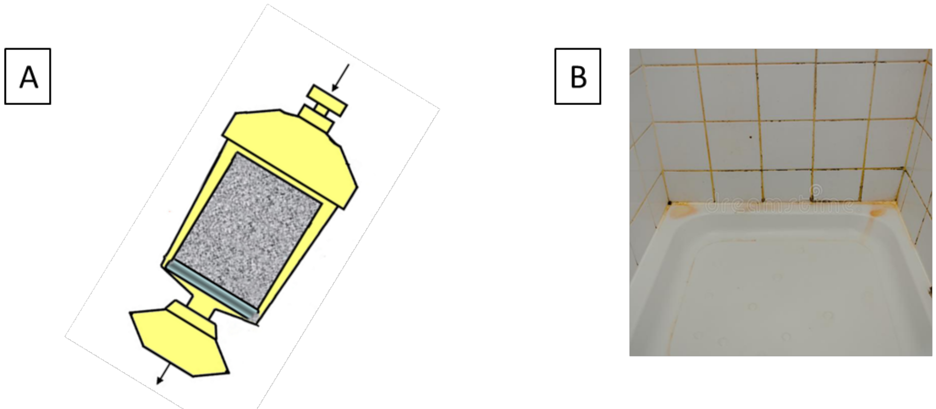

Bactericidal dynamic filters

Bactericidal blends for tile joints in domestic showers

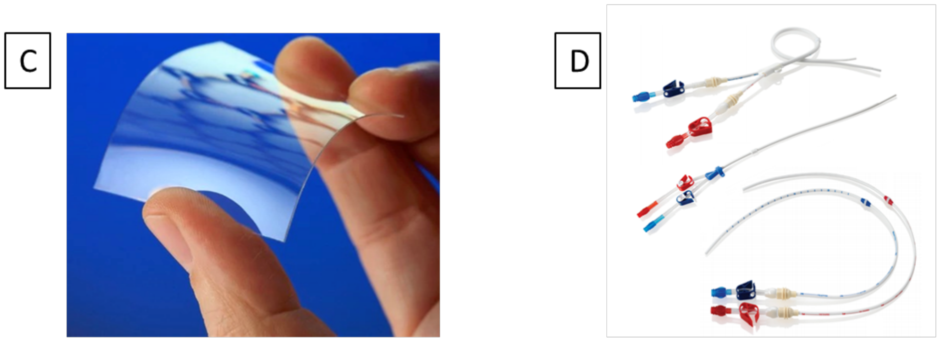

Antimicrobial electronic sensors

Antimicrobial catheters for urinary tract infections

Figure 4.3 – Possible applications for antimicrobial CA-SP-Ag nanomaterials. (A) Bactericidal dynamic filters for water sanitization; (B) Bactericidal blends for tile joints in showers; (C) Antimicrobial flexible sensors; (D) Antimicrobial catheters for the prevention of urinary tract infections.

Keeping in mind the evidence of our results, we suggest CA-SP-Ag powders would potentially be studied and employed in the form of suspensions for the sanitization of water. The great efficacy against *E. coli* exerted by our compounds paves the way for an application in active bactericidal dynamic filters (Figure 4.3A), able to prevent the transition of living microorganisms through them and thus preventing the formation of bacterial biofilms downstream of the purification apparatus. Moreover, such water filters would potentially display an additional advantage with respect from classic ones, which are based on Ag releasing systems: acting as catalysts for oxidative bacterial degradation, our CA-SP-Ag powders should guarantee a longer working life, since Ag will not be consumed during the filtering activity.

Shifting our focus on antimicrobial surfaces, a promising application of CA-Ag compounds is represented by the implementation of antimicrobial properties in electronic sensors (Figure 4.3C). The high conductivity of graphene-related materials [96], especially those which have not undergone any or little oxidizing procedure, is one of the most exploited features of these nanomaterials, thus graphene-based electronic sensors are becoming more and more popular in the scientific world. The risk of contamination and, above all, the eventual biofilm formation on the external core of the sensors obviously hamper their functionalities, thus bactericidal properties exerted by the sensor itself would represent an innovative solution in this field. Future development may thus relate with an in-depth research of the electronic conductive properties of CA-Ag compounds and their capability to prevent formation of bacterial biofilms.

Our powders would potentially find application in those contexts where a prevention of bacterial biofilm is needed. For instance, one could think about tile joints of showers, where the abundance of humidity and stagnation of water inside porous structures promote the proliferation of bacteria, usually identifiable by a yellow/orange slime deposition. A homogeneous blend between the filler and CA-Ag powder could thus offer a solution for the prevention of biofilms inside domestic showers (Figure 4.3B).

Also CA-Ag powders may be useful to fabricate polymeric antimicrobial membranes or catheters dealing with urinary system (Figure 4.3D): the absence of proteins which characterize body fluids in this sector represents indeed a good chance for the maximal exploitation of antimicrobial features of CA-Ag compounds, since the protein aggregation onto the material surface is prevented.

Even though further researches will be necessary to investigate whether CA-Ag compounds exhibit or not cytotoxic activity against eukaryotic primary cells, our findings took the first step reporting an outstanding antimicrobial activity against *E. coli*, which is one of the main microorganisms responsible for urinary tract infections.

In conclusion, our research integrates the existing scientific literature which relates with the antimicrobial efficacy of graphene-related materials, providing new knowledge about a simple, sustainable and green procedure for their functionalization. This work aimed to characterize and evaluate the antimicrobial efficacy of three graphene allotrope, i.e. Graphite, Carbon Black and MWCNTs, which have undergone a double-stage functionalization process with SP and Ag NPs. We could claim this procedure resulted to be a reliable and sustainable approach to significantly enhance their intrinsic antimicrobial properties, paving the way for future characterizations and developments in a multitude of scientific fields.

5 Appendix

5.1 TGA graphs

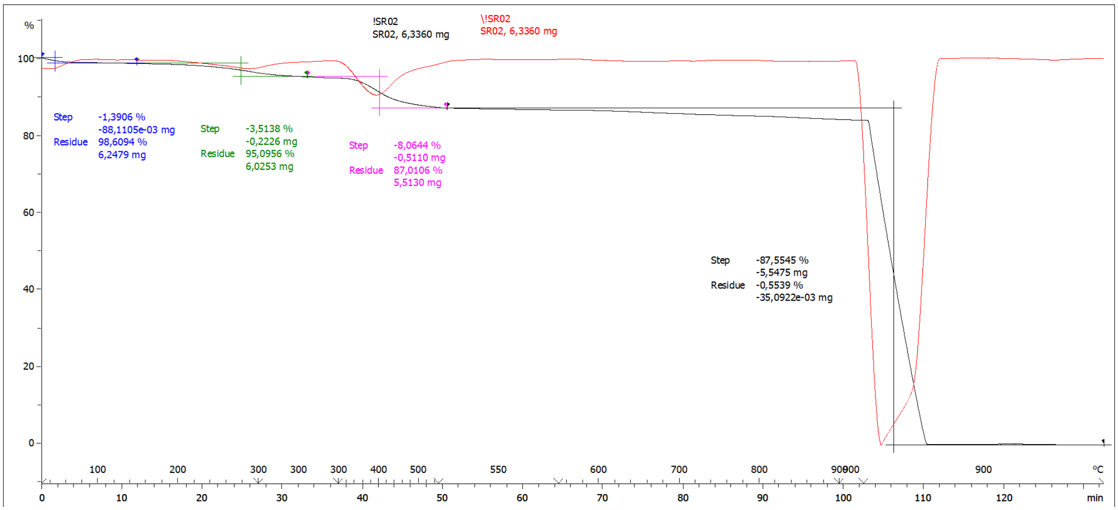

Figure 5.1 - TGA graph for the sample G.

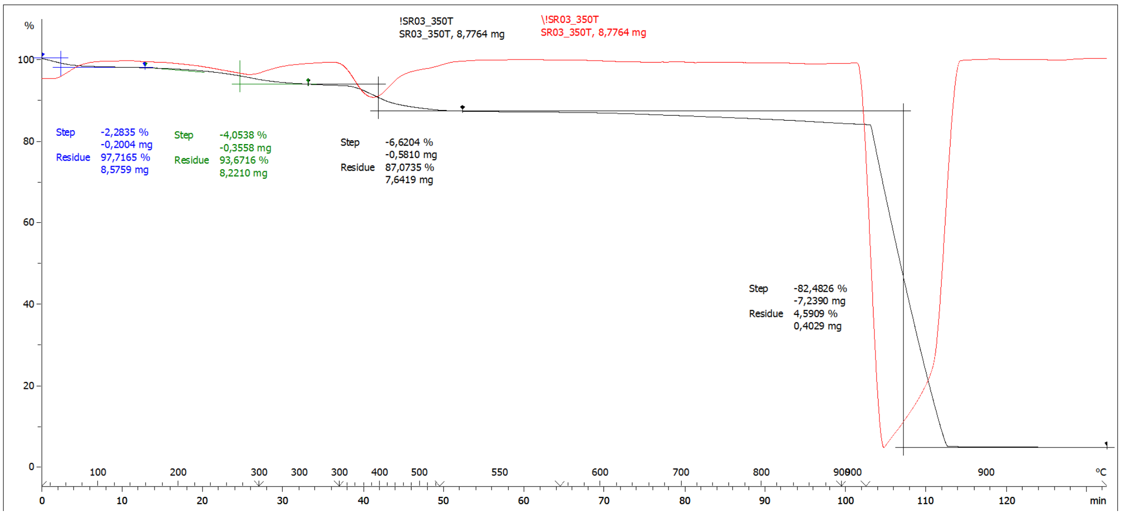

Figure 5.2 - TGA graph for the sample G350.

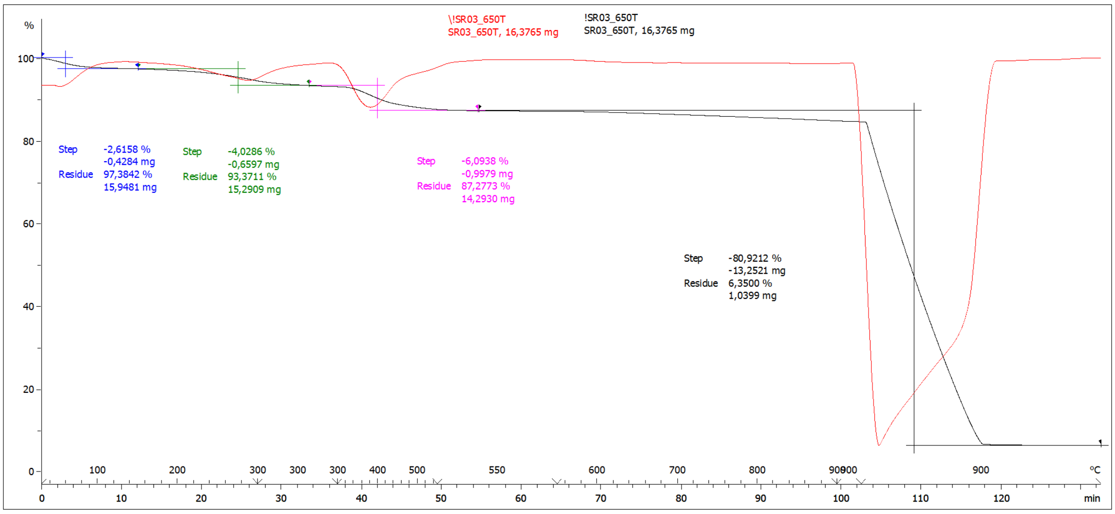

Figure 5.3 - TGA graph for the sample G650.

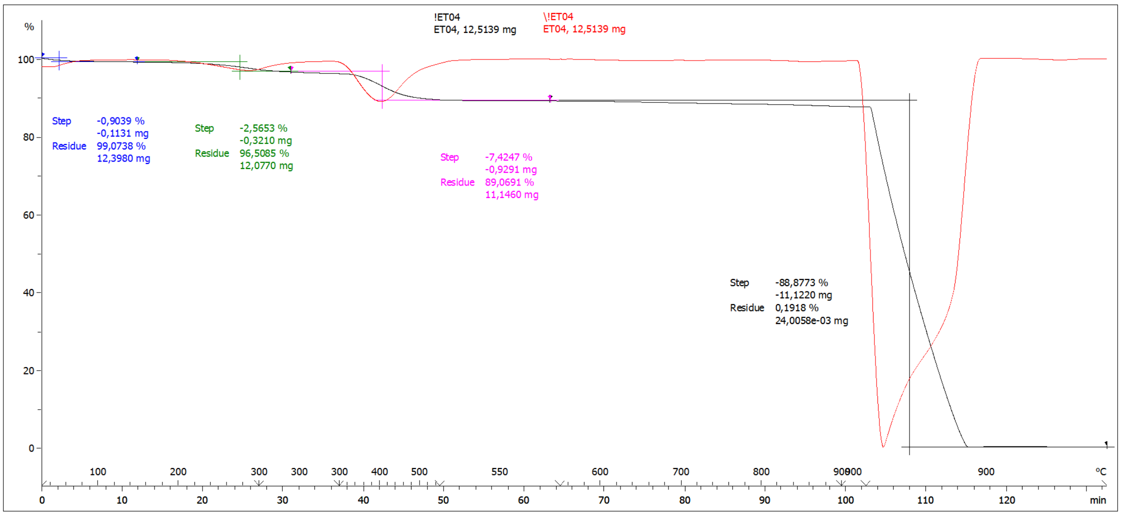

Figure 5.4 - TGA graph for the sample CB.

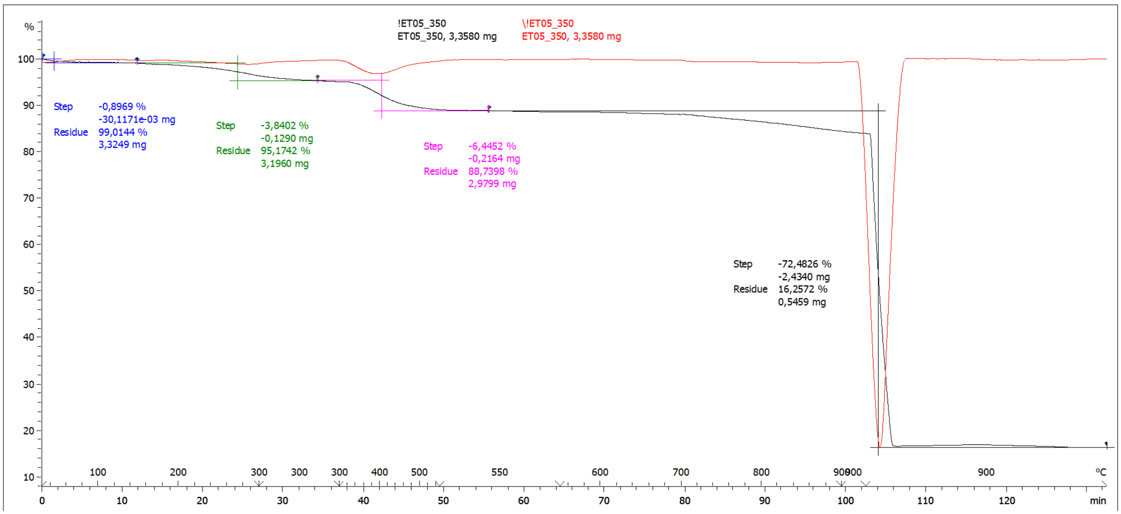

Figure 5.5 - TGA graph for the sample CB350.

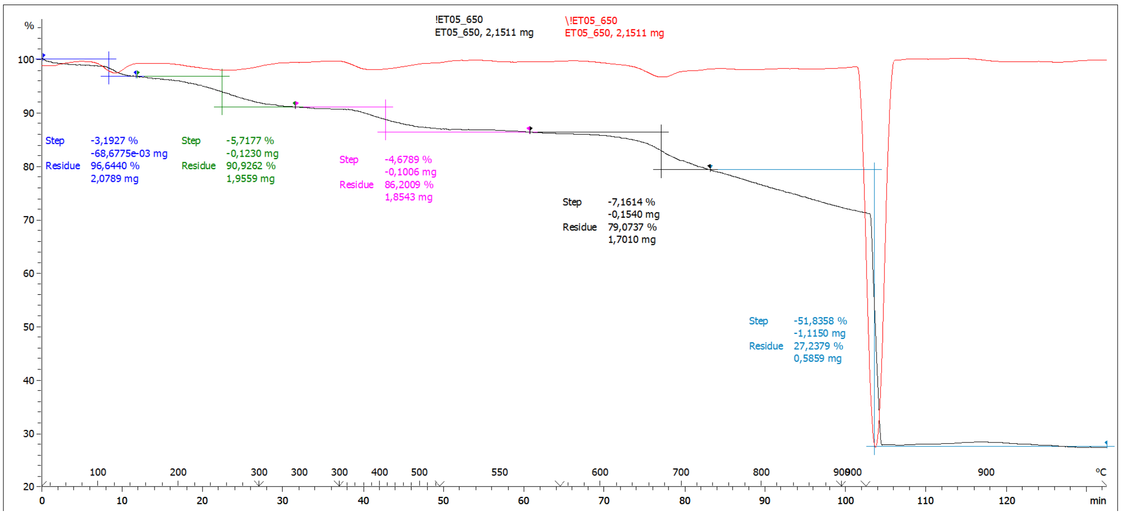

Figure 5.6 - TGA graph for the sample CB650.

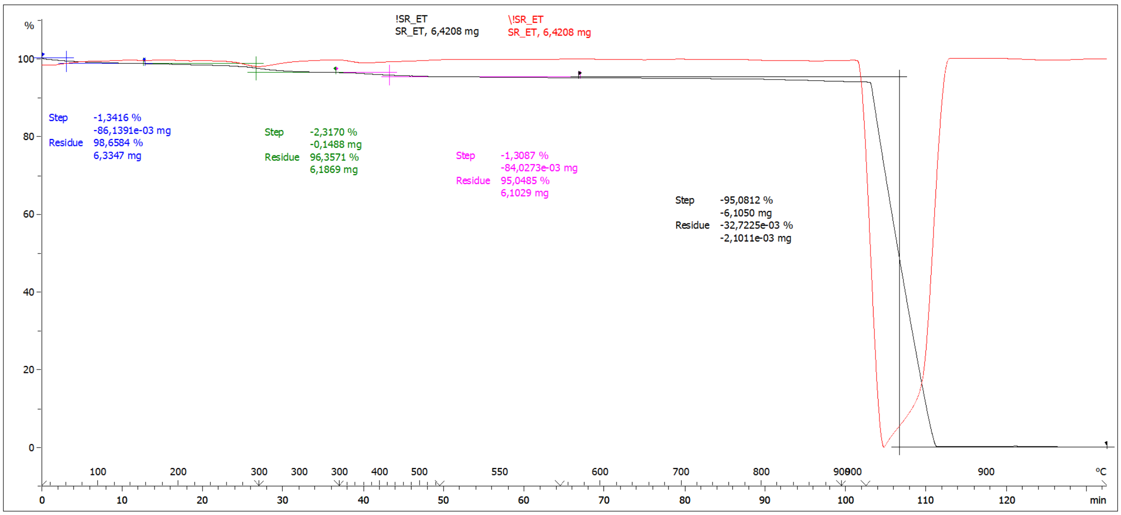

Figure 5.7 - TGA graph for the sample CNT.

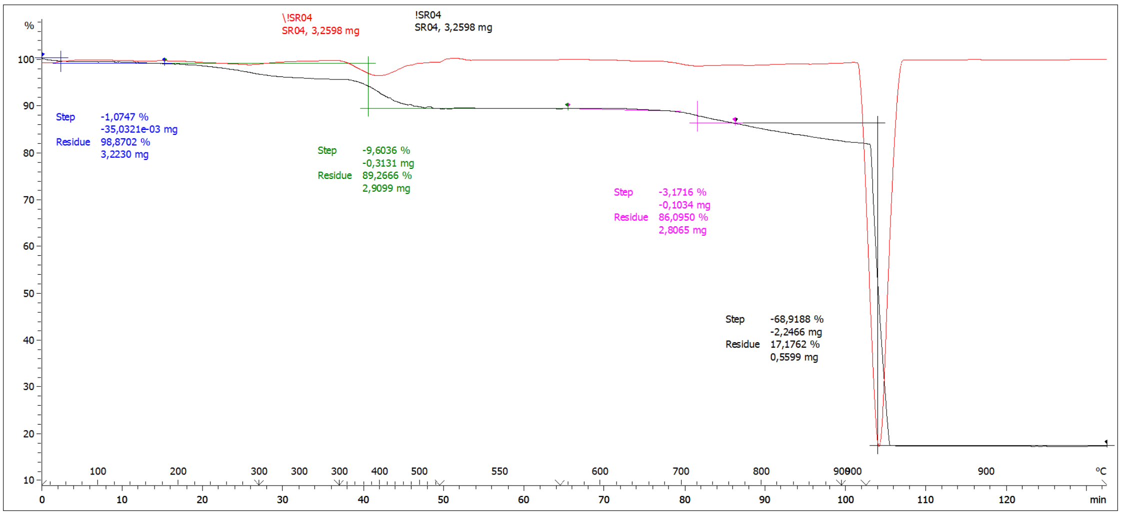

Figure 5.8 - TGA graph for the sample CNT350.

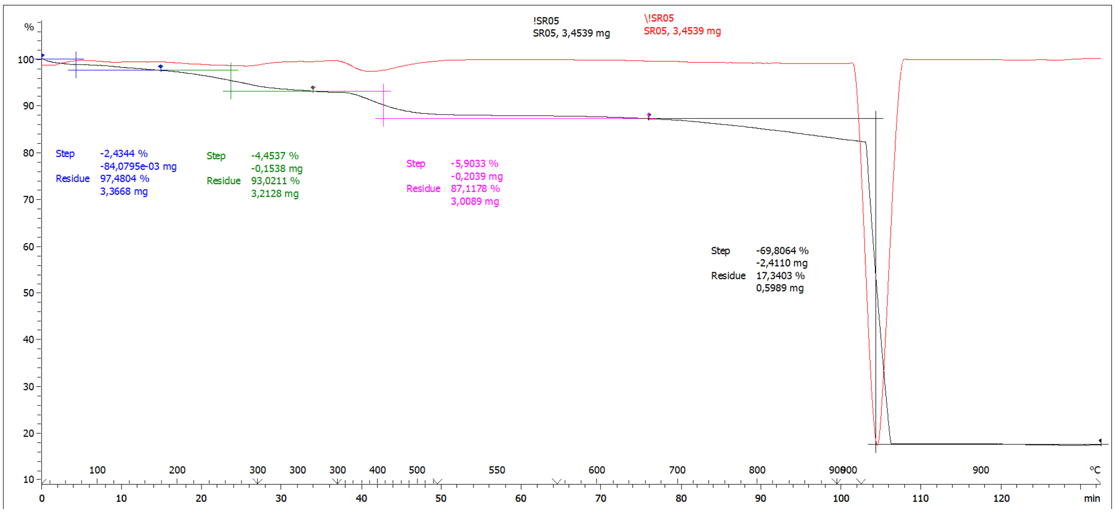

Figure 5.9 - TGA graph for the sample CNT650.

5.2 Antimicrobial activity evaluation tools

Validation of sample MBC					
Compound:	Sample name				
SP Moles / C=C Moles:	0.019	[µmol/µmol]			
SP Moles / Ag Moles:	0.370	[µmol/µmol]			
SP Moles / Compound mass	0.562	[µmol/mg]			
	A	**B**	**C**	**D**	
Ag Concentration:	2000.0	250.0	31.3	3.9	[µM]
SP Concentration:	740.0	92.5	11.6	1.4	[µM]
C=C Concentration:	38.9	4.9	0.6	0.1	[mM]
Volumes per eppendorf:	400 µL Ag-C/SP (30:1) in PBS + 400 µL E.coli in PBS/LB (100:1)				
Dilutions:	1:1	1:8	1:64	1:512	
Bacteria:	E.Coli JM109				
Inoculum suspension:	~ 10^6	[CFU/mL]			
Cell Density in well:	10^6	[CFU/mL]			
Medium:	PBS/LB (100:1) [Samples & CTRL-] - dH2O/LB (100:1) [CTRL+]				

Figure 5.10 - Example of table used for the computations of compounds molarity.

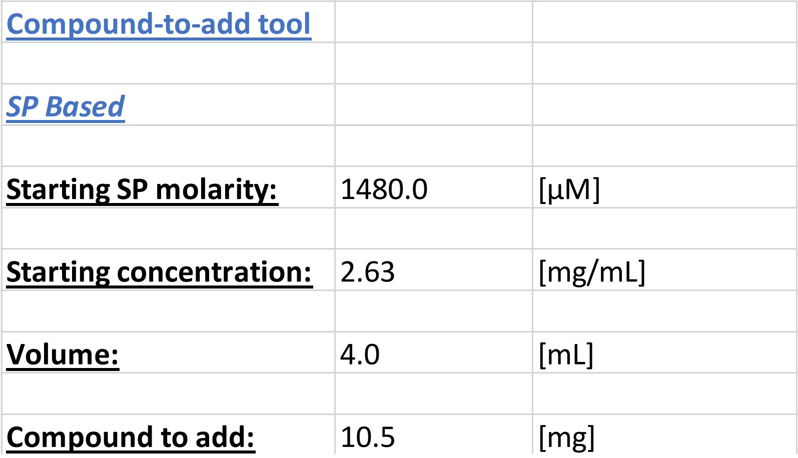

Compound-to-add tool		
SP Based		
Starting SP molarity:	1480.0	[µM]
Starting concentration:	2.63	[mg/mL]
Volume:	4.0	[mL]
Compound to add:	10.5	[mg]

Figure 5.11 – Tool for the computation of the amount of powders to add to a desired volume to reach the desired compound concentration.

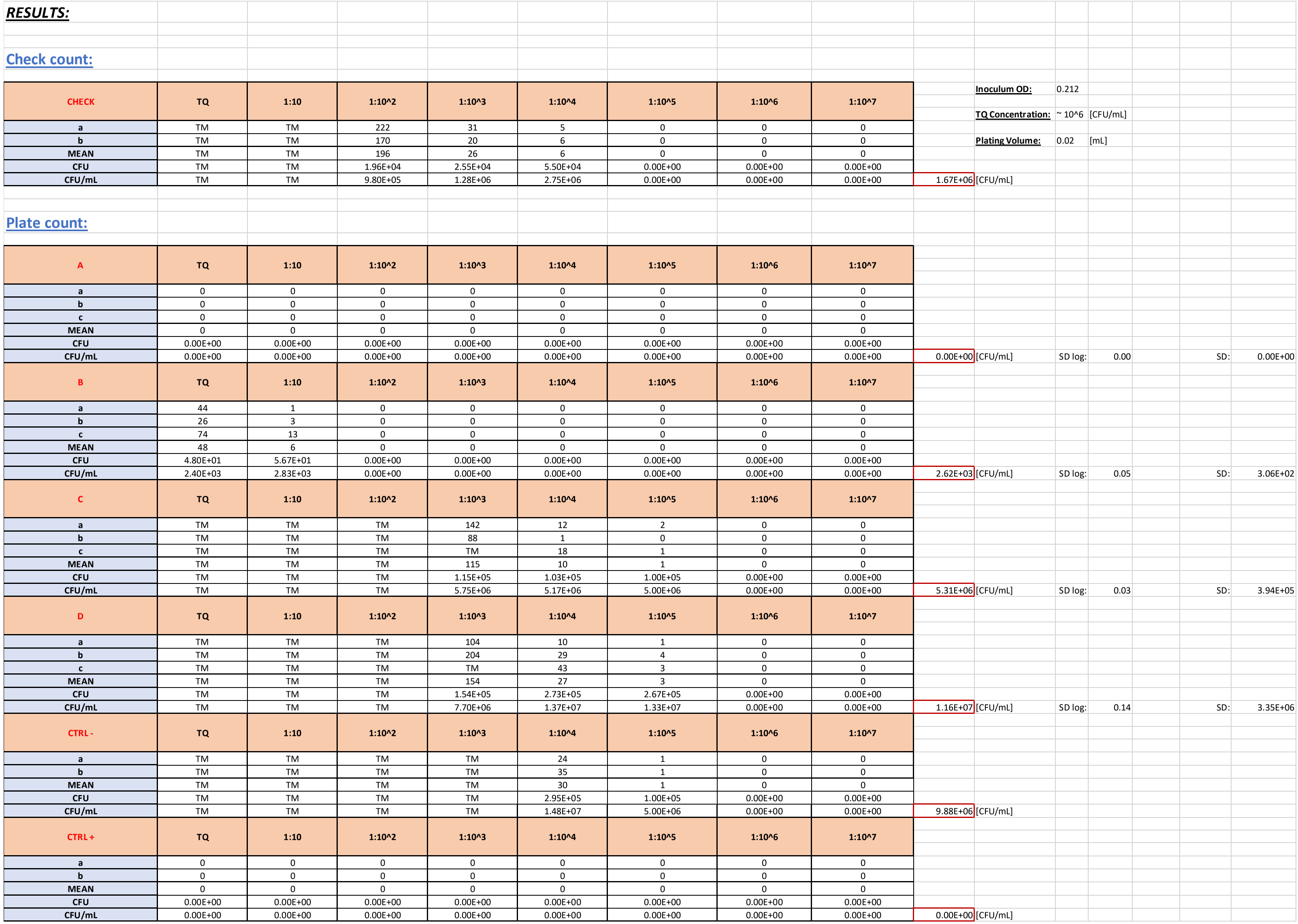

RESULTS:

Check count:

Inoculum OD: 0.212

TQ Concentration: ~ 10^6 [CFU/mL]

Plating Volume: 0.02 [mL]

CHECK	TQ	1:10	1:10^2	1:10^3	1:10^4	1:10^5	1:10^6	1:10^7		
a	TM	TM	222	31	5	0	0	0		
b	TM	TM	170	20	6	0	0	0		
MEAN	TM	TM	196	26	6	0	0	0		
CFU	TM	TM	1.96E+04	2.55E+04	5.50E+04	0.00E+00	0.00E+00	0.00E+00		
CFU/mL	TM	TM	9.80E+05	1.28E+06	2.75E+06	0.00E+00	0.00E+00	0.00E+00	1.67E+06	[CFU/mL]

Plate count:

A	TQ	1:10	1:10^2	1:10^3	1:10^4	1:10^5	1:10^6	1:10^7						
a	0	0	0	0	0	0	0	0						
b	0	0	0	0	0	0	0	0						
c	0	0	0	0	0	0	0	0						
MEAN	0	0	0	0	0	0	0	0						
CFU	0.00E+00	0.00E+00	0.00E+00	0.00E+00	0.00E+00	0.00E+00	0.00E+00	0.00E+00						
CFU/mL	0.00E+00	0.00E+00	0.00E+00	0.00E+00	0.00E+00	0.00E+00	0.00E+00	0.00E+00	0.00E+00	[CFU/mL]	SD log:	0.00	SD:	0.00E+00
B	**TQ**	**1:10**	**1:10^2**	**1:10^3**	**1:10^4**	**1:10^5**	**1:10^6**	**1:10^7**						
a	44	1	0	0	0	0	0	0						
b	26	3	0	0	0	0	0	0						
c	74	13	0	0	0	0	0	0						
MEAN	48	6	0	0	0	0	0	0						
CFU	4.80E+01	5.67E+01	0.00E+00	0.00E+00	0.00E+00	0.00E+00	0.00E+00	0.00E+00						
CFU/mL	2.40E+03	2.83E+03	0.00E+00	0.00E+00	0.00E+00	0.00E+00	0.00E+00	0.00E+00	2.62E+03	[CFU/mL]	SD log:	0.05	SD:	3.06E+02
C	**TQ**	**1:10**	**1:10^2**	**1:10^3**	**1:10^4**	**1:10^5**	**1:10^6**	**1:10^7**						
a	TM	TM	TM	142	12	2	0	0						
b	TM	TM	TM	88	1	0	0	0						
c	TM	TM	TM	TM	18	1	0	0						
MEAN	TM	TM	TM	115	10	1	0	0						
CFU	TM	TM	TM	1.15E+05	1.03E+05	1.00E+05	0.00E+00	0.00E+00						
CFU/mL	TM	TM	TM	5.75E+06	5.17E+06	5.00E+06	0.00E+00	0.00E+00	5.31E+06	[CFU/mL]	SD log:	0.03	SD:	3.94E+05
D	**TQ**	**1:10**	**1:10^2**	**1:10^3**	**1:10^4**	**1:10^5**	**1:10^6**	**1:10^7**						
a	TM	TM	TM	104	10	1	0	0						
b	TM	TM	TM	204	29	4	0	0						
c	TM	TM	TM	TM	43	3	0	0						
MEAN	TM	TM	TM	154	27	3	0	0						
CFU	TM	TM	TM	1.54E+05	2.73E+05	2.67E+05	0.00E+00	0.00E+00						
CFU/mL	TM	TM	TM	7.70E+06	1.37E+07	1.33E+07	0.00E+00	0.00E+00	1.16E+07	[CFU/mL]	SD log:	0.14	SD:	3.35E+06
CTRL -	**TQ**	**1:10**	**1:10^2**	**1:10^3**	**1:10^4**	**1:10^5**	**1:10^6**	**1:10^7**						
a	TM	TM	TM	TM	24	1	0	0						
b	TM	TM	TM	TM	35	1	0	0						
MEAN	TM	TM	TM	TM	30	1	0	0						
CFU	TM	TM	TM	TM	2.95E+05	1.00E+05	0.00E+00	0.00E+00						
CFU/mL	TM	TM	TM	TM	1.48E+07	5.00E+06	0.00E+00	0.00E+00	9.88E+06	[CFU/mL]				
CTRL +	**TQ**	**1:10**	**1:10^2**	**1:10^3**	**1:10^4**	**1:10^5**	**1:10^6**	**1:10^7**						
a	0	0	0	0	0	0	0	0						
b	0	0	0	0	0	0	0	0						
MEAN	0	0	0	0	0	0	0	0						
CFU	0.00E+00	0.00E+00	0.00E+00	0.00E+00	0.00E+00	0.00E+00	0.00E+00	0.00E+00						
CFU/mL	0.00E+00	0.00E+00	0.00E+00	0.00E+00	0.00E+00	0.00E+00	0.00E+00	0.00E+00	0.00E+00	[CFU/mL]				

Figure 5.12 - Table for the data processing of numbers obtained from CFUs enumeration of culture plates.

5.3 Drop method for the plating out of bacteria

Dealing with the direct count of viable CFUs from culture plates involved the choice of suitable plating methods. Among those most utilized from the scientific community we decided to evaluate the feasibility of the drop method.
This plating method is similar to the one eventually used during our antimicrobial experiments (i.e. classic spread method) but does not require glass beads. The desired inoculum is poured onto LB-agar with a drop of known volume (in our case, 20 µL) and no spreading actions follow this stage. Plates are next transferred into incubator without flip them over as for the other spread methods. After 24 hours, CFUs are ready to be enumerated.

One of the advantages of this method is to avoid the waste of glass beads and contamination risks related to their usage. Moreover, plating times are considerably reduced.
Beside these positive features, the limited range of enumerable CFUs represents a disadvantage of this technique. Whereas the range of enumerable CFUs is between 0 and 300 for spread methods, for the drop method it is restricted from 0 to 50 due to the impossibility of discerning separate colonies in such a restricted space (Figure 5.13).

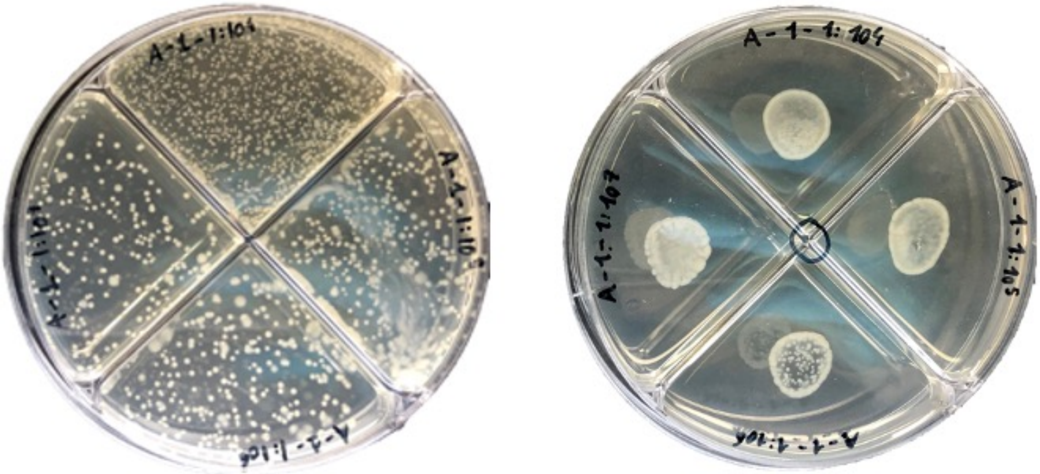

Figure 5.13 – Representative image for the comparison of the two mentioned plating methods: spread method (left) and drop method (right). Despite comparable concentrations in terms of CFUs/mL (the two plates derive from culture of the same inoculum), the impossibility of discerning separate colonies for the drop method is clearly visible for the plate on the right.

Despite this problem, we decided to evaluate the feasibility of the drop method for the plating out of bacteria, comparing results with those derived from a standard spread method. Representative pictures are displayed in Figure 5.14 and cumulative results from experiments, carried out with triplicates for each method, are provided in the Table 5.1.

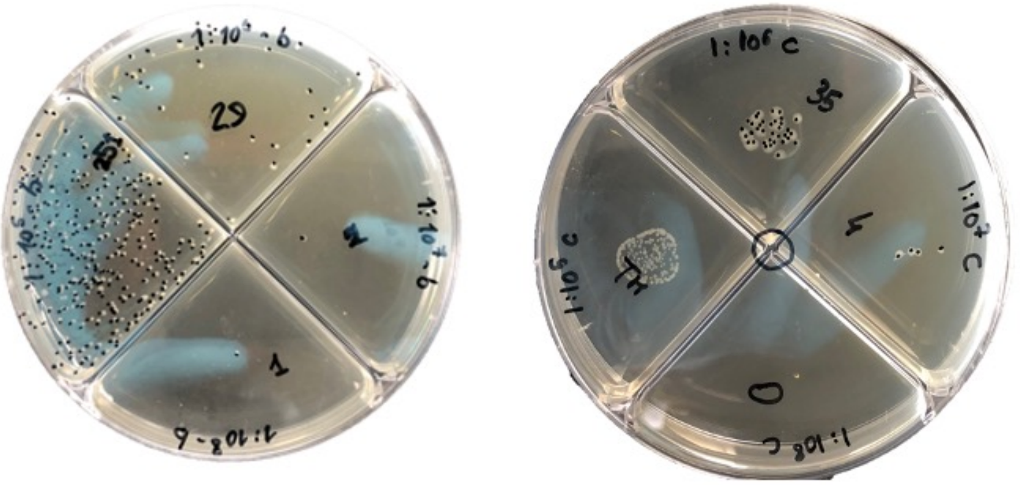

Figure 5.14 – Representative image for the comparison of results derived from the spread method (left) and the drop method (right).

Table 5.1 - Table of results from direct count of viable CFUs. The upper table displays results deriving from the classic SPREAD method. The table below represent those deriving from DROP method.

Starting OD_{600nm} *= 0.180 A.U. (~*10^9 *CFU/mL) - Plating volume = 20 µL.*

SPREAD method	**1:10^5**	**1:10^6**	**1:10^7**	**1:10^8**		
a	259	13	5	3		
b	251	29	2	1		
c	316	54	4	/		
MEAN	275	32	4	2		
CFU	2.75E+07	3.20E+07	3.67E+07	2.00E+08		
CFU/mL	1.38E+09	1.60E+09	1.83E+09	1.00E+10	1.60E+09	[CFUs/mL]

DROP method	**1:10^5**	**1:10^6**	**1:10^7**	**1:10^8**		
a	TM	32	3	0		
b	TM	42	5	0		
c	TM	35	4	0		
MEAN	TM	36	4	0		
CFU	TM	3.63E+07	4.00E+07	0.00E+00		
CFU/mL	TM	1.82E+09	2.00E+09	0.00E+00	1.91E+09	[CFUs/mL]

Results display little differences between the two methods in terms of concentration ($1.60 \cdot 10^9$ CFUs/mL against $1.91 \cdot 10^9$ CFUs/mL). Despite this, for the drop method it was not possible to perform any statistical analysis (e.g. computation of standard deviation) due to the lack of a third significant plate. Therefore, basing our attention on the number of significant plates given from this test, these findings led us to exclude the drop method (2 significant plates) as a possible alternative to the classic spread method (4 significant plates), which gives more precise and robust results.

Index of Figures

Index of Tables

Bibliography

[1] M. Yousefi *et al.*, Anti-Bacterial Activity of Graphene Oxide as a New Weapon Nanomaterial to Combat Multidrug-Resistance Bacteria, *Mater. Sci. Eng. C*, vol. 74, pp. 568–581, 2017, DOI: 10.1016/j.msec.2016.12.125.

[2] C. B. Clemons, M. W. Roberts, J. P. Wilber, G. W. Young, A. Buldum, and D. D. Quinn, Continuum Plate Theory and Atomistic Modeling to Find the Flexural Rigidity of a Graphene Sheet Interacting with a Substrate, *J. Nanotechnol.*, no. May, 2010, DOI: 10.1155/2010/868492.

[3] K. S. Novoselov *et al.*, Electric Field Effect in Atomically Thin Carbon Films Supplementary, *Science (80-.).*, vol. 5, no. 1, pp. 1–12, 2004, DOI: 10.1126/science.aab1343.

[4] M. Maas, Carbon Nanomaterials as Antibacterial Colloids, *Materials (Basel).*, vol. 9, no. 8, pp. 1–19, 2016, DOI: 10.3390/ma9080617.

[5] R. L. Davies and S. F. Etris, The Development and Functions of Silver in Water Purification and Disease Control, *Catal. Today*, vol. 36, no. 1, pp. 107–114, 1997, DOI: 10.1016/S0920-5861(96)00203-9.

[6] X. Zou, L. Zhang, Z. Wang, and Y. Luo, Mechanisms of the Antimicrobial Activities of Graphene Materials, *J. Am. Chem. Soc.*, vol. 138, no. 7, pp. 2064–2077, 2016, DOI: 10.1021/jacs.5b11411.

[7] J. Gao and B. Xu, Applications of Nanomaterials inside Cells, *Nano Today*, vol. 4, no. 1, pp. 37–51, 2009, DOI: 10.1016/j.nantod.2008.10.009.

[8] J. L. West and N. J. Halas, Engineered Nanomaterials for Biophotonics Applications: Improving Sensing, Imaging, and Therapeutics, *Annu. Rev. Biomed. Eng.*, vol. 5, no. 1, pp. 285–292, 2003, DOI: 10.1146/annurev.bioeng.5.011303.120723.

[9] S. Lanone and J. Boczkowski, Biomedical Applications and Potential Health Risks of Nanomaterials: Molecular Mechanisms, *Curr. Mol. Med.*, vol. 6, no. 6, pp. 651–663, 2006, DOI: 10.2174/156652406778195026.

[10] C. Liu *et al.*, Nano-Carrier for Gene Delivery and Bioimaging Based on Carbon Dots with PEI-Passivation Enhanced Fluorescence, *Biomaterials*, vol. 33, no. 13, pp. 3604–3613, 2012, DOI: 10.1016/j.biomaterials.2012.01.052.

[11] H. M. Hegab, A. Elmekawy, L. Zou, D. Mulcahy, C. P. Saint, and M. Ginic-Markovic, The Controversial Antibacterial Activity of Graphene-Based Materials, *Carbon N. Y.*, vol. 105, pp. 362–376, 2016, DOI: 10.1016/j.carbon.2016.04.046.

[12] M. Papi *et al.*, Biomimetic Antimicrobial Cloak by Graphene-Oxide Agar Hydrogel, *Sci. Rep.*, vol. 6, pp. 1–7, 2016, DOI: 10.1038/s41598-016-0010-7.

[13] M. Arakha *et al.*, Antimicrobial Activity of Iron Oxide Nanoparticle upon Modulation of Nanoparticle-Bacteria Interface, *Sci. Rep.*, vol. 5, pp. 1–12, 2015, DOI: 10.1038/srep14813.

[14] R. Kumar, A. Umar, G. Kumar, and H. S. Nalwa, Antimicrobial Properties of ZnO Nanomaterials: A Review, *Ceram. Int.*, vol. 43, no. 5, pp. 3940–3961, 2017, DOI: 10.1016/j.ceramint.2016.12.062.

[15] A. Azam, A. S. Ahmed, M. Oves, M. S. Khan, and A. Memic, Size-Dependent Antimicrobial Properties of CuO Nanoparticles against Gram-Positive and -Negative Bacterial Strains, *Int. J. Nanomedicine*, vol. 7, pp. 3527–3535, 2012, DOI: 10.2147/IJN.S29020.

[16] A. Azam, A. S. Ahmed, M. Oves, M. S. Khan, S. S. Habib, and A. Memic, Antimicrobial Activity of Metal Oxide Nanoparticles against Gram-Positive and Gram-Negative Bacteria: A Comparative Study, *Int. J. Nanomedicine*, vol. 7, pp. 6003–6009, 2012, DOI: 10.2147/IJN.S35347.

[17] M. Sui, L. Zhang, L. Sheng, S. Huang, and L. She, Synthesis of ZnO Coated Multi-Walled Carbon Nanotubes and Their Antibacterial Activities, *Sci. Total Environ.*, vol. 452–453, pp. 148–154, 2013, DOI: 10.1016/j.scitotenv.2013.02.056.

[18] E. Rosenberg, E. F. DeLong, S. Lory, E. Stackebrandt, and F. Thompson, The Prokaryotes: Prokaryotic Communities and Ecophysiology, *Prokaryotes Prokaryotic Communities Ecophysiol.*, pp. 1–528, 2012, DOI: 10.1007/978-3-642-30123-0.

[19] J. B. Kaplan, Antibiotic-Induced Biofilm Formation, *Int. J. Artif. Organs*, vol. 34, no. 9, pp. 737–751, 2011, DOI: 10.5301/ijao.5000027.

[20] X. Fan *et al.*, Mussel-Inspired Synthesis of NIR-Responsive and Biocompatible Ag-Graphene 2D Nanoagents for Versatile Bacterial Disinfections, *ACS Appl. Mater. Interfaces*, vol. 10, no. 1, pp. 296–307, 2018, DOI: 10.1021/acsami.7b16283.

[21] C. L. Ventola, The Antibiotic Resistance Crisis: Part 1: Causes and Threats., *P T*, vol. 40, no. 4, pp. 277–83, Apr. 2015.

[22] S. Szunerits and R. Boukherroub, Antibacterial Activity of Graphene-Based

Materials, *J. Mater. Chem. B*, vol. 4, no. 43, pp. 6892–6912, 2016, DOI: 10.1039/c6tb01647b.

[23] H. Yun, J. D. Kim, H. C. Choi, and C. W. Lee, Antibacterial Activity of CNT-Ag and GO-Ag Nanocomposites against Gram-Negative and Gram-Positive Bacteria, *Bull. Korean Chem. Soc.*, vol. 34, no. 11, pp. 3261–3264, 2013, DOI: 10.5012/bkcs.2013.34.11.3261.

[24] S. M. Dizaj, A. Mennati, S. Jafari, K. Khezri, and K. Adibkia, Antimicrobial Activity of Carbon-Based Nanoparticles, *Adv. Pharm. Bull.*, vol. 5, no. 1, pp. 19–23, 2015, DOI: 10.5681/apb.2015.003.

[25] N. X. Dinh *et al.*, Water-Dispersible Silver Nanoparticles-Decorated Carbon Nanomaterials: Synthesis and Enhanced Antibacterial Activity, *Appl. Phys. A Mater. Sci. Process.*, vol. 119, no. 1, pp. 85–95, 2015, DOI: 10.1007/s00339-014-8962-6.

[26] V. Barbera, A. Bernardi, A. Palazzolo, A. Rosengart, L. Brambilla, and M. Galimberti, Facile and Sustainable Functionalization of Graphene Layers with Pyrrole Compounds, *Pure Appl. Chem.*, vol. 90, no. 2, pp. 253–270, 2018, DOI: 10.1515/pac-2017-0708.

[27] Z. Çiplak, N. Yildiz, and A. Cąlimli, Investigation of Graphene/Ag Nanocomposites Synthesis Parameters for Two Different Synthesis Methods, *Fullerenes Nanotub. Carbon Nanostructures*, vol. 23, no. 4, pp. 361–370, 2015, DOI: 10.1080/1536383X.2014.894025.

[28] R. S. Edwards and K. S. Coleman, Graphene Synthesis: Relationship to Applications, *Nanoscale*, vol. 5, no. 1, pp. 38–51, 2013, DOI: 10.1039/c2nr32629a.

[29] Y. Arao and M. Kubouchi, High-Rate Production of Few-Layer Graphene by High-Power Probe Sonication, *Carbon N. Y.*, vol. 95, pp. 802–808, 2015, DOI: 10.1016/j.carbon.2015.08.108.

[30] U. Khan, A. O'Neill, M. Lotya, S. De, and J. N. Coleman, High-Concentration Solvent Exfoliation of Graphene, *Small*, vol. 6, no. 7, pp. 864–871, 2010, DOI: 10.1002/smll.200902066.

[31] C. Chung, Y. K. Kim, D. Shin, S. R. Ryoo, B. H. Hong, and D. H. Min, Biomedical Applications of Graphene and Graphene Oxide, *Acc. Chem. Res.*, vol. 46, no. 10, pp. 2211–2224, 2013, DOI: 10.1021/ar300159f.

[32] V. Singh, D. Joung, L. Zhai, S. Das, S. I. Khondaker, and S. Seal, Graphene Based Materials: Past, Present and Future, *Prog. Mater. Sci.*, vol. 56, no. 8, pp. 1178–1271, 2011, DOI: 10.1016/j.pmatsci.2011.03.003.

[33] H. Shen, L. Zhang, M. Liu, and Z. Zhang, Biomedical Applications of Graphene, *Theranostics*, vol. 2, no. 3, pp. 283–294, 2012, DOI:

10.7150/thno.3642.

[34] N. Mohanty and V. Berry, Graphene-Based Single-Bacterium Resolution Biodevice and DNA Transistor: Interfacing Graphene Derivatives with Nanoscale and Microscale Biocomponents, *Nano Lett.*, vol. 8, no. 12, pp. 4469–4476, 2008, DOI: 10.1021/nl802412n.

[35] Y. Chen *et al.*, Electronic Detection of Lectins Using Carbohydrate-Functionalized Nanostructures: Graphene versus Carbon Nanotubes, *ACS Nano*, vol. 6, no. 1, pp. 760–770, 2012, DOI: 10.1021/nn2042384.

[36] S. He *et al.*, A Craphene Nanoprobe for Rapid, Sensitive, and Multicolor Fluorescent DNA Analysis, *Adv. Funct. Mater.*, vol. 20, no. 3, pp. 453–459, 2010, DOI: 10.1002/adfm.200901639.

[37] L. A. L. Tang, J. Wang, and K. P. Loh, Graphene-Based SELDI Probe with Ultrahigh Extraction and Sensitivity for DNA Oligomer, *J. Am. Chem. Soc.*, vol. 132, no. 32, pp. 10976–10977, 2010, DOI: 10.1021/ja104017y.

[38] B. Chen, M. Liu, L. Zhang, J. Huang, J. Yao, and Z. Zhang, Polyethylenimine-Functionalized Graphene Oxide as an Efficient Gene Delivery Vector, *J. Mater. Chem.*, vol. 21, no. 21, pp. 7736–7741, 2011, DOI: 10.1039/c1jm10341e.

[39] H. Kim, R. Namgung, K. Singha, I. K. Oh, and W. J. Kim, Graphene Oxide-Polyethylenimine Nanoconstruct as a Gene Delivery Vector and Bioimaging Tool, *Bioconjug. Chem.*, vol. 22, no. 12, pp. 2558–2567, 2011, DOI: 10.1021/bc200397j.

[40] H. Bao *et al.*, Chitosan-Functionalized Graphene Oxide as a Nanocarrier for Drug and Gene Delivery, *Small*, vol. 7, no. 11, pp. 1569–1578, 2011, DOI: 10.1002/smll.201100191.

[41] S. R. Ryoo, Y. K. Kim, M. H. Kim, and D. H. Min, Behaviors of NIH-3T3 Fibroblasts on Graphene/Carbon Nanotubes: Proliferation, Focal Adhesion, and Gene Transfection Studies, *ACS Nano*, vol. 4, no. 11, pp. 6587–6598, 2010, DOI: 10.1021/nn1018279.

[42] H. Fan *et al.*, Fabrication, Mechanical Properties, and Biocompatibility of Graphene-Reinforced Chitosan Composites, *Biomacromolecules*, vol. 11, no. 9, pp. 2345–2351, 2010, DOI: 10.1021/bm100470q.

[43] S. Y. Park *et al.*, Enhanced Differentiation of Human Neural Stem Cells into Neurons on Graphene, *Adv. Mater.*, vol. 23, no. 36, pp. 263–267, 2011, DOI: 10.1002/adma.201101503.

[44] T. R. Nayak *et al.*, Graphene for Controlled and Accelerated Osteogenic Differentiation of Human Mesenchymal Stem Cells, *ACS Nano*, vol. 5, no. 6, pp. 4670–4678, 2011, DOI: 10.1021/nn200500h.

[45] D. D. L. Chung, Review: Graphite, *J. Mater. Sci.*, vol. 37, no. 8, pp. 1475–1489, 2002, DOI: 10.1023/A:1014915307738.

[46] Y. Hernandez, M. Lotya, D. Rickard, S. D. Bergin, and J. N. Coleman, Measurement of Multicomponent Solubility Parameters for Graphene Facilitates Solvent Discovery, *Langmuir*, vol. 26, no. 5, pp. 3208–3213, 2010, DOI: 10.1021/la903188a.

[47] S. Liu *et al.*, Antibacterial Activity of Graphite, Graphite Oxide, Graphene Oxide, and Reduced Graphene Oxide: Membrane and Oxidative Stress, *ACS Nano*, vol. 5, no. 9, pp. 6971–6980, 2011, DOI: 10.1021/nn202451x.

[48] S. Peddavarapu and R. Jayendra Bharathi, CNT Review, *Mater. Today Proc.*, vol. 5, no. 6, pp. 14507–14511, 2018, DOI: 10.1016/j.matpr.2018.03.038.

[49] Characterization of Single Wall Carbon Nanotubes (SWNTs) by Combining Dynamic Light Scattering and Raman Spectroscopy. Malvern Instrument Limited, pp. 1–9, 2015.

[50] S. Detriche, G. Zorzini, J. F. Colomer, A. Fonseca, and J. B. Nagy, Application of the Hansen Solubility Parameters Theory to Carbon Nanotubes, *J. Nanosci. Nanotechnol.*, vol. 8, no. 11, pp. 6082–6092, 2008, DOI: 10.1166/jnn.2008.SW16.

[51] B. Krause, M. Mende, P. Pötschke, and G. Petzold, Dispersability and Particle Size Distribution of CNTs in an Aqueous Surfactant Dispersion as a Function of Ultrasonic Treatment Time, *Carbon N. Y.*, vol. 48, no. 10, pp. 2746–2754, 2010, DOI: 10.1016/j.carbon.2010.04.002.

[52] S. Kang, M. Pinault, L. D. Pfefferle, and M. Elimelech, Single-Walled Carbon Nanotubes Exhibit Strong Antimicrobial Activity, *Langmuir*, vol. 23, no. 17, pp. 8670–8673, 2007, DOI: 10.1021/la701067r.

[53] F. A. Heckman, Microstructure of Carbon Black, *Rubber Chem. Technol.*, vol. 37, no. 5, pp. 1245–1298, 1964, DOI: 10.5254/1.3540400.

[54] T. M. Sager and V. Castranova, Surface Area of Particle Administered versus Mass in Determining the Pulmonary Toxicity of Ultrafine and Fine Carbon Black: Comparison to Ultrafine Titanium Dioxide, *Part. Fibre Toxicol.*, vol. 6, pp. 1–12, 2009, DOI: 10.1186/1743-8977-6-15.

[55] C. K. Chua and M. Pumera, Covalent Chemistry on Graphene, *Chem. Soc. Rev.*, vol. 42, no. 8, pp. 3222–3233, 2013, DOI: 10.1039/c2cs35474h.

[56] C. H. Deng *et al.*, Inactivation Performance and Mechanism of Escherichia Coli in Aqueous System Exposed to Iron Oxide Loaded Graphene Nanocomposites, *J. Hazard. Mater.*, vol. 276, pp. 66–76, 2014, DOI: 10.1016/j.jhazmat.2014.05.011.

[57] C. W. Chambers, C. M. Proctor, and P. W. Kabler, Bactericidal Effect of Low Concentrations of Silver, *J. Am. Water Works Assoc.*, vol. 54, no. 2, pp. 208–216, 1962, DOI: 10.1002/j.1551-8833.1962.tb00834.x.

[58] J. L. Clement and P. S. Jarrett, Antibacterial Silver, *Met. Based. Drugs*, vol. 1, no. 5–6, pp. 467–482, 1994, DOI: 10.1155/mbd.1994.467.

[59] J. Ma, J. Zhang, Z. Xiong, Y. Yong, and X. S. Zhao, Preparation, Characterization and Antibacterial Properties of Silver-Modified Graphene Oxide, *J. Mater. Chem.*, vol. 21, no. 10, pp. 3350–3352, 2011, DOI: 10.1039/c0jm02806a.

[60] M. Prodana, D. Ionita, C. Ungureanu, D. Bojin, and I. Demetrescu, Enhancing Antibacterial Effect of Multiwalled Carbon Nanotubes Using Silver Nanoparticles, *Dig. J. Nanomater. Biostructures*, vol. 6, no. 2, pp. 549–556, 2011.

[61] S. Hou *et al.*, Silver Nanoparticles-Loaded Exfoliated Graphite and Its Anti-Bacterial Performance, *Appl. Sci.*, vol. 7, no. 8, 2017, DOI: 10.3390/app7080852.

[62] J. D. Kim, H. Yun, G. C. Kim, C. W. Lee, and H. C. Choi, Antibacterial Activity and Reusability of CNT-Ag and GO-Ag Nanocomposites, *Appl. Surf. Sci.*, vol. 283, pp. 227–233, 2013, DOI: 10.1016/j.apsusc.2013.06.086.

[63] A. C. M. de Moraes, B. A. Lima, A. F. de Faria, M. Brocchi, and O. L. Alves, Graphene Oxide-Silver Nanocomposite as a Promising Biocidal Agent against Methicillin-Resistant Staphylococcus Aureus, *Int. J. Nanomedicine*, vol. 10, pp. 6847–6861, 2015, DOI: 10.2147/IJN.S90660.

[64] S. Vijay Kumar, N. M. Huang, H. N. Lim, A. R. Marlinda, I. Harrison, and C. H. Chia, One-Step Size-Controlled Synthesis of Functional Graphene Oxide/Silver Nanocomposites at Room Temperature, *Chem. Eng. J.*, vol. 219, pp. 217–224, 2013, DOI: 10.1016/j.cej.2012.09.063.

[65] M. R. Das *et al.*, The Synthesis of Citrate-Modified Silver Nanoparticles in an Aqueous Suspension of Graphene Oxide Nanosheets and Their Antibacterial Activity, *Colloids Surfaces B Biointerfaces*, vol. 105, pp. 128–136, 2013, DOI: 10.1016/j.colsurfb.2012.12.033.

[66] N. Gugala, J. Lemire, K. Chatfield-Reed, Y. Yan, G. Chua, and R. J. Turner, Using a Chemical Genetic Screen to Enhance Our Understanding of the Antibacterial Properties of Silver, *Genes (Basel).*, vol. 9, no. 7, 2018, DOI: 10.3390/genes9070344.

[67] P. Kumar, P. Huo, R. Zhang, and B. Liu, Antibacterial Properties of Graphene-Based Nanomaterials, *Nanomaterials*, vol. 9, no. 5, pp. 1–32, 2019, DOI: 10.3390/nano9050737.

[68] W. Hu *et al.*, Graphene-Based Antibacterial Paper, *ACS Nano*, vol. 4, no. 7, pp. 4317–4323, 2010, DOI: 10.1021/nn101097v.

[69] S. Pandit *et al.*, Vertically Aligned Graphene Coating Is Bactericidal and Prevents the Formation of Bacterial Biofilms, *Adv. Mater. Interfaces*, vol. 5, no. 7, pp. 1–9, 2018, DOI: 10.1002/admi.201701331.

[70] L. Hui *et al.*, Availability of the Basal Planes of Graphene Oxide Determines Whether It Is Antibacterial, *ACS Appl. Mater. Interfaces*, vol. 6, no. 15, pp. 13183–13190, 2014, DOI: 10.1021/am503070z.

[71] O. N. Ruiz *et al.*, Graphene Oxide: A Nonspecific Enhancer of Cellular Growth, *ACS Nano*, vol. 5, no. 10, pp. 8100–8107, 2011, DOI: 10.1021/nn202699t.

[72] V. Barbera *et al.*, Domino Reaction for the Sustainable Functionalization of Few-Layer Graphene, *Nanomaterials*, vol. 9, no. 1, 2019, DOI: 10.3390/nano9010044.

[73] V. Barbera *et al.*, Process for the Synthesis of 2-(2,5-Dimethyl-1H-Pyrrol-1-Yl)-1,3-Propanediol and Its Substituted Derivatives, US 10,329,253 B2, 2017.

[74] A. C. Agents, Standard Guide for Assessment of Antimicrobial Activity Using a Time-Kill, *Astm Int.*, vol. 03, no. Reapproved 2008, pp. 1–5, 2012, DOI: 10.1520/E2315-16.2.

[75] M. Galimberti *et al.*, Biobased Janus Molecule for the Facile Preparation of Water Solutions of Few Layer Graphene Sheets, *RSC Adv.*, vol. 5, no. 99, pp. 81142–81152, 2015, DOI: 10.1039/c5ra11387c.

[76] A. Al Nafiey, P. Subramanian, A. Addad, B. Sieber, S. Szunerits, and R. Boukherroub, Green Synthesis of Reduced Graphene Oxide-Silver Nanoparticles Using Environmentally Friendly L-Arginine for H2O2 Detection, *ECS J. Solid State Sci. Technol.*, vol. 5, no. 8, pp. M3060–M3066, 2016, DOI: 10.1149/2.0121608jss.

[77] W. E. Benet, G. S. Lewis, L. Z. Yang, and D. E. Peter Hughes, The Mechanism of the Reaction of the Tollens Reagent, *J. Chem. Res.*, vol. 35, no. 12, pp. 675–677, 2011, DOI: 10.3184/174751911X13206824040536.

[78] T. Thermogravimetric and I. Family, Thermogravimetric Analysis (TGA) A Beginner ' s Guide, 1960.

[79] J. Chen, B. Yao, C. Li, and G. Shi, An Improved Hummers Method for Eco-Friendly Synthesis of Graphene Oxide, *Carbon N. Y.*, vol. 64, no. 1, pp. 225–229, 2013, DOI: 10.1016/j.carbon.2013.07.055.

[80] B. Y. S. Chang *et al.*, Facile Hydrothermal Preparation of Titanium Dioxide

Decorated Reduced Graphene Oxide Nanocomposite, *Int. J. Nanomedicine*, vol. 7, pp. 3379–3387, 2012, DOI: 10.2147/IJN.S28189.

[81] U. Szeluga, B. Kumanek, and B. Trzebicka, Synergy in Hybrid Polymer/Nanocarbon Composites. A Review, *Compos. Part A Appl. Sci. Manuf.*, vol. 73, no. November, pp. 204–231, 2015, DOI: 10.1016/j.compositesa.2015.02.021.

[82] K. Y. Chun, S. K. Choi, H. J. Kang, C. Y. Park, and C. J. Lee, Highly Dispersed Multi-Walled Carbon Nanotubes in Ethanol Using Potassium Doping, *Carbon N. Y.*, vol. 44, no. 8, pp. 1491–1495, 2006, DOI: 10.1016/j.carbon.2005.12.004.

[83] C.-X. Liu and J.-W. Choi, Improved Dispersion of Carbon Nanotubes in Polymers at High Concentrations, *Nanomaterials*, vol. 2, no. 4, pp. 329–347, 2012, DOI: 10.3390/nano2040329.

[84] S. Bhattacharjee, DLS and Zeta Potential - What They Are and What They Are Not?, *J. Control. Release*, vol. 235, pp. 337–351, 2016, DOI: 10.1016/j.jconrel.2016.06.017.

[85] Z. Fathi, R. A. Khavari Nejad, H. Mahmoodzadeh, and T. N. Satari, Investigating of a Wide Range of Concentrations of Multi-Walled Carbon Nanotubes on Germination and Growth of Castor Seeds (Ricinus Communis L.), *J. Plant Prot. Res.*, vol. 57, no. 3, pp. 228–236, 2017, DOI: 10.1515/jppr-2017-0032.

[86] K. H. Liao, Y. S. Lin, C. W. MacOsko, and C. L. Haynes, Cytotoxicity of Graphene Oxide and Graphene in Human Erythrocytes and Skin Fibroblasts, *ACS Appl. Mater. Interfaces*, vol. 3, no. 7, pp. 2607–2615, 2011, DOI: 10.1021/am200428v.

[87] L. Wang and C. Chen, Pathophysiologic Mechanisms of Biomedical Nanomaterials, *Toxicol. Appl. Pharmacol.*, vol. 299, pp. 30–40, 2016, DOI: 10.1016/j.taap.2016.01.022.

[88] G. Duan *et al.*, Protein Corona Mitigates the Cytotoxicity of Graphene Oxide by Reducing Its Physical Interaction with Cell Membrane, *Nanoscale*, vol. 7, no. 37, pp. 15214–15224, 2015, DOI: 10.1039/c5nr01839k.

[89] H. Pan, Y. Zhang, G. X. He, N. Katagori, and H. Chen, A Comparison of Conventional Methods for the Quantification of Bacterial Cells after Exposure to Metal Oxide Nanoparticles, *BMC Microbiol.*, vol. 14, no. 1, 2014, DOI: 10.1186/s12866-014-0222-6.

[90] H. Haase, L. Jordan, L. Keitel, C. Keil, and B. Mahltig, Comparison of Methods for Determining the Effectiveness of Antibacterial Functionalized Textiles, *PLoS One*, vol. 12, no. 11, pp. 1–16, 2017, DOI: 10.1371/journal.pone.0188304.

[91] W. R. Li, X. B. Xie, Q. S. Shi, H. Y. Zeng, Y. S. Ou-Yang, and Y. Ben Chen, Antibacterial Activity and Mechanism of Silver Nanoparticles on Escherichia Coli, *Appl. Microbiol. Biotechnol.*, vol. 85, no. 4, pp. 1115–1122, 2010, DOI: 10.1007/s00253-009-2159-5.

[92] H. A. Hassan and M. A. El-Aal, Lipid Peroxidation End-Products as a Key of Oxidative Stress: Effect of Antioxidant on Their Production and Transfer of Free Radicals, in *Lipid Peroxidation*, 2012, pp. 63–88.

[93] S. Kang, M. Herzberg, D. F. Rodrigues, and M. Elimelech, Antibacterial Effects of Carbon Nanotubes: Size Does Matter!, *Langmuir*, vol. 24, no. 13, pp. 6409–6413, 2008, DOI: 10.1021/la800951v.

[94] T. Skaltsas, X. Ke, C. Bittencourt, and N. Tagmatarchis, Ultrasonication Induces Oxygenated Species and Defects onto Exfoliated Graphene, *J. Phys. Chem. C*, vol. 117, no. 44, pp. 23272–23278, 2013, DOI: 10.1021/jp4057048.

[95] I. H. Shaik and R. Mehvar, Rapid Determination of Reduced and Oxidized Glutathione Levels Using a New Thiol-Masking Reagent and the Enzymatic Recycling Method: Application to the Rat Liver and Bile Samples, *Anal. Bioanal. Chem.*, vol. 385, no. 1, pp. 105–113, 2006, DOI: 10.1038/jid.2014.371.

[96] F. Menaa, A. Abdelghani, and B. Menaa, Graphene Nanomaterials as Biocompatible and Conductive Scaffolds for Stem Cells: Impact for Tissue Engineering and Regenerative Medicine, *J. Tissue Eng. Regen. Med.*, vol. 9, pp. 1321–1338, 2015, DOI: 10.1002/term.